Analysis of Mudrock Lithofacies and Hydrocarbon-Source Potential of the Middle Ordovician Athens Shale, Alabama Fold and Thrust Belt

by

Phillip Andrew Daymond

A thesis submitted to the Graduate Faculty of
Auburn University
in partial fulfillment of the
requirements for the Degree of
Master of Science

Auburn, Alabama
May 7, 2017

Approved by

Dr. Charles E. Savrda, Chair, Professor of Geology
Dr. Ashraf Uddin, Professor of Geology
Dr. Ronald Lewis, Professor of Geology

ABSTRACT

Lithologic, petrologic, and geochemical studies were performed on the Ordovician Athens Shale, with a focus on a 140-ft-thick core section recovered near Calera, Alabama, supplemented by observations of limited outcrop exposures. Study goals were to (1) characterize the mudrock lithofacies of the Athens Shale, (2) interpret the environmental conditions and processes that influenced Athens Shale deposition, and (3) assess the potential of the Athens Shale as a hydrocarbon-source rock.

Four broad lithofacies are recognized in the Calera core interval of the Athens Shale based primarily on the abundance and character of limestone interbeds. Occurring in ascending stratigraphic order, lithofacies A, B, C, and D record a progressive increase in basin slope stability and/or water depth. Lithofacies A, dominated by nodular skeletal limestones, records slope instability and debris-flow deposition. Progressively thinner and finer-grained limestone beds in lithofacies B and C reflect deposition by proximal and distal turbidity currents. Carbonaceous shales, which become more prevalent upward from lithofacies B through lithofacies D reflect pelagic/hemipelagic depositional processes. Quartz silt content and evidence for weak bioturbation increase upward in the shales.

Major and trace element compositions of shale samples are similar to the average black shale, indicating no significant metal enrichment. Geochemical proxies for basin redox conditions yield ambiguous results, but provide some indication of temporal changes in basin oxygenation. Geochemical data also suggest that the Athens Shale muds were derived from a passive-margin, quartzose sedimentary provenance and thus do not reflect an arc-related terrane as expected for Taconic orogenesis.

Organic geochemical data from organic carbon and Rock-eval analyses indicate that the Athens Shale contains sufficient organic matter to have served as a hydrocarbon-source rock. However, in the Calera area, the Athens Shale is thermally overmature.

ACKNOWLEDGMENTS

First, I would like to thank the GSA, GCAGS, Department of Geosciences Advisory Board, and donors of the Waters-Folse award for providing financial support for my research, and the Argos Corporation for donating the Athens Shale core. To my parents, step-parents, sisters, and step-brothers who have given me unconditional support throughout this journey, thank you for always being there for me. To the staff of the department (Mrs. Sheila, Ms. Delaine, Tony), thank you for helping me take care of the “little things”. To all my fellow graduate students, thanks for being a great group to spend the past two years with. To my committee, thanks to Dr. Uddin for giving me support and having my back from the beginning. I will always remember that. Thanks to Dr. Lewis for helping me with my writing and presentation techniques, which certainly helped, and for checking my fossil identification. Finally, I would like to thank Dr. Savrda, without whom I would never have been where I am today. From directing me as an undergraduate on my first research project all the way through the completion of my masters thesis, he has provided a wealth of knowledge that only a true mentor and friend could provide. I will miss our field excursions and jokes along the way. And if I ever buy a mini-van, I will think of him every time I step foot in it.

TABLE OF CONTENTS

Abstract ii

Acknowledgments iv

List of Tables viii

List of Figures x

Chapter 1: Introduction 1

Chapter 2: Athens Shale 3

Chapter 3: Study Locations 7

3.1 Calera Core Section 7

3.2 Surface Exposures 10

Chapter 4: Methods 13

4.1 Calera Core 13

4.1.1 Core Descriptions and Sampling 13

4.1.2 Thin-Section Petrography 13

4.1.3 Carbonate and Organic Carbon Analyses 14

4.1.4 Whole-Rock Geochemical Analyses 15

4.1.5 Rock-Eval Pyrolysis 18

4.2 Supplementary Outcrop Studies 22

Chapter 5: Lithofacies 23
5.1 Lithofacies Descriptions 23
5.1.1 Lithofacies A - Nodular Limestone in Calcareous Mudstone 23
5.1.2 Lithofacies B – Carbonaceous Shale with Thin- to Medium-Bedded Limestones 31
5.1.3 Lithofacies C – Carbonaceous Shale with Thin, Fine-Grained Carbonate Beds and Laminae 36
5.1.4 Lithofacies D – Carbonaceous Shale 41
5.2 Vertical Distribution of Lithofacies 45
5.3 Lithofacies Interpretations 47
5.3.1 Lithofacies A 47
5.3.2 Limestones of Lithofacies B, C, and D 48
5.3.3 Shales in Lithofacies B, C, and D 49
5.4 Comparison to Pratts Ferry and Vincent sections 52
5.4.1 Pratts Ferry Section 52
5.4.2 Vincent Sections 55
Chapter 6: Athens Shale Geochemistry 58
6.1 Introduction 58
6.2 Trace Element Geochemistry 58
6.3 Potential Redox Indicators 64

6.3.1 V/Cr ratios 64
6.3.2 Ni/Co ratios 66
6.3.3 U/Th ratios 66
6.3.4 C/S relationship 67
6.3.5 Implications for Athens Shale Basin Oxygenation 69
6.4 Sediment Provenance 70
Chapter 7: Rock-Eval Pyrolysis 76
7.1 Quantity of Organic Matter 76
7.2 Thermal Maturity 77
7.3 Type of Organic Matter 79
7.4 Hydrocarbon-Source Potential 81
7.5 Comparison with Athens Shale Equivalents 81
Chapter 8: Summary and Conclusions 82
References 84
Appendix 1 98

LIST OF TABLES

Table 1. Representative geochemical proxies with detection limits for aqua regia ICP-ES/MS analyses. 16

Table 2. Representative geochemical proxies for whole-rock ICP-MS analysis 17

Table 3. Carbonate and organic carbon data for all 140 Calera Core samples (ND = no data due to operator error). 24

Table 4. Trace element compositions for the Athens Shale. 59

Table 4 cont. Trace element compositions of Athens Shale samples. 60

Table 5. Whole-rock geochemistry data derived from analyses of Athens Shale 61

Table 5 cont. Whole-rock geochemistry data derived from analyses of Athens Shale samples 62

Table 6. Trace element concentrations (%) in Athens Shale compared to the average shale and average black shale. 63

Table 7. Geochemical indices used as proxies for paleo-oxygenation conditions. 65

Table 8. Normalized major oxide values used for discriminant function. 75

Table 9. Results of rock-eval analysis of Calera Core samples. 77

Table 10. Relations among Tmax values, production indices, thermal maturity, and hydrocarbon generation (modified from Hunt, 1995). 78

Table 11. Relationship among kerogen types, organic matter sources, and hydrocarbon potential. 79

List of Figures

Figure 1. (A) Middle Ordovician paleogeographic map with NW to SE cross section line, illustrated in B. (B) Reconstruction of Middle Ordovician stratigraphy and facies relationships in Alabama (modified from Benson, 1986). 7

Figure 2. Generalized geological map across the Alabama fold-and thrust belt showing the locations of the Calera, Pratts Ferry and Vincent sections targeted for study. Map modified from Google Earth. 8

Figure 3. Location and general character of the Calera core section. (A) Google Earth image of the NE-11-18 core drill site at the Roberta Plant,Calera, Shelby County, Alabama (Oa = Athens Shale belt). (B, C) Examples of Athens Shale core from near the base (B) and top (C) of the section. Core box is approximately two feet long. 10

Figure 4. Photos of road-cut exposures of the Athens Shale at the Pratts Ferry (A) and Vincent (B) localities (author for scale). 12

Figure 5. Cycle of Rock-Eval pyrolysis and corresponding output. Modified from Tissot and Welte, (1984). 19

Figure 6. Example of modified Van Krevelen diagram. Modified from McCarthy et al., (2011) 21

Figure 7. Photograph of core interval 169-179 ft. (Box 14) which represents Lithofacies A. White box indicates intervals shown in detail in Figure 8. 28

Figure 8. Photographs of Lithofacies A expressed on external (A) and internal (B) core surfaces. 29

Figure 9. Photomicrographs of limestone nodules (A-C) and mudstone matrix (D) in Lithofacies A. (A) Packed biomicrite with microsparitic matrix (thin section CC-1). Allochem labeled E is an echinoderm fragment. (B) Sparse to packed biomicrite with relatively unaltered micritic matrix (thin section cc-1). Skeletal allochems are dominated by brachiopod fragments. (C) Packed biomicrite nodule surrounded by sparse biomicrite (thin section CC-2). (D) Calcareous mudstone interval showing variable abundance of skeletal allochems (thin section CC-3). 30

Figure 10. Photograph of core interval 159-169 ft. (Box 13) exemplifying Lithofacies B.White boxes indicate intervals shown in detail in Figure 11 32

Figure 11. Close up photographs of multiple thin limestone beds and intervening shales in Lithofacies B expressed on external (A, C) and internal (B, D) core surfaces. Small white arrows indicate narrow, calcite-healed fractures. 33

Figure 12. Photomicrographs of limestone (A-C) and shale (D,E) beds in Lithofacies B. (A) Biosparitic limestone grading upward into a packed biomicrite (thin section CC-5). (B) Packed biomicrites grading upward into sparse biomicrite (thin section CC-5). (C) Sparse biomicrite interval (thin section CC-6). (D) Homogeneous shale with dispersed skeletal allochems, carbonate silt grains, and pyrite. (E) Shale interval with irregular stringer of skeletal allochems (thin section CC-5). 34

Figure 13. Photograph of core interval 119-129 (Box 9) dominated by Lithofacies C. White boxes indicate intervals shown in detail in Figure 14 37

Figure 14. Close up photographs of thin limestone beds and laminae and dark gray shale expressed on internal (A,C) and external (B,D) core surfaces. Note sharp bases and gradational tops of beds in C. Small white arrows in A and B indicate narrow calcite-healed fracture. 38

Figure 15. Photomicrographs representing characteristic features of Lithofacies C. (A) Carbonate bed with thin, flattened enigmatic structure with fine-grained mud fill (thin section CC-17). (B) Carbonaceous shale interval (thin section CC-7). (C) Continuous, parallel carbonate laminae sets interbedded with carbonaceous shale (thin section CC-11). (D) Sets of carbonate silt laminae sets in shale (thin section CC-10). (E) Carbonaceous mud with spherical calcite filled structures (calcispheres?) in a carbonaceous shale interval (thin section CC-22). (F) Closer view of calcite filled bodies within a carbonaceous shale interval (thin section CC-22).....39

Figure 16. Photograph of core interval 49-59 (Box 2) exemplifying Lithofacies D. White boxes indicate intervals shown in detail in Figure 17. Arrow points to narrow, calcite-healed fracture.....42

Figure 17. Close up photographs of dark gray shale with thin limestone laminae in Lithofacies D expressed on external (A, C) and internal (B, D) core surfaces. Arrows in B and D highlight a few thin carbonate laminae.....43

Figure 18. Photomicrographs exemplifying Lithofacies D. (A) Thin, continuous, parallel carbonate laminae interbedded with carbonaceous shale (thin section CC- 32). (B) Shale with dispersed fine quartz silt grains (small arrows) and calcite- and pyrite-filled spherical structures (calcispheres?; large arrows) (thin section CC-32). (C) Shale with dispersed quartz silt grains (arrows) (thin section CC-37) (D) Carbonaceous shale with flattened lenses of fine grained mud perhaps representing compact burrow fills (thin section CC-41). (E) Carbonaceous shale with sub-horizontal, irregular calcite-filled ven (thin section CC-30). (F) Shale with pyrite euhedra surrounded by gypsum (thin section CC-27). 44

Figure 19. Carbonate/Organic carbon curves next to a generalized stratigraphic column of the Athens shale at the Calera Core section. 46

Figure 20. Outcrop photos of the Pratts Ferry section. (A) Interbedded limestones and darker gray, fissile shales. (B) Soft-sediment deformation in lower part of a limestone bed.....53

Figure 21. Photographs of slabbed block samples collected at the Pratts Ferry locale. (A) Thin carbonate laminae in calcareous shale. (B) Thin micritic limestone beds interbedded with calcareous shale. (C) Relative thick micritic limestone bed overlying calcareous shale with soft sediment deformation features (arrow). Cross Cutting linear features are saw marks (D) Interbedded carbonate and calcareous shale with localized small-scale deformational features.....54

Figure 22. Outcrop photos of the Vincent section. (A) Weathered platy shale in tight, nearly isoclinal fold. (B) Highly fractured, platy carbonaceous shale. 56

Figure 23. Photographs of polished block samples collected at Vincent section. (A) Apparently homogeneous carbonaceous, calcareous shale. (B) Calcareous shale with large pyrite concretion. (C) Thinly laminated limestone and calcareous shale cut by small-scale microfaults. (D) Thinly laminated limestone and calcareous shale. 57

Figure 24. Geochemical indices plotted next to carbonate/organic carbon curves and stratigraphic column. 66

Figure 25. C/S ratios for Athens shale samples plotted on the diagram of, and Raiswell and Canfield, (2012). 68

Figure 26. Athens Shale samples plotted on the mudrock provenance diagram of Roser and Korsch (1986). PM = passive margin, ACM = active continental margin, and ARC = oceanic island arc....72

Figure 27. Athens Shale samples plotted on Rosher and Korsch's (1988) discriminant function diagram using coefficients derived from oxide concentrations. Blue dots reflect plots of raw geochemical data. Yellow dots reflect plots of data normalized after exclusion of CaO. P1= mafic detritus, P2+ intermediate dominantly andesitic detritus; P3 = felsic plutonic and volcanic detritus, and P4 = recycled mature polycyclic quartzose detritus.

Discriminant function I = -1.773 TiO_2 + 0.607 Al_2O_3 + 0.76 $Fe_2O_{3(TOTAL)}$ – 1.5 MgO + 0.616 CaO + 0.509 Na_2O – 1.224 K_2O – 9.09;

Discriminant function II = 0.445 TiO_2 + 0.07 Al_2O_3 – 0.25 $Fe_2O_{3(TOTAL)}$ – 1.142 MgO + 0.438 CaO + 1.475 Na_2O + 1.426 K_2O – 6.861....73

Figure 28. Athens Shale samples plotted on Rosher and Korsch's (1988) discriminant function diagram using coefficients derived from oxide ratios.

Discriminant function I = 30.638 TiO_2 / Al_2O_3 – 12.541 $Fe_2O_{3(TOTAL)}$ / Al_2O_3 + 7.329 MgO / Al_2O_3 + 12.031 Na_2O / Al_2O_3 + 35.402 K_2O / Al_2O_3 – 6.382;

Discriminant function II = 56.500 TiO_2 / Al_2O_3 – 10.879 $Fe_2O_{3(TOTAL)}$ / Al_2O_3 + 30.875 MgO / Al_2O_3 – 5.404 Na_2O / Al_2O_3+ 11.112 K_2O / Al_2O_3 – 3.890....74

Figure 29. Athens Shale samples plotted on a modified Van Krevelen diagram....79

1. INTRODUCTION

The sedimentary rock record is dominated by mudrocks; i.e., strata with modal grain sizes less than 62.5 μm (Lazar et al., 2015). These include the common dark, carbonaceous rocks collectively referred to as black shales. These organic-rich mudrocks are important because they serve as the source rocks for most conventional hydrocarbon systems and, as evidenced by the recent developments in the shale-gas industry, they may serve as self-contained hydrocarbon systems in which they represent the source, reservoir, and seal (e.g. Klemme and Ulmishek,1991; Bohacs et al., 2005; Passey et al., 2010).

Given the significance of black shales to the petroleum industry, it is important to gain a firm understanding of their depositional environments and the processes that operated therein. In the past, black shales usually were attributed to slow deposition from suspension within relatively deep, quiet, anoxic basins. However, more recent studies of compositions, geochemistries, textures, sedimentary structures, and microfabrics demonstrate that black shales are heterogeneous and were deposited by a variety of processes, including those involving bedload transport, in basins of variable water depth and under a range of oxygenation levels (O'Brien, 1996; Stow et al., 2001; Schieber et al., 2007; Schieber and Southard, 2009; MacQuaker et al., 2010a, b; Hammes and Frebourg, 2012; Bohacs et al., 2014; Lazar et al., 2015). Understanding this

lithologic heterogeneity is important in assessing factors that impact both the generation and production of hydrocarbons (e.g., organic-richness, porosity and permeability, and fracturability) (Soeder, 1988; Gale et al., 2007; Engelder et al., 2009; Schieber, 2011).

The stratigraphic record of the southeastern U.S. includes several marine black shale units. In Alabama and adjacent states, these include the Cambrian Conasauga Formation, Ordovician Athens Shale, Devonian Chattanooga Shale, and Mississippian Floyd and Neal shales. The Conasauga, Chattanooga, and Neal/Floyd shales have been identified as potential hydrocarbon-source rocks and shale-gas prospects (Telle et al., 1987; Carroll et al., 1995; Pashin, 2008, 2009). Consequently, these three units, particularly the Chattanooga Shale, have been the subject of considerable study, and their environments and processes of deposition are reasonably well established (e.g., Schieber, 1994a, b, 1998; Haynes et al., 2010). In contrast, the Ordovician Athens Shale has received comparably little attention.

The primary objectives of this study are to (1) characterize in detail the mudrock lithofacies of the Athens Shale, (2) interpret the environmental conditions and processes that influenced Athens Shale deposition, and (3) assess the potential of the Athens Shale lithofacies as hydrocarbon-source rocks. These objectives were met mainly by detailed examination of a single Athens Shale core drilled near Calera, Alabama, but also via supplementary observations of surface exposures within the Appalachian fold-and-thrust belt of Alabama.

2. ATHENS SHALE

During the Middle Ordovician Taconic orogeny, the North American plate collided with a volcanic arc system. Under the load of an accreted terrane, lithospheric flexure and subsidence created a string of foreland basin depocenters in which Middle Ordovician strata accumulated (Rodgers, 1970; Read, 1980; Shanmugan and Walker, 1980) (Fig. 1A). The Athens Shale and its low-grade metamorphic equivalent in Georgia, the Rockmart Slate, represent the deep basinal facies deposited in the southernmost depocenter of this foreland basin system (Gleason et al., 2002).

Continuity of Middle Ordovician facies has been disrupted significantly by later Acadian and Alleghenian orogenic events, and various facies belts are now juxtaposed across thrust faults within the Alabama Valley-and-Ridge province (Fig. 1B). Nonetheless, previous workers, including Benson (1986) and Carter and Chowns (1986), have reconstructed the histories of basin development and deposition for the Middle Ordovician in the region (Fig. 1C). Throughout the region, Middle Ordovician strata rest unconformably on the karstified surface developed upon platform carbonates of the Late Cambrian-Early Ordovician Knox Group. In the western part of the region, toward the craton, shallow platform carbonate deposition resumed with the accumulation of the Chickamauga Group. Further southeast, basin development is reflected by

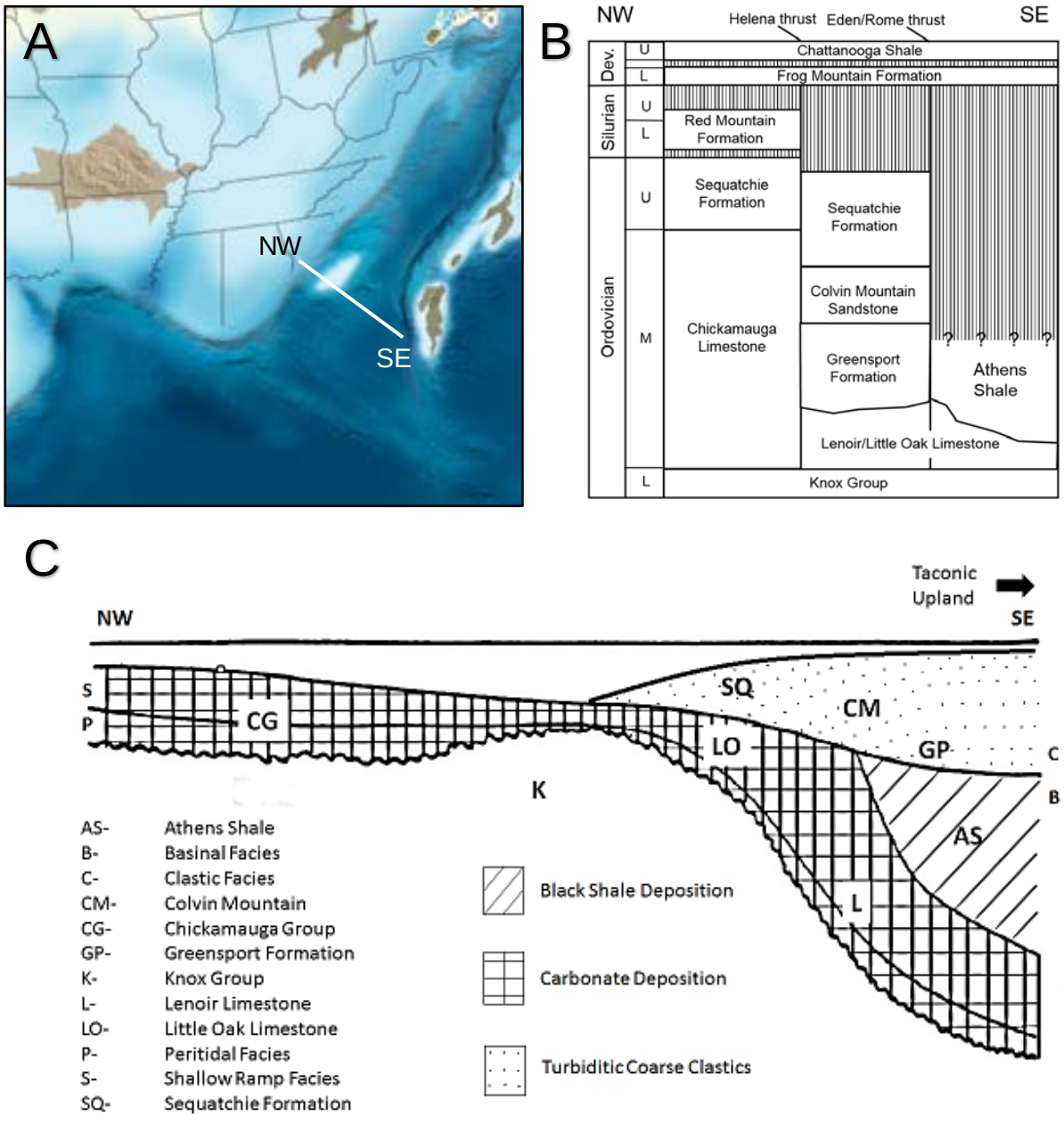

Figure 1. (A) Middle Ordovician paleogeographic map with NW to SE cross section line, illustrated in B. (B) Generalized Ordovician through Devonian stratigraphy in the Alabama Valley and Ridge in relation to major thrust faults associated with the Alleghenian orogeny (based on information in Benson, 1986; Raymond et al., 1988). (C) Reconstruction of Middle Ordovician stratigraphy and facies relationships in Alabama (modified from Benson, 1986).

deposition of shallow- to deep-ramp carbonates of the Lenoir and Little Oak limestones, which grade upward and eastward into the Athens Shale. Even further to the southeast, the Lenoir Limestone pinches out and the Athens (or equivalent Rockmart Slate) thickens and directly overlies Knox Group carbonates.

Continued Taconic orogenesis and related emergence eventually led to the deposition of the shallow-marine and terrestrial sediments of the Greensport, Colvin Mountain, and Sequatchie formations, which prograded southwestward over the Athens Shale and western carbonate platform facies. However, owing to late Taconic and subsequent Acadian orogenesis, the Athens Shale is now overlain unconformably by the Devonian Frog Mountain Sandstone or Chattanooga Shale (Fig. 1B). Due to pre-Devonian truncation and subsequent deformational and erosion events, thicknesses of Athens Shale successions are poorly established. Benson (1986) indicates that thicknesses range from 50-100 m and generally increase towards the southeast.

General lithologic descriptions of the Athens Shale have been provided by Benson and Mink (1983), Benson (1986), Carter and Chowns (1986), and Saunders and Savrda (1993). The lower part of the unit is gradational with the Lenoir and Little Oak limestones and consists of interbedded micritic limestones and calcareous shales, which locally exhibit soft-sediment deformational features reflecting basin-margin slope instability. The upper part of the Athens is dominated by dark gray to black, relatively carbonate-poor, thinly laminated, apparently unbioturbated, pyritiferous, graptolitic shales. In addition to graptolites,

the Athens Shale also contains rare brachiopods and trilobites locally (Benson, 1986). In places, the Athens Shale is cut by orthogonal hydrothermal veinlets filled with pyrite, calcite, barite, and quartz (Saunders and Savrda, 1993). The current thesis research represents a more detailed characterization of the sedimentology and geochemistry of the Athens Shale.

3. STUDY LOCATIONS

Outcrops of the Athens Shale typically are deeply weathered, locally highly structurally deformed, and expose only narrow intervals of the formation. Hence, most of the detailed sedimentologic and geochemical analyses reported herein focused on a relatively unweathered, continuous, 140-ft-thick (~43 m) core section of the Athens Shale recovered by drilling near Calera, Alabama (Calera core section). Nonetheless, after reconnaissance of Athens Shale surface exposures in Alabama, outcrops at two localities—the Vincent and Pratts Ferry sections—were selected for supplementary study. Locations of three sections are shown in Figure 2.

3.1 Calera Core Section

The Calera section is a 2”-diameter core section recovered during test drilling just east of a Newala Limestone quarry and cement plant (Roberta Plant) west-northwest of Calera, Shelby County, Alabama (Fig. 3). The core, designated NE-11-18 by Lafarge North America, the previous quarry operator that performed the drilling, was donated to the project by Argos USA Corporation, the current quarry operator. Drilling was oriented approximately normal to regional strike (~N35E 40-60° SE) and, after penetrating ~30 feet (~9 m) of weathered rock, recovered ~140 feet (~43 m) of Athens Shale and its transition to the underlying Lenoir Limestone. Notably, a comparable interval of Athens Shale is exposed in a quarry just south of the NE-11-18 drilling site.

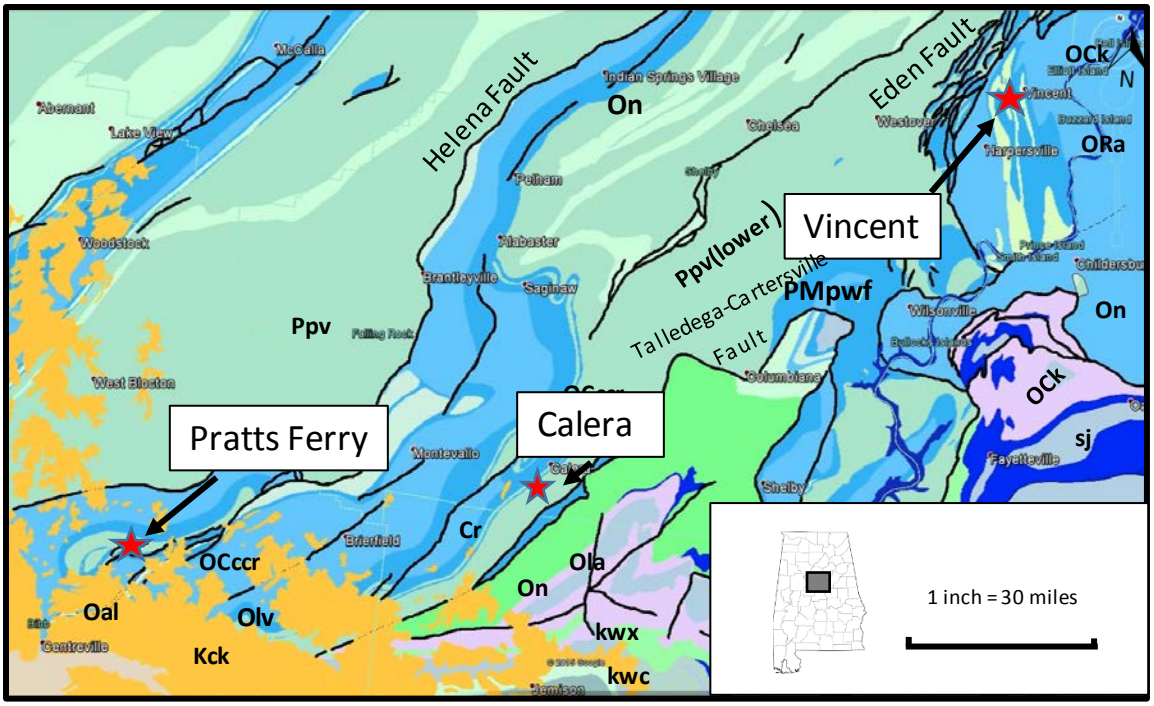

Kck: Coker Formation
Ppv : Pottsville Formation
PMpwf: Parkwood Formation and Floyd Shale Undiffernitaited
Oal: Athens Shale and Lenoir Limestone Undifferentiated
Ock: Knox Group
Occcr: Chepultec and Copper Ridge Dolomites Undifferntiated
Olv: Longview Limestone
On: Newala Limestone

ORa: Athens Shale
Cr: Rome Formation
kwc: Wash Creek Slate
kwx: Waxahatchee Slate
sj: Sylacauga Marble Group

Localities

Faults

Figure 2. Generalized geological map across the Alabama fold-and thrust belt showing the locations of the Calera, Pratts Ferry and Vincent sections targeted for study. Map modified from Google Earth.

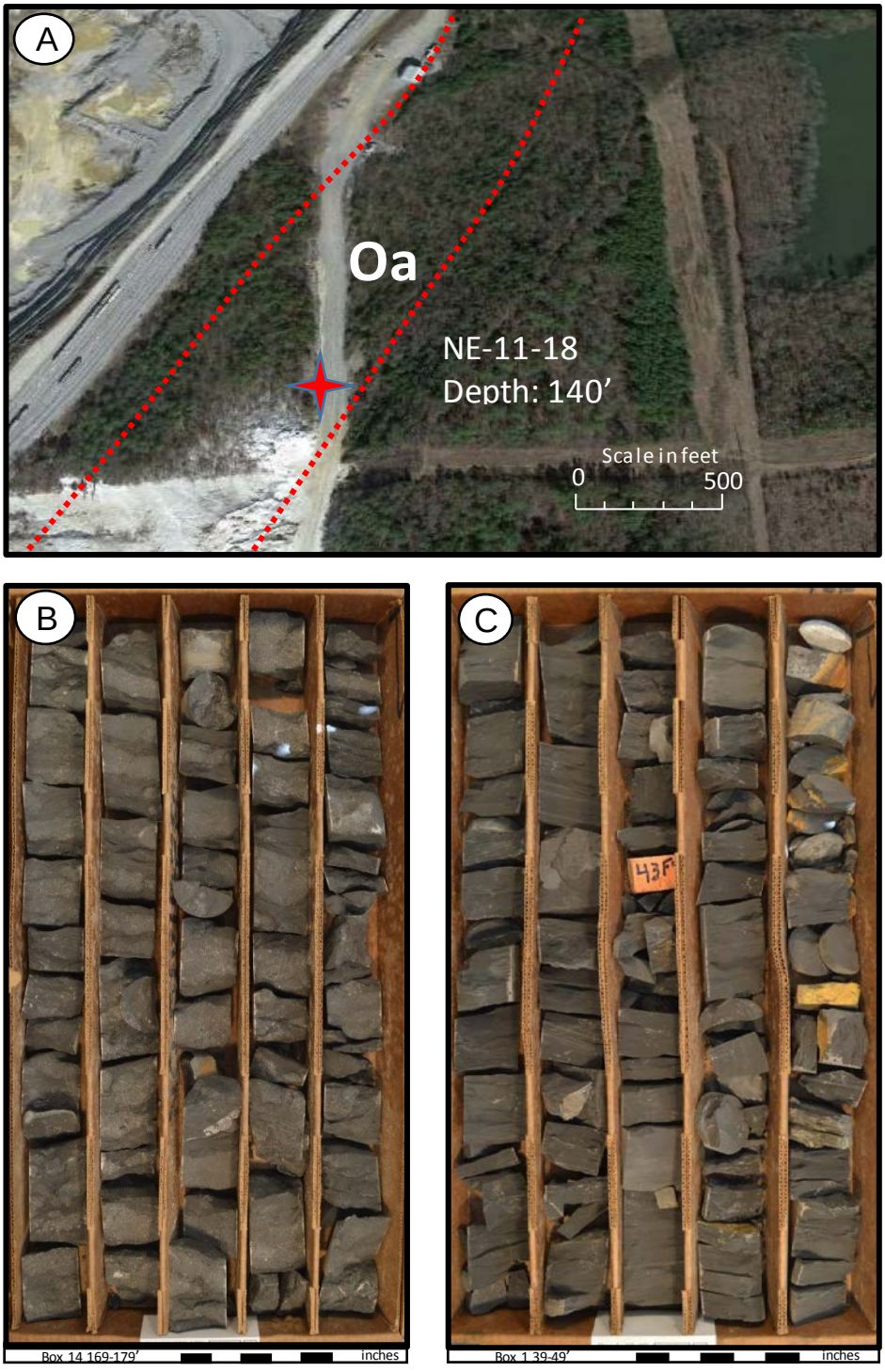

Figure 3. Location and general character of the Calera core section. (A) Google Earth image of the NE-11-18 core drill site at the Roberta Plant, Calera, Shelby County, Alabama (Oa = Athens Shale belt). (B, C) Examples of Athens Shale core from near the base (B) and top (C) of the section. Core box is approximately two feet long.

These exposures, now inaccessible due to safety concerns, were described by Benson (1986; fieldtrip stop 8). Exposures purportedly include ~75 m (~246 ft) of Athens Shale extending from its basal contact with the Lenoir Limestone to its upper contact with the Frog Mountain Sandstone. Benson (1986) describes the Athens Shale here as dark gray to black, graptolitic, pyritiferous shale with common argillaceous limestone interbeds towards the base. According to Gleason et al. (2002), the calera exposure includes the *Hustedograptus teretiusculus* and lower *Nemograptus gracilis* graptolite zones.

3.2 Surface Exposures

The Vincent and Pratts Ferry sections are road-cut exposures that include relatively thin intervals of the Athens Shale. The Pratts Ferry section occurs along the south side of Bibb County Road 27 just east of the Pratts Ferry bridge across the Cahaba River, ~5 miles north of Centreville, Bibb County, Alabama (Fig. 4A). Previously described by Benson (1986; fieldtrip stop 9), exposures here reflect the transition from basin-margin facies of the Lenoir Limestone (Pratts Ferry beds) to deeper basinal deposits of the lower part (~15-20 m; 50-65 feet) of the Athens Shale. While exposures are generally good, shalier intervals are more highly weathered. Benson (1986) describes the Athens Shale here as interbedded calcareous mudstones and dark gray, fissile, laminated shales with rare graptolites and other invertebrate body fossils (brachiopods, trilobites, and ostracods) and localized soft-sediment deformational features (Benson, 1986).

Figure 4. Photos of road-cut exposures of the Athens Shale at the Pratts Ferry (A) and Vincent (B) localities (author for scale).

The Vincent section refers to exposures of the Athens Shale on the north side of Highway 231 just east of its intersection with Shelby County Road 83 in the town of Vincent, Shelby County, Alabama (Fig. 4B). Here, the Athens Shale occurs in a north-northwest-trending syncline near the leading edge of the Pell City thrust sheet. The exposure is approximately 67 meters (~220 feet) long and reaches a maximum height of 3.5 m (~11 feet). The section is highly weathered and locally heavily vegetated, particularly at the eastern end of the outcrop. Structural deformation reflected by tight, small-scale folds and shear planes preclude accurate determination of stratigraphic thickness of the Athens Shale. Moreover, the precise stratigraphic position of these strata within the Athens Shale is unclear. Gleason et al. (2002) reported graptolites of the *Didymograptus murchissoni* zone from this locality suggesting that the rocks are from the lower part of the Athens.

4. METHODS

4.1 Calera Core

4.1.1 Core Descriptions and Sampling

The Calera core boxes were laid out in ascending order in the lab, photographed, and examined with the naked eye, hand lens, and binocular microscope. Descriptions and digital photographic records were made of general lithology, bedding, sedimentary structures and textures, fossil content, and diagenetic features based on observations of exterior and split interior surfaces of all core segments as well as available bedding-parallel parting surfaces. Observations were integrated in order to provisionally delineate mudrock lithofacies.

Following core description, the Calera section was systematically sampled for the thin-section studies and carbonate, organic carbon, whole-rock geochemical, and rock-eval analyses described below. Photographs of the entire Calera core showing the positions of close-up photographs and sampling horizons are provided in Appendix A.

4.1.2 Thin-Section Petrography

A total of 54 thin sections were produced commercially by Wagner Petrographic LLC (Lindon, Utah) from strategically collected samples from various intervals of the Calera core (see Appendix A for thin-section sample horizons). Thirty-two samples were prepared as standard-size (1 x 1 7/8”) thin

sections. In order to better characterize larger bedding features, the remaining 22 samples were prepared as large-format (2 x 3") thin sections.

Thin sections were examined under a petrographic microscope at various magnifications to better characterize sedimentary structures, composition, and textures. Digital photomicrographs were taken to document various features that aided in the characterization and interpretation of lithofacies.

4.1.3 Carbonate and Organic Carbon Analyses

Carbonate and organic carbon (TOC) contents of the Athens Shale were determined using a combination of acid-digestion and combustion techniques. One hundred and forty (140) samples were collected at ~1 ft (~30.5 cm) intervals throughout the Calera core section (see Appendix A). Sampling and sample powdering were completed simultaneously using a power drill equipped with a carbide-tipped bit. Approximately 0.5 g of powder were extracted from each sample horizon.

Powdered subsamples, each weighing ~0.25 g, were digested in 10% HCL and then filtered through pre-weighed, carbon-free borosilicate glass filters using a vacuum apparatus. Filters and insoluble residues were dried at 100°C in an oven for ~24 hours. After drying, filters with residues were reweighed, and carbonate content (weight percent $CaCO_3$) was determined by weight loss.

Organic carbon contents were determined for the same 140 samples by combustion of filters + residues. Filters with residues were disaggregated, individually wrapped in tin foil to form near spherical masses, and analyzed using

an Elementar Verio Macro Carbon/Nitrogen Analyzer at the ALFA Agricultural Services and Research Center at Auburn University. In this analyzer, catalytic combustion is carried out at a temperature of 1050°C. Resulting combustion gases are separated into their components via purge and trap chromatography and detected by a thermal conductivity detector (TCD). Carbon contents are computed based on evolved CO_2 in relation to the initial subsample weights prior to acid digestion.

4.1.4 Whole-Rock Geochemical Analyses

Twelve (12) samples from the Calera core section, each ~3 cm^3 in size, were selected for commercial geochemical analysis; ten samples were derived from shalier intervals distributed throughout the core, while the remaining two samples were derived from limestones in the lower parts of the core (see Appendix D). Samples were sent to Bureau Veritas Minerals in Vancouver, Canada, where they were pulverized to a fine powder (~3.75 phi). All 12 samples were subjected to inductively coupled mass and emission spectrometry (ICP-ES/MS). Subsamples weighing ~1 gram were digested with aqua regia (usually a mixture of HNO_3 and HCL) for two hours at 95°C. After cooling and dilution with deionized water, samples were analyzed using laser ablation and ICP-ES/MS to determine the concentrations of thirty-five (35) elements (see Table 1). The 10 shale samples also were subjected to whole-rock lithogeochemistry. Subsamples weighing ~5 grams were digested through robotic fusion technology, laser ablated, and analyzed via ICP-MS to determine the concentrations of 21 parameters (e.g., major oxides, LECO C and S; see Table 2).

Table 1. Representative geochemical proxies with detection limits for aqua regia ICP-ES/MS analyses.

Element	Detection	Upper Limit	Element	Detection	Upper Limit
Ag	0.5 ppm	1000 ppm	***Mo***	0.5 ppm	50000 ppm
Al	0.01%	40%	***Na***	0.01 %	25 %
As	5 ppm	100000 ppm	***Ni***	0.5 ppm	100000 ppm
Ba	5 ppm	5000 ppm	***P***	0.001 %	25 %
Bi	0.5 ppm	10000 ppm	***Pb***	0.5 ppm	40000 ppm
Ca	0.01 %	40%	***S***	0.05 %	30 %
Cd	0.5 ppm	10000 ppm	***Sb***	0.5 ppm	50000 ppm
Co	0.5 ppm	10000 ppm	***Sc***	0.5 ppm	500 ppm
Cr	0.5 ppm	50000 ppm	***Se***	2 ppm	500 ppm
Cu	0.5 ppm	100000 ppm	***Sr***	5 ppm	10000 ppm
Fe	0.01 %	40 %	***Th***	0.5 ppm	10000 ppm
Ga	5 ppm	5000 ppm	***Ti***	0.001 %	10 %
Hg	0.05 ppm	10000 ppm	***Tl***	0.5 ppm	5000 ppm
K	0.01 %	40 %	***U***	0.5 ppm	10000 ppm
La	0.5 ppm	5000 ppm	***V***	10 ppm	50000 ppm
Mg	0.01 %	40 %	***W***	0.5 ppm	10000 ppm
Mn	5 ppm	200000 ppm	***Zn***	5 ppm	200000 ppm

Table 2. Representative geochemical proxies for whole-rock ICP-MS analysis.

Element	*Detection Limit*	*Upper Limit*
SiO_2	0.01 %	100%
Al_2O_3	0.01 %	100 %
CaO	0.01 %	100 %
Cr_2O_3	0.002 %	100 %
Fe_2O_3	0.045	100 %
K_2O	0.01 %	100 %
MgO	0.01 %	100 %
MnO	0.01 %	100 %
Na_2O	0.01 %	100 %
P_2O_5	0.01 %	100 %
TiO_2	0.01 %	100 %
Ba	5 ppm	5 %
Nb	5 ppm	1,000 ppm
Ni	20 ppm	10,000 ppm
Sc	1 ppm	10,000 ppm
Sr	2 ppm	50,000 ppm
Y	3 ppm	50,000 ppm
Zr	5 ppm	50,000 ppm
C	0.02 %	100 %
S	0.02 %	100 %

4.1.5 Rock-Eval Pyrolysis

To provide a complete source-rock screening of the Athens Shale, ten samples were selected for commercial source-rock analysis. Analyses included LECO carbon analysis and Rock-eval pyrolysis. Eight samples were taken from dark, shalier intervals within the Calera core section (with an average spacing of 18 feet; see Appendix A). Samples, each measuring ~3 cm^3, were sent to Weatherford Laboratories in Houston, Texas, where they were pulverized to a fine powder prior to analysis.

For total organic carbon (TOC) analyses, 80-100 mg of powdered sample were first acid-digested to remove all mineral carbon. The residue was then dried and analyzed using a LECO C744 Carbon Analyzer. In these analyses, samples were combusted in an induction furnace, in an oxidizing environment. CO_2 eluted from the sample was measured by a non-dispersive infrared detection (NDIR) cell and reported as weight % TOC.

Additional ~80 mg subsamples were subjected to Rock-eval analysis using a Total Potential Hydrocarbons Total Organic Carbon source rock analyzer. In Rock-eval analysis, samples undergo pyrolysis—i.e., thermochemical decomposition–during programmed heating through a temperature of ~650°C within a stable atmosphere. An example of the cycle of analysis and corresponding output is shown in Figure 5. The sample is held

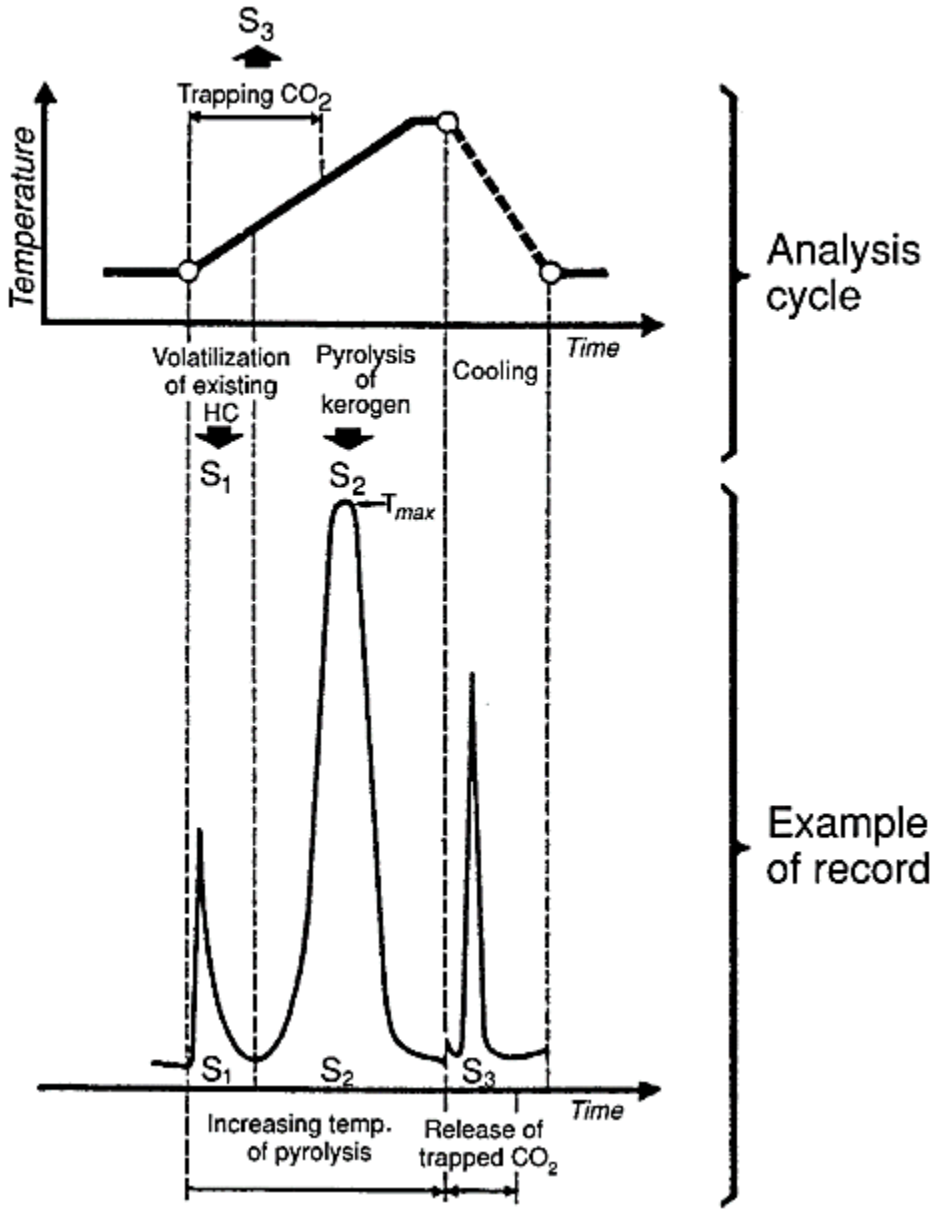

Figure 5. Cycle of Rock-eval pyrolysis and corresponding output. Modified from Tissot and Welte, (1984).

isothermally at 300°C for three minutes at which point S1 is determined. S1 is the amount of volatized hydrocarbons already present in free state or adsorbed in the sample, measured in milligrams of hydrocarbon/gram of rock. The oven temperature is then increased at a rate of 25°C/minute to the final temperature of 650°C and held isothermally for one minute. During the temperature increase, S2 is measured. S2 is the amount of hydrocarbons, measured in milligrams of hydrocarbon/gram of rock, generated by kerogen pyrolysis and is an indication of the quantity of hydrocarbons that the rock potentially could produce. The temperature at the S2 peak is measured and recorded as Tmax, the temperature at peak generation of hydrocarbons. Tmax is an indication of the thermal maturation state of the organic matter in the sample; Tmax increases with increasing maturity. As the temperature is subsequently lowered (to between 300 and 390°C), S3 is measured by NDIR cells. S3 measures the amount of CO_2 (in milligrams CO_2 per gram of rock) released from kerogen pyrolysis, and also is an indication of the amount of oxygen in the kerogen.

Additional parameters provided by Rock-eval analysis include the production index (PI; aka transformation index) and hydrogen (HI) and oxygen (OI) indices. The production Index, determined as PI = S1/ [S1+S2], is another measure of thermal maturity. HI and OI, measures of the H and O contents of organic matter, are calculated as HI = (100*S2)]/TOC) and OI = [100*S3]/TOC, respectively. Plotted together on a modified Van Krevelen Diagram (Fig. 6), HI and OI may be used to determine the type of organic matter in a sample

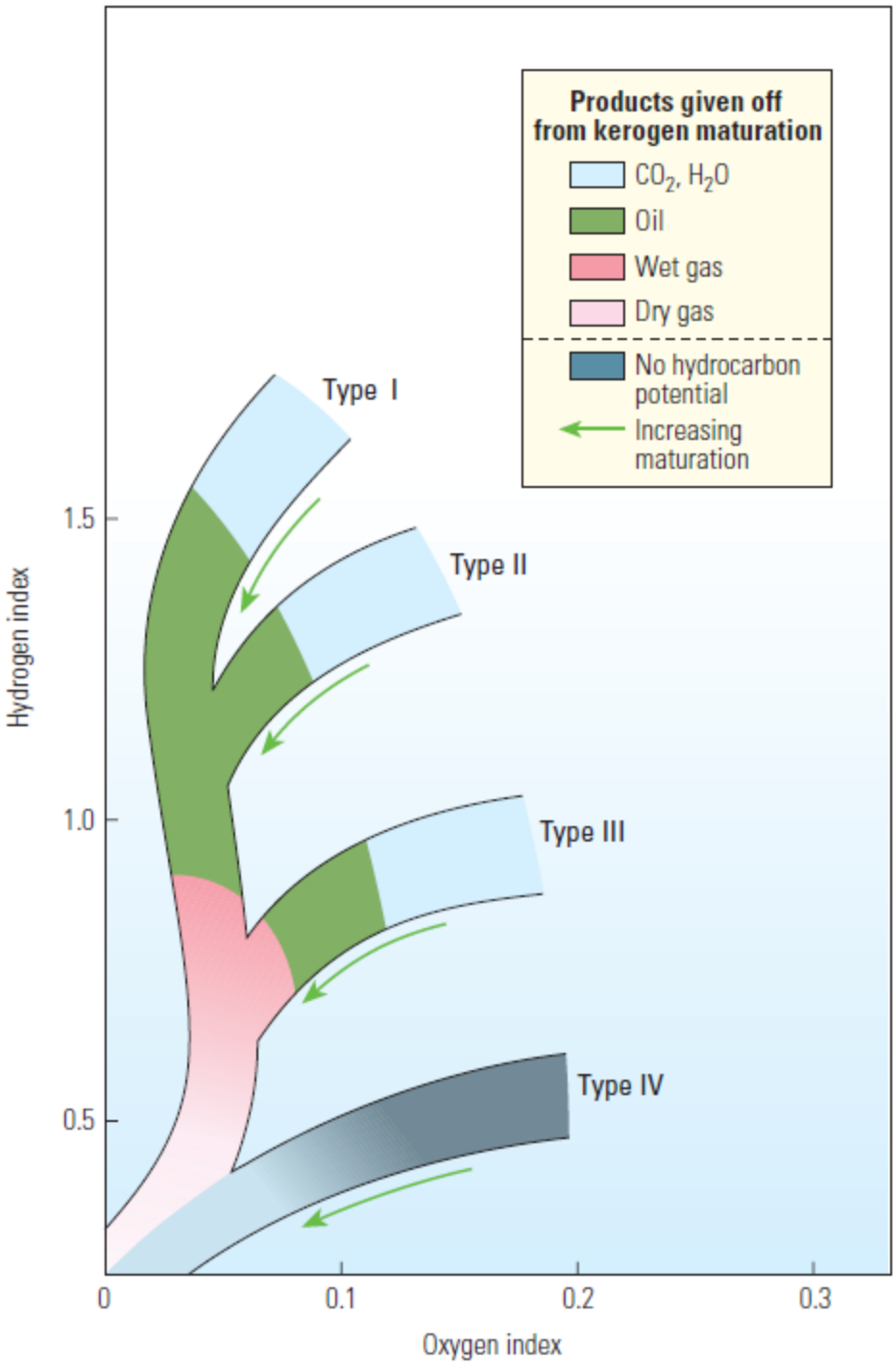

Figure 6. Example of modified Van Krevelen diagram. Modified from McCarthy et al. (2011).

(kerogen type; e.g., liptinite, vitrinite, inertinite) as well as its thermal maturity. For examples, oil-prone, lipid-rich organic matter with high H/C ratios (cyanobacteria, marine algae) has high HI and low OI, while more gas-prone, carbohydrate-rich terrestrial plant material (vitrinite) has lower HI and high OI. However, both HI and OI decrease with thermal maturation.

4.2 Supplementary Outcrop Studies

The Vincent and Pratts Ferry road-cut sections of the Athens Shale were described in as much detail as possible in the field. Sedimentary features were photographed and a series of block samples were collected for more detailed examination in the laboratory. Twenty-nine (29) and thirty-three (33) oriented block samples were collected at ~1-m and 50-cm spacings at the Vincent (V-1 through V-29) and Pratts Ferry (PF-1 through PF-33) sections, respectively. Blocks were wrapped in duct tape to limit disaggregation and then cut perpendicular to bedding with a 24" Covington Engineering slab saw housed in the Department of Geosciences at Auburn University. Selected cut block surfaces were polished with various grits, photographed, and examined with the naked eye and under a binocular microscope to better characterize primary, biogenic, and diagenetic features. Observations were compared with that of the Calera core section.

5. LITHOFACIES

5.1 Lithofacies Descriptions

Observations of the Calera core, combined with carbonate and organic carbon data (Table 3) for the 140 samples, resulted in the recognition of four broad lithofacies. Each of these lithofacies, herein referred to Lithofacies A through D, are described below.

5.1.1 Lithofacies A- Nodular Limestone in Calcareous Mudstone

Core intervals assigned to Lithofacies A comprise nodular masses of medium gray limestone within a matrix of very dark gray, calcareous mudstone (Fig. 7). Limestone nodules, which represent 50% to 80% by volume of these intervals, have an average $CaCO_3$ content of 82% (range = 79.8-84.3%) and low TOC contents (0.29-0.67%; average = 0.42%). Nodules are subrounded to subangular and highly variable in gross shape; some are irregularly ovate but most appear to have highly complex three-dimensional geometries. Long axes of nodules vary from 1 cm to >8 cm (Fig. 8). Boundaries between nodules and intervening mudstone matrices range from sharp to diffuse.

Petrographic examination indicates that the limestones in the nodules are sparse to packed biomicrites (fossiliferous wacke- and packstones) (Fig. 9A-C).

Table 3. Carbonate and organic carbon data for all 140 Calera Core samples (ND = no data due to operator error).

Sample #	Sample depth (ft)	Facies	Lithology	Carbonate %	Organic Carbon %
1.5.18	139.5	D	Mudstone	18.74	1.13
1.5.6	138.5	D	Mudstone	24.86	0.99
1.4.18	137.5	D	Mudstone	42.49	0.85
1.4.6	136.5	D	Mudstone	25.32	0.99
1.3.18	135.5	D	Mudstone	28.26	1.07
1.3.6	134.5	D	Mudstone	29.69	0.94
1.2.18	133.5	D	Mudstone	27.29	1.13
1.2.6	132.5	D	Mudstone	31.00	1.03
1.1.18	133.5	D	Mudstone	26.72	1.24
1.1.6	130.5	D	Mudstone	25.12	1.21
2.5.18	129.5	D	Mudstone	34.85	0.97
2.5.6	128.5	D	Mudstone	27.57	1.15
2.4.18	127.5	D	Mudstone	24.40	1.24
2.4.6	126.5	D	Mudstone	26.67	1.09
2.3.18	125.5	D	Mudstone	26.03	1.01
2.3.6	124.5	D	Mudstone	30.70	1.02
2.2.18	123.5	D	Mudstone	23.16	1.27
2.2.6	122.5	D	Mudstone	37.77	1.05
2.1.18	121.5	D	Mudstone	28.67	0.98
2.1.7	120.5	D	Mudstone	31.08	1.02
3.5.18	119.5	D	Mudstone	24.43	1.11
3.5.7	118.5	D	Mudstone	31.84	1.17
3.4.18	117.5	D	Mudstone	24.69	1.10
3.4.6	116.5	D	Mudstone	24.00	1.10
3.3.18	115.5	D	Mudstone	29.28	1.10
3.3.6	114.5	D	Mudstone	18.31	1.33
3.2.18	113.5	D	Mudstone	43.85	0.91
3.2.6	112.5	D	Mudstone	21.62	ND
3.1.18	111.5	D	Mudstone	24.80	ND
3.1.6	110.5	D	Mudstone	23.78	1.11
4.5.18	109.5	D	Mudstone	21.76	1.09
4.5.6	108.5	D	Mudstone	18.67	1.05
4.4.18	107.5	D	Mudstone	22.09	1.00
4.4.6	106.5	D	Mudstone	16.44	ND
4.3.18	105.5	D	Mudstone	15.97	1.05
4.3.6	104.5	D	Mudstone	15.45	2.23
4.2.18	103.5	D	Mudstone	18.53	1.07
4.2.6	102.5	D	Mudstone	14.02	1.16

4.1.18	101.5	D	Mudstone	22.23	ND
4.1.5	100.5	D	Mudstone	32.11	ND
5.5.18	99.5	D	Mudstone	17.14	1.58
5.5.6	98.5	D	Mudstone	18.48	1.40
5.4.18	97.5	D	Mudstone	18.38	1.27
5.4.6	96.5	D	Mudstone	20.75	1.13
5.3.18	95.5	D	Mudstone	23.12	1.08
5.3.6	94.5	D	Mudstone	24.94	1.15
5.2.18	93.5	D	Mudstone	19.43	1.21
5.2.6	92.5	D	Mudstone	24.31	1.25
5.1.18	91.5	D	Mudstone	21.90	1.09
5.1.5	90.5	D	Mudstone	34.95	0.90
6.5.19	89.5	D	Mudstone	27.47	1.76
6.5.6	88.5	D	Mudstone	47.82	1.03
6.4.18	87.5	D	Mudstone	27.05	1.46
6.4.6	86.5	D	Mudstone	37.09	1.28
6.3.18	85.5	D	Mudstone	25.81	1.38
6.3.6	84.5	D	Mudstone	31.02	1.28
6.2.18	83.5	D	Mudstone	21.29	ND
6.2.6	82.5	D	Mudstone	36.87	ND
6.1.18	81.5	D	Mudstone	31.69	0.94
6.1.6	80.5	D	Mudstone	22.48	1.10
7.5.18	79.5	D	Mudstone	28.86	1.08
7.5.6	78.5	D	Mudstone	25.11	1.09
7.4.18	77.5	D	Mudstone	31.58	0.89
7.4.6	76.5	D	Mudstone	22.65	1.04
7.3.18	75.5	D	Mudstone	29.29	1.00
7.3.6	74.5	C	Mudstone	24.73	1.14
7.2.18	73.5	C	Mudstone	37.75	0.89
7.2.6	72.5	C	Mudstone	23.41	1.08
7.1.18	71.5	C	Mudstone	26.24	1.07
7.1.6	70.5	C	Mudstone	21.87	1.11
8.5.18	69.5	C	Mudstone	25.81	1.10
8.5.6	68.5	C	Mudstone	41.05	0.82
8.4.17	67.5	C	Mudstone	24.67	1.07
8.4.6	66.5	C	Mudstone	25.25	1.12
8.3.18	65.5	C	Mudstone	24.69	1.14
8.3.6	64.5	C	Mudstone	23.04	1.20
8.2.18	63.5	C	Mudstone	21.52	1.03
8.2.6	62.5	C	Mudstone	19.50	1.24
8.1.21	61.5	C	Mudstone	38.13	1.01

8.1.8	60.5	C	Mudstone	24.72	1.14
9.5.18	59.5	C	Mudstone	22.02	1.19
9.5.6	58.5	C	Mudstone	36.30	0.95
9.4.20	57.5	C	Mudstone	25.50	1.14
9.4.6	56.5	C	Mudstone	22.68	1.20
9.3.18	55.5	C	Mudstone	28.16	1.28
9.3.8	54.5	C	Mudstone	23.02	1.21
9.2.18	53.5	C	Mudstone	27.78	1.00
9.2.6	52.5	C	Mudstone	22.35	1.39
9.1.18	51.5	C	Mudstone	24.87	1.12
9.1.6	50.5	C	Mudstone	20.27	1.34
10.5.18	49.5	C	Mudstone	24.26	1.23
10.5.6	48.5	C	Mudstone	20.47	1.27
10.4.18	47.5	C	Mudstone	24.73	1.01
10.4.6	46.5	C	Mudstone	26.86	0.89
10.3.18	45.5	C	Limestone	68.00	0.32
10.3.6	44.5	C	Limestone	58.60	0.40
10.2.18	43.5	C	Mudstone	22.86	1.23
10.2.6	42.5	C	Limestone	67.10	0.40
10.1.18	41.5	C	Mudstone	26.69	1.12
10.1.6	40.5	C	Limestone	69.16	1.20
11.5.18	39.5	C	Mudstone	31.94	1.03
11.5.6	38.5	C	Mudstone	28.10	1.43
11.4.18	37.5	C	Mudstone	33.62	1.18
11.4.6	36.5	C	Mudstone	35.20	1.13
11.3.18	35.5	C	Mudstone	35.95	1.16
11.3.6	34.5	C	Mudstone	35.41	1.37
11.2.18	33.5	C	Limestone	68.83	1.37
11.2.6	32.5	C	Mudstone	41.76	0.80
11.1.18	31.5	C	Mudstone	34.38	1.05
11.1.6	30.5	C	Mudstone	47.44	0.85
12.5.18	29.5	B	Mudstone	24.50	1.06
12.5.6	28.5	B	Mudstone	35.63	0.98
12.4.20	27.5	B	Mudstone	26.06	1.06
12.4.6	26.5	B	Mudstone	38.25	0.88
12.3.18	25.5	B	Limestone	59.98	2.18
12.3.7	24.5	B	Mudstone	37.90	0.89
12.2.18	23.5	B	Mudstone	37.20	0.95
12.2.6	22.5	B	Limestone	73.67	0.46
12.1.18	21.5	B	Mudstone	36.33	0.93
12.1.6	20.5	B	Mudstone	28.05	1.12

13.5.18	19.5	B	Mudstone	23.52	1.15
13.5.6	18.5	B	Limestone	83.31	0.58
13.4.18	17.5	B	Limestone	74.91	0.46
13.4.6	16.5	B	Mudstone	20.84	0.94
13.3.18	15.5	B	Mudstone	32.15	0.93
13.3.6	14.5	B	Mudstone	29.02	0.94
13.2.18	13.5	B	Limestone	80.29	0.40
13.2.6	12.5	B	Mudstone	33.38	0.78
13.1.18	11.5	B	Limestone	88.30	0.33
13.1.6	10.5	B	Limestone	83.14	0.37
14.5.18	9.5	A	Limestone	77.29	0.36
14.5.7	8.5	A	Limestone	67.49	0.67
14.4.18	7.5	A	Mudstone	43.89	0.57
14.4.6	6.5	A	Limestone	56.21	0.43
14.3.18	5.5	A	Limestone	79.76	0.34
14.3.6	4.5	A	Mudstone	40.28	0.53
14.2.18	3.5	A	Limestone	53.40	0.47
14.2.6	2.5	A	Limestone	84.29	0.29
14.1.18	1.5	A	Limestone	57.81	0.38
14.1.6	0.5	A	Limestone	52.40	0.43

Figure 7. Photograph of core interval 169-179 ft. (Box 14) exemplifying Lithofacies A. White box indicates interval shown in detail in Figure 8.

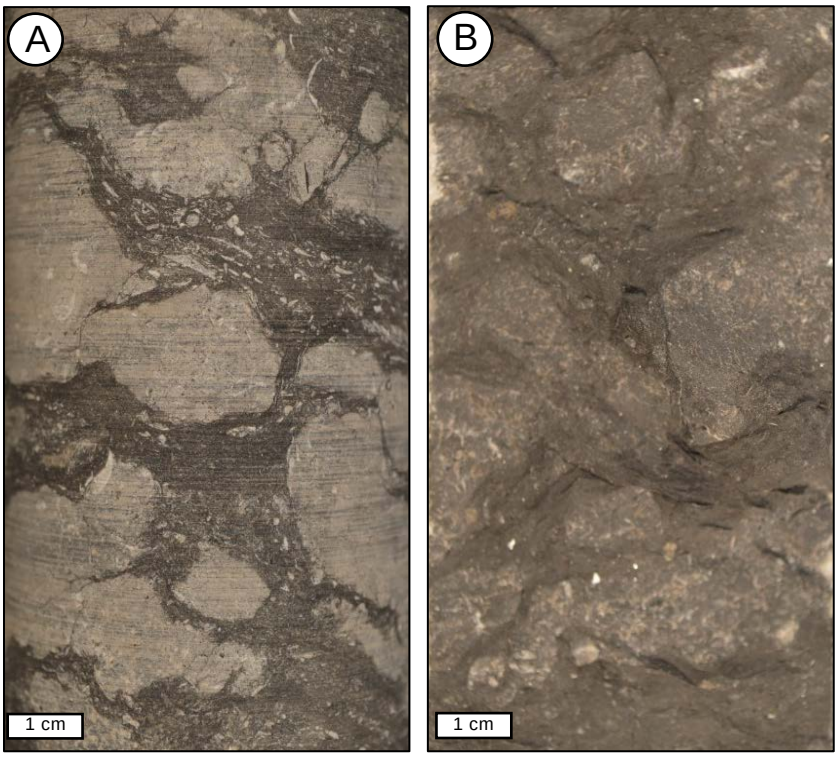

Figure 8. Photographs of Lithofacies A expressed on external (A) and internal (B) core surfaces.

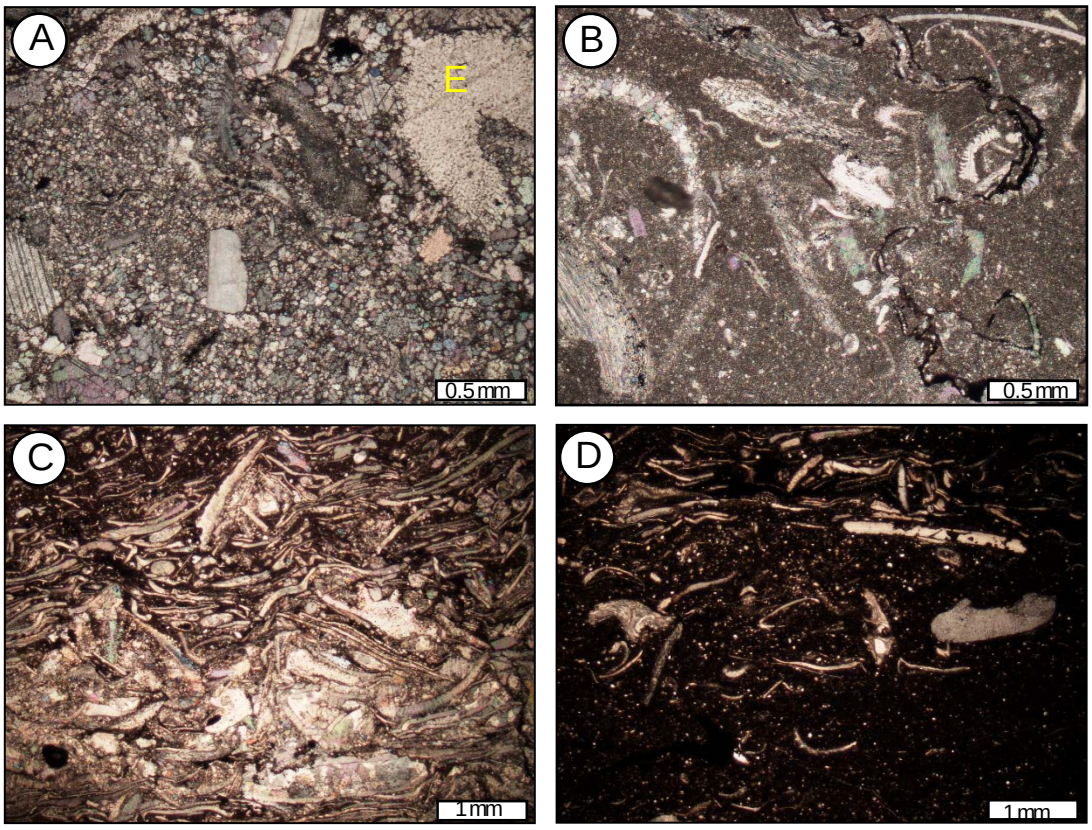

Figure 9. Photomicrographs of limestone nodules (A-C) and mudstone matrix (D) in Lithofacies A. (A) Packed biomicrite with microsparitic matrix (thin section CC-1). Allochem labeled E is an echinoderm fragment. (B) Sparse to packed biomicrite with relatively unaltered micritic matrix (thin section CC-1). Skeletal allochems are dominated by brachiopod fragments. (C) Packed biomicrite nodule surrounded by sparse biomicrite (thin section CC-2). (D) Calcareous mudstone interval showing variable abundance of skeletal allochems (thin section CC-3).

Identifiable skeletal allochems include crinoid, brachiopod, bryozoan, and trilobite fragments. Allochems are surrounded by a micritic matrix that in some nodules has been recrystallized to microspar (Fig. 9A).

Mudstone matrices between nodules are relatively clastic-rich; $CaCO_3$ contents range from 40.3 to 77.3% and average 56%, depending on the abundance of dispersed skeletal allochems and unidentifiable silt-sized carbonate grains. Skeletal allochems in the mudstones are similar to those in the limestone nodules (Fig. 9D). Mudstones are characterized by homogeneous to contorted fabrics. Contorted fabrics are best expressed where elongate skeletal fragments are abundant and roughly conform in orientation to nodule margins (e.g., see Fig. 9C). No burrows or other evidence for bioturbation are apparent. Mudstones are only slightly carbonaceous (average TOC = 0.55%) and locally contain pyrite nodules and lenses.

5.1.2 Lithofacies B- Carbonaceous Shale with Thin- to Medium-Bedded Limestones

Lithofacies B is characterized by interbedded medium gray, variably argillaceous limestone and dark gray, calcareous, carbonaceous shale (Fig. 10). Limestone beds, which have $CaCO_3$ contents ranging from 74 to 88% (average = 81%) and TOC contents of 0.33 to 0.58% (average = 0.43%), make up approximately 30% of this lithofacies by volume and range from 1 to 15 cm thick (average thickness = 4.75 cm). Their bases are generally sharp, while bed tops are typically gradational with overlying shales (Fig. 11). Limestones are normally

Figure 10. Photograph of core interval 159-169 ft. (Box 13) exemplifying Lithofacies B. White boxes indicate intervals shown in detail in Figure 11.

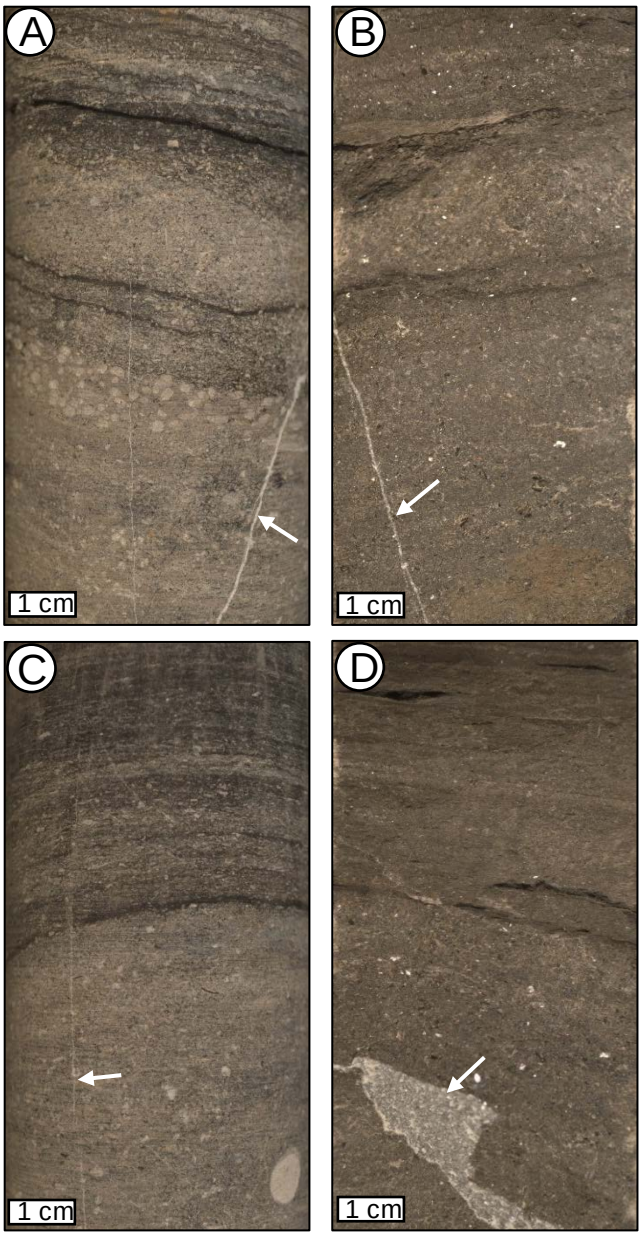

Figure 11. Close up photographs of multiple thin limestone beds and intervening shales in Lithofacies B expressed on external (A, C) and internal (B, D) core surfaces. Small white arrows indicate narrow, calcite-healed fractures.

graded, reflecting upward decreases in skeletal allochems and increases in mud; they typically transition gradually upward from biosparites (fossiliferous grainstones), through packed biomicrites (fossiliferous packstones) (Fig. 12A-B), to sparse biomicrites (fossiliferous wackstones; Fig. 12C). Although many of the skeletal allochems cannot be identified, recognizable forms are similar to those found in Lithofacies A, including echinoderm (crinoid? ossicles), brachiopod, bivalve, and trilobite fragments (Fig. 12A-D).

Carbonaceous intervals between limestone beds range from < 1 cm to 1 dm in thickness. Organic carbon contents range from 0.78 to 1.15% (average = 0.97%) Carbonate contents vary from 20 to 33% (average = 27%), reflecting differences in abundance of sand-sized skeletal allochems like those in the limestones and unidentifiable carbonate silt grains. In thicker shale intervals, skeletal allochems are relatively sparse and randomly distributed (Fig. 12D). However, thin stringers of concentrated skeletal material locally occur and are particularly common in thin shales between closely-spaced limestones (Fig. 12E). With the exception of the skeletal stringers, shales are apparently homogeneous; they lack clearly defined laminae but also show no evidence for bioturbation. In addition to the fossil elements apparent in thin section, graptolites are common on bedding-parallel core surfaces. Pyrite occurs as fine grains dispersed throughout the shales and locally as larger bedding-parallel concretions. Both limestones and shales are locally cut by subvertical to subhorizontal, calcite-healed fractures (Fig. 11). Calcite veins are typically less than 1 mm in thickness.

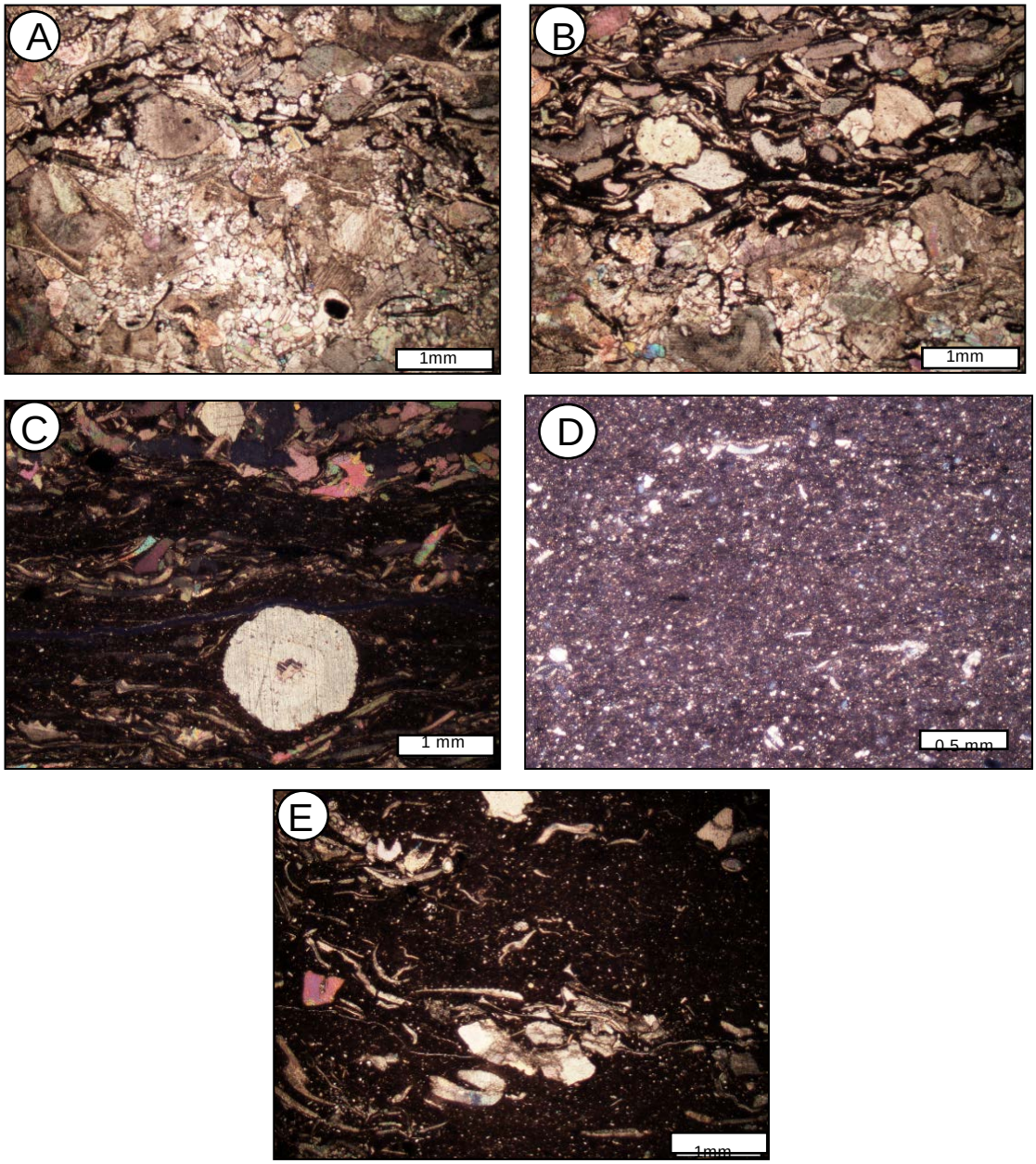

Figure 12. Photomicrographs of limestone (A-C) and shale (D,E) beds in Lithofacies B. (A) Biosparitic limestone grading upward into a packed biomicrite (thin section CC-5). (B) Packed biomicrites grading upward into sparse biomicrite (thin section CC-5). (C) Sparse biomicrite interval (thin section CC-6). (D) Homogeneous shale with dispersed skeletal allochems, carbonate silt grains, and pyrite. (E) Shale interval with irregular stringer of skeletal allochems (thin section CC-5).

5.1.3 Lithofacies C- Carbonaceous Shale with Thin, Fine-Grained Carbonate Beds and Laminae

Lithofacies C is characterized by dark gray, calcareous and carbonaceous shale and light to medium gray limestone (Fig.13). This lithofacies differs from Lithofacies B in several ways. In Lithofacies C, limestones are less abundant, thinner, finer grained, and generally more argillaceous. Limestone comprises only ~15% of this lithofacies and occurs as <1-mm-thick laminae and thin beds in isolation or in closely spaced sets (Fig. 14). Although some beds may be up to 15 cm thick, average limestone thickness is ~ 2 cm. Limestone beds have sharp basal contacts, sharp to diffuse upper contacts, and are texturally homogeneous to weakly graded (Fig. 14). As shown in thin section, limestone laminae and beds are composed solely of unidentifiable, silt-sized, carbonate grains. Recognizable skeletal fragments or other sand-sized allochemical grains are virtually absent (Fig. 15A-C), although some beds contain small (0.5-1.0 cm long) shale rip-up clasts. Comparatively low carbonate contents (range = 59-69%, average = 65%) generally reflect significant amounts of admixed clastic mud.

Shale intervals that dominate in this lithofacies are relatively carbonaceous variably pyritiferous and calcareous; TOC contents range from 0.8 – 1.4% (mean = 1.09%). Pyrite occurs as finely disseminated crystallites and locally as larger bedding-parallel masses. $CaCO_3$ contents range from 20-40% (average= 27%), reflecting differences in abundance of dispersed silt-sized

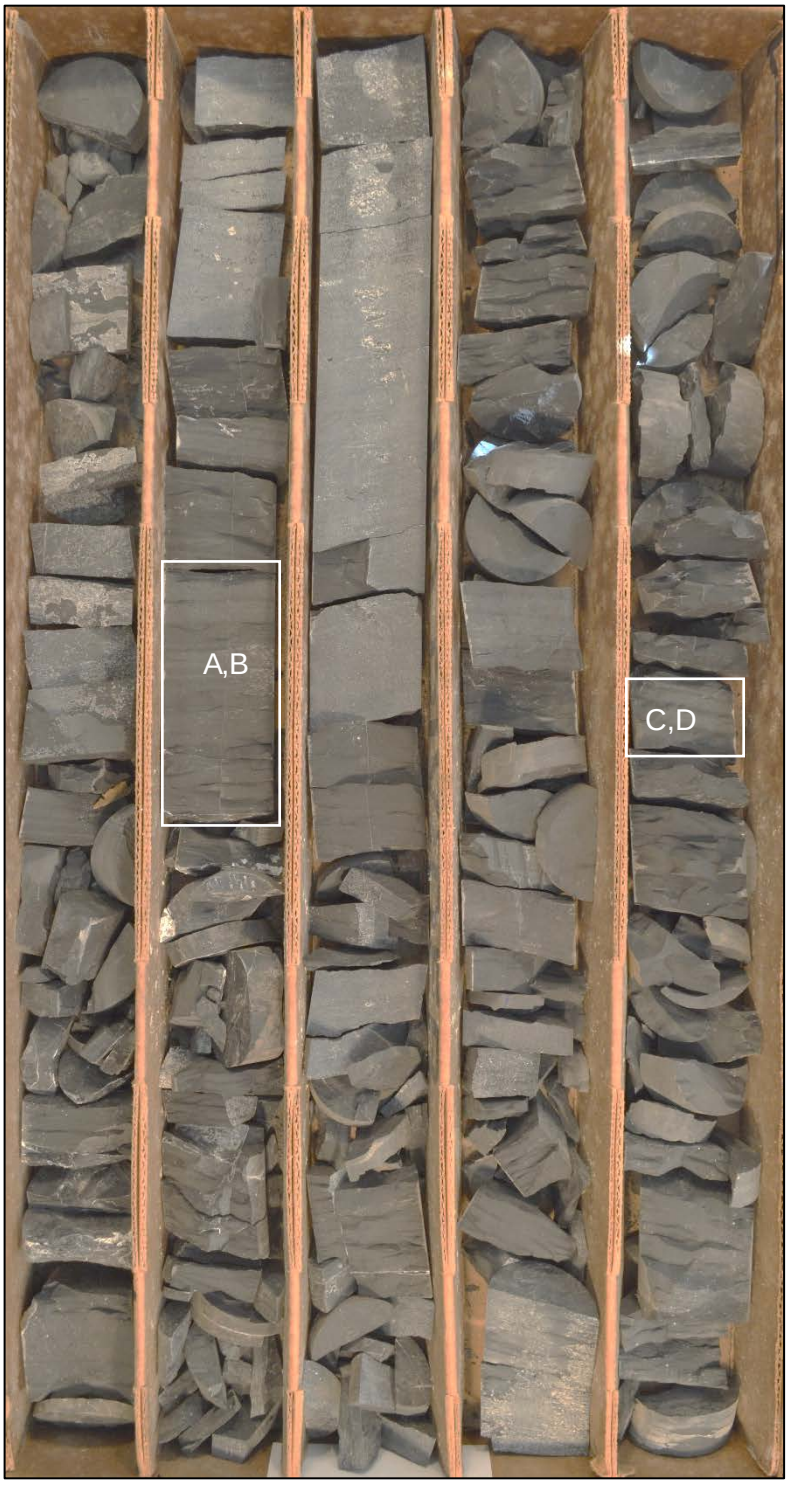

Figure 13. Photograph of core interval 119-129 (Box 9) dominated by Lithofacies C. White boxes indicate intervals shown in detail in Figure 14.

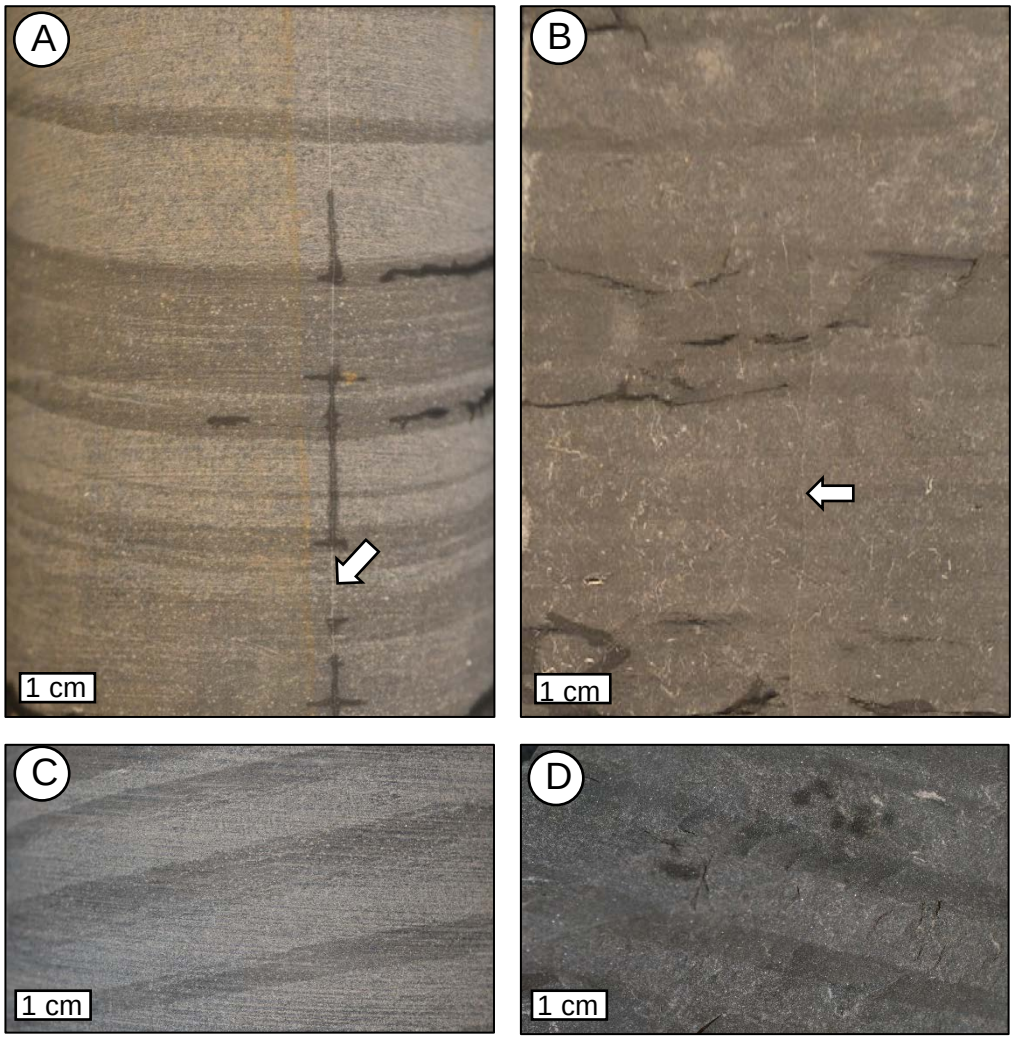

Figure 14. Close up photographs of thin limestone beds and laminae and dark gray shale in Lithofacies C expressed on external (A,C) and internal (B,D) core surfaces. Note sharp bases and gradational tops of beds in C. Small white arrows in A and B indicate narrow calcite-healed fracture.

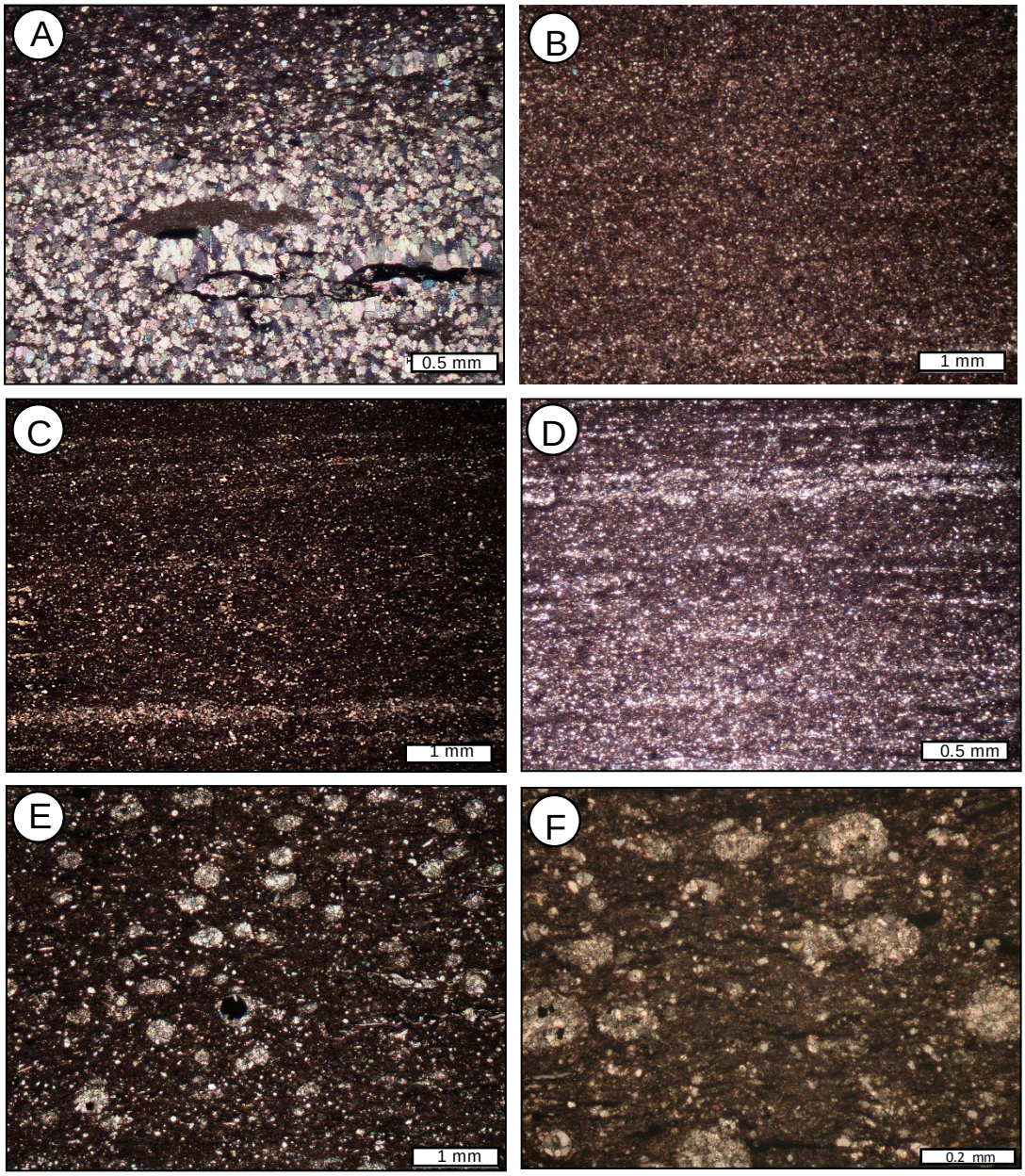

Figure 15. Photomicrographs representing characteristic features of Lithofacies C. (A) Carbonate bed with thin, flattened enigmatic structure with fine-grained mud fill (thin section CC-17). (B) Carbonaceous shale interval (thin section CC-7). (C) Continuous, parallel carbonate laminae sets interbedded with carbonaceous shale (thin section CC-11). (D) Sets of carbonate silt laminae in shale (thin section CC-10). (E) Carbonaceous mud with spherical calcite filled structures (calcispheres?) in a carbonaceous shale interval (thin section CC-22). (F) Closer view of calcite-filled bodies within a carbonaceous shale interval (thin section CC-22).

carbonate grains similar to that observed in the limestone beds (Fig. 15B-D) and of larger (0.2-0.5 mm) spherical to subspherical calcite bodies. The latter structures are characterized by sparry calcite crystals that appear to radiate inward from the margins and, in some cases, envelope euhedral crystals of an opaque mineral, most likely pyrite (Fig. 15E, F). Although no visible wall structure is preserved, the character of these structures suggests they originated as hollow spheres that were mineralized during early diagenesis, prior to significant compaction. These structures may be microfossils, possibly calcispheres (see below). Otherwise, unlike those in Lithofacies B, shales in Lithofacies C are generally devoid of recognizable carbonate skeletal allochems. However, as in Lithofacies B, graptolites are common on bedding-parallel parting surfaces in Lithofacies C shales.

Overall, there is little evidence of significant bioturbation in Lithofacies C. Small (<0.5 mm diameter), lenticular mud masses observed towards the tops of some limestone beds could be construed as compacted burrow fills (Fig. 15A). However, these could instead be shale rip-up clasts. The preservation of mm-scale carbonate silt laminae and apparent lack of disrupted bed contacts (Fig. 14) indicate that Lithofacies C strata are generally unbioturbated.

Rocks in Lithofacies C are also locally cut by calcite-healed fractures (e.g., Fig. 14A, B). These vary from vertical to subhorizontal and are typically less than 1 mm wide.

5.1.4 Lithofacies D – Carbonaceous Shale

Lithofacies D is characterized by dark gray carbonaceous shale with rare, thin, light gray, discontinuous to continuous carbonate laminae (Figs. 16-18). Carbonate laminae, which make up only ~10% by volume of this lithofacies, range in thickness from <1 mm to 5 mm. Like those in Lithofacies C, they typically exhibit relatively sharp bases and gradational tops, lack recognizable allochems, and are composed of unidentifiable silt-sized carbonate grains (Fig. 18A). Owing to the relative paucity of limestone beds and laminae, carbonate contents for Lithofacies D are comparatively low, ranging from 14-47% $CaCO_3$ (average= 25%). The dark gray shales that dominate in Lithofacies D are in several respects similar to those in Lithofacies C. They are comparably organic rich (TOC range = 0.89 to 2.23%, mean = 1.03%), and pyritiferous, contain common graptolites and dispersed fine silt-sized carbonate grains, and include common medium sand-sized (~0.5 mm), spherical to sub-spherical bodies (calcispheres?) filled with sparry calcite and pyrite (Fig. 18B). However, Lithofacies D shales differ in two ways. First, siliciclastic fine silt grains, mainly quartz dispersed in the finer-grained matrix, are more abundant (Fig. 18B, C). Notably, in this lithofacies at higher stratigraphic levels in the core, siliciclastic silt grains become more abundant as the frequency and grain size of distinct carbonate laminae decreases.

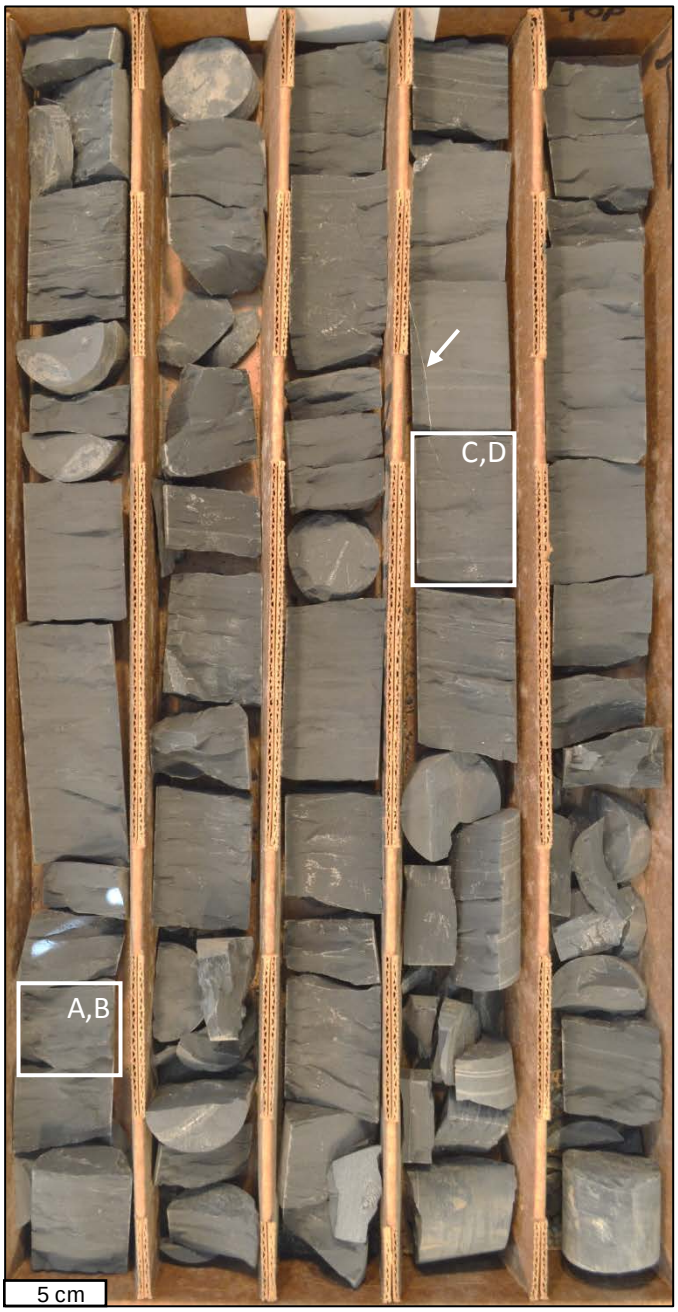

Figure 16. Photograph of core interval 49-59 (Box 2) exemplifying Lithofacies D. White boxes indicate intervals shown in detail in Figure 17. Arrow points to narrow, calcite-healed fracture.

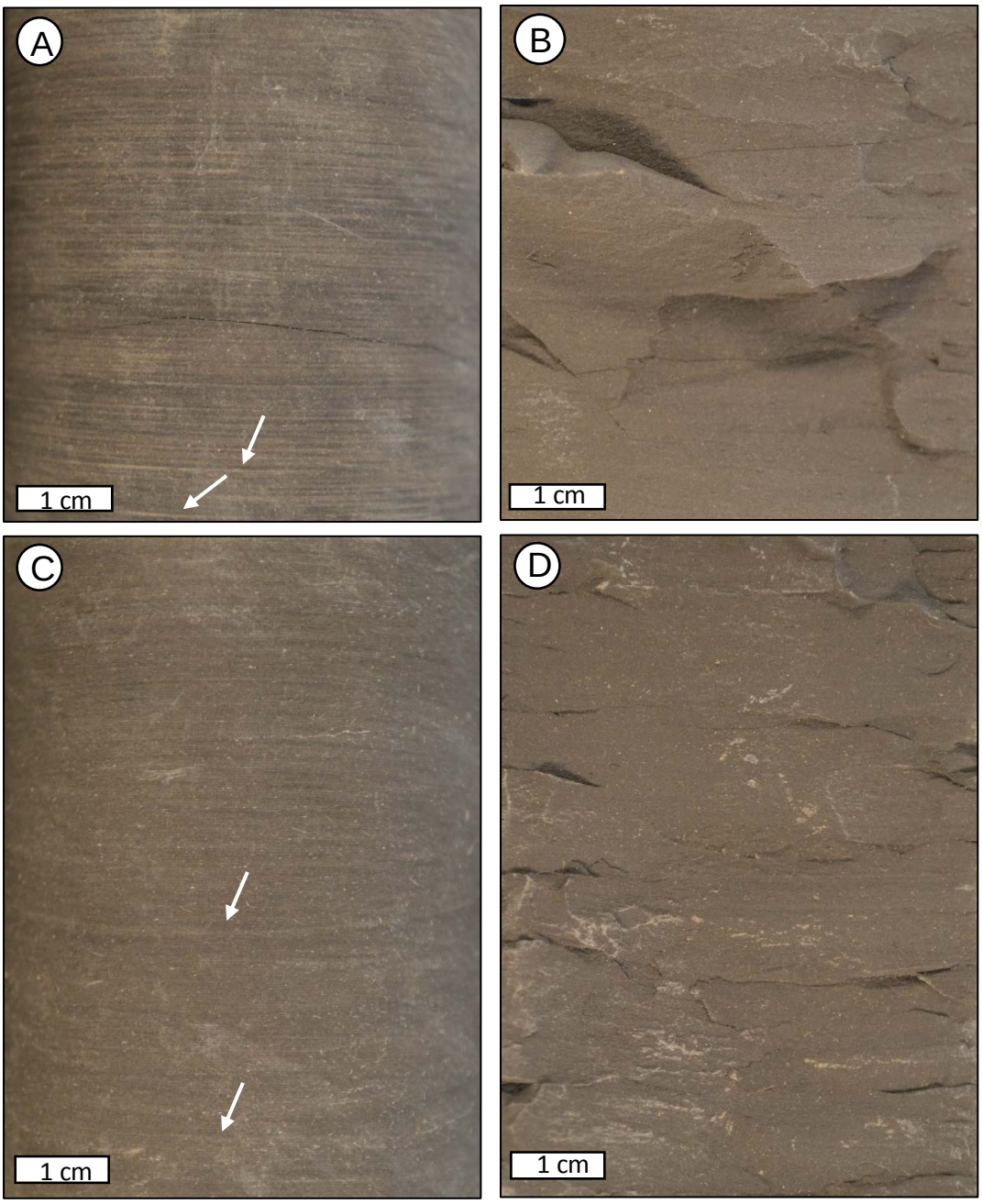

Figure 17. Close up photographs of dark gray shale with thin limestone laminae in Lithofacies D expressed on external (A, C) and internal (B, D) core surfaces. Arrows in B and D highlight a few thin carbonate laminae.

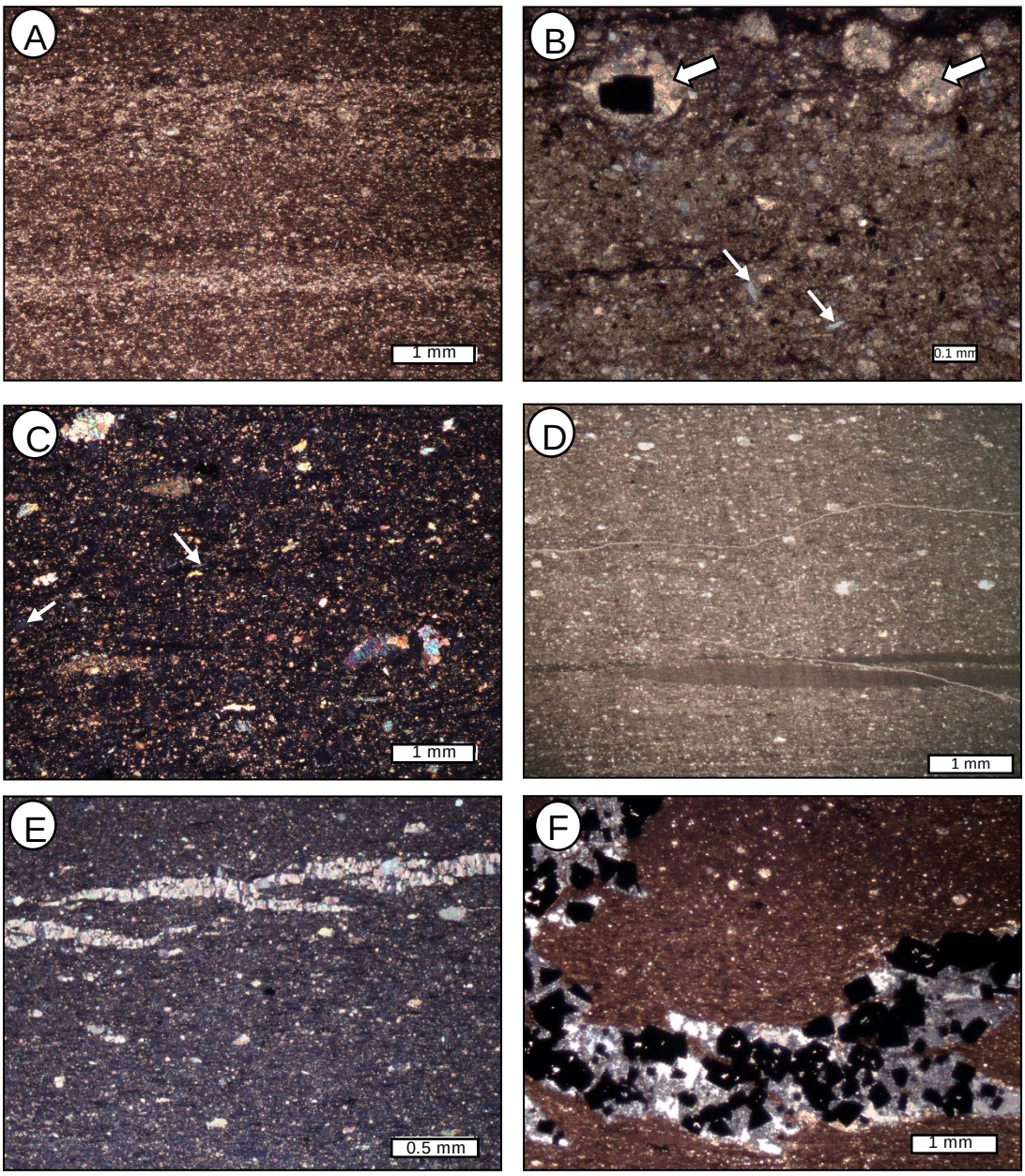

Figure 18. Photomicrographs exemplifying Lithofacies D. (A) Thin, continuous, parallel carbonate laminae interbedded with carbonaceous shale (thin section CC- 32). (B) Shale with dispersed fine quartz silt grains (small arrows) and calcite- and pyrite-filled spherical structures (calcispheres?; large arrows) (thin section CC-32). (C) Shale with dispersed quartz silt grains (arrows) (thin section CC-37) (D) Carbonaceous shale with flattened lenses of fine grained mud perhaps representing compact burrow fills (thin section CC-41). (E) Carbonaceous shale with sub-horizontal, irregular calcite-filled vein (thin section CC-30). (F) Shale with pyrite euhedra surrounded by gypsum (thin section CC-27).

Second, evidence of bioturbation is more prominent in Lithofacies D shales. As revealed in thin section, shales locally contain small (~1 cm wide, 0.2-0.5 mm thick) lenses of finer grained mud (Fig. 18D). These structures, which may represent highly compacted burrow fills, appear to be more common in at higher stratigraphic levels where dispersed siliciclastic silt is more common.

Like other lithofacies, Lithofacies D strata are locally cut by vertical through bedding-parallel, planar to irregular, calcite veins and fracture fills (Figs. 16, 18E, F). Other diagenetic features include localized masses of gypsum surrounding euhedral pyrite crystals (Fig. 18F).

5.2 Vertical Distribution of Lithofacies

The vertical distribution of the four lithofacies through the Calera core section is illustrated in Figure 19, along with carbonate and organic carbon data. As shown, there is a simple succession from Lithofacies A, through Lithofacies B and C, to Lithofacies D within the cored interval. Based on this lithofacies succession, several general trends are apparent. First, frequency, thickness, and overall grain size of carbonate beds decrease up-section as carbonaceous shale becomes more prevalent. Second, the abundances of dispersed calcispheric bodies, fine clastic silt grains, and evidence for at least minor bioturbation appear to increase towards the top of the section.

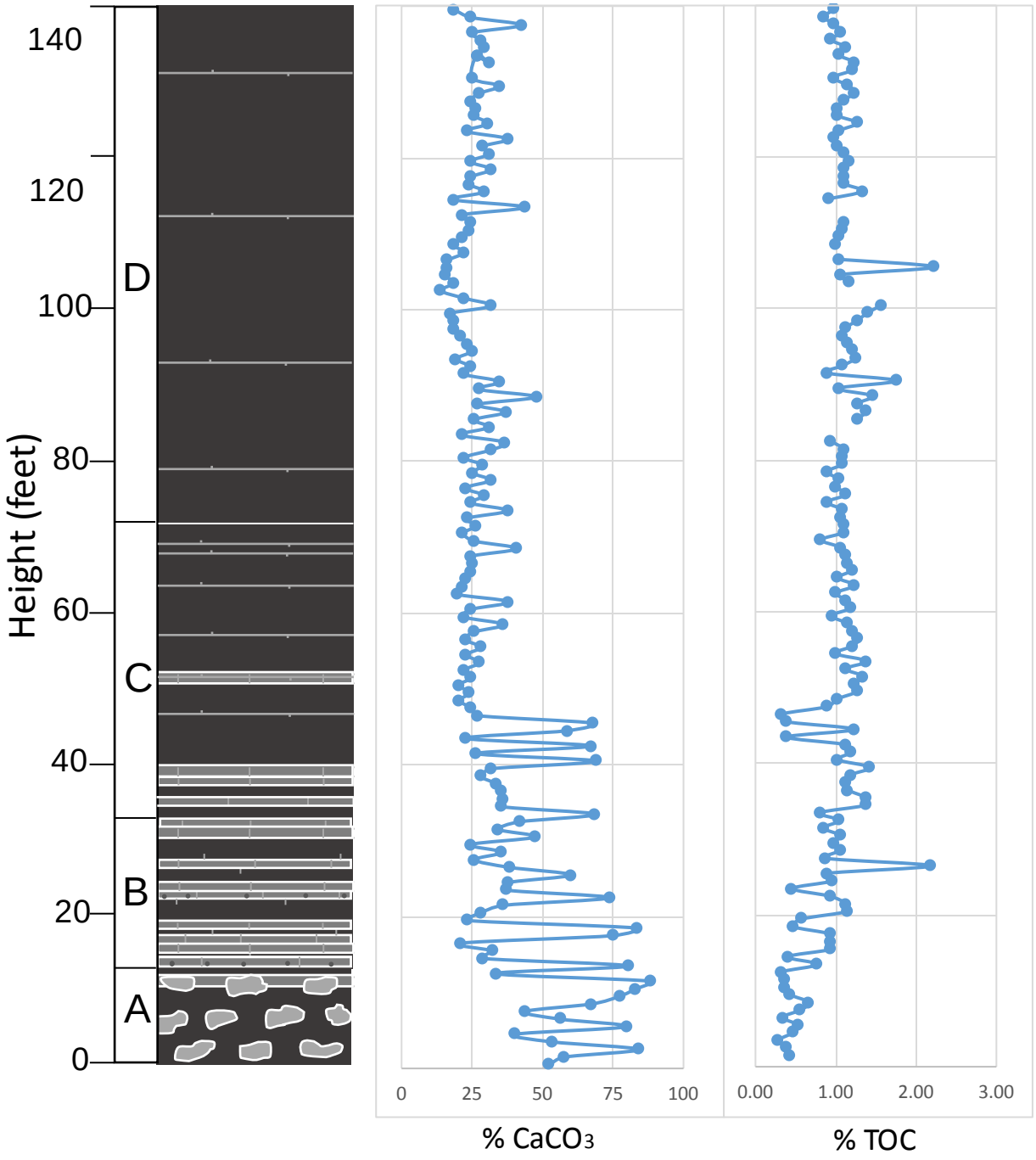

Figure 19. Vertical distribution of lithofacies and carbonate/organic carbon contents of the Athens in the Calera core section.

5.3 Lithofacies Interpretations

Athens Shale lithofacies appear to reflect a variety of depositional processes as expected in a slope-basin setting. These include episodic mass-movement processes, which are mainly manifested by the limestones in lithofacies A, B, and C, and pelagic and hemipelagic processes indicated by carbonaceous shales in lithofacies B, C, and D.

5.3.1 Lithofacies A

Lithofacies A is interpreted to reflect deposition by debris flows, a common transport mechanism in both siliciclastic and carbonate slope settings (Hampton, 1972, 1975; Crevello and Schlager, 1980; McIlreath and James, 1984). The pebble- and cobble-sized limestone nodules in lithofacies A are carbonate clasts that were derived from the adjacent carbonate platform and, supported by cohesive matrices of mud and interstitial water, were transported downslope. With sufficient decrease in gravitational shear stress, the clasts and associated mud matrix were essentially “frozen” in place.

Debris-flows result from unstable slopes. They may form at the downslope ends of slumps and may give rise to turbidity currents (Hampton, 1972; Boggs, 2006). In settings adjacent to carbonate platforms, slope instability may result from changes in base level, overproduction, and/or tectonic subsidence (Tucker and Wright, 2009). In the case of the debrites in lithofacies A of the Athens Shale, carbonate slope failure and transportation of platform debris were most likely triggered by abrupt basin subsidence associated with Taconic orogenesis. Notably, comparable debris-flow deposits have been documented in the lower

parts of other Taconic foreland-basin successions (e.g., in the Whitesburg Formation of Tennessee) and similarly have been attributed to tectonic subsidence (e.g., Shanmugan and Benedict, 1978; Shanmugan, 1980; Shanmugan and Walker, 1983; Ruppel and Walker, 1984).

5.3.2 Limestones of Lithofacies B, C, and D

Limestone beds within lithofacies B, C, and D are interpreted to have been deposited by turbidity currents, which along with debris flows are a common mode of transport in carbonate slope settings (Crevello and Schlager, 1980; McIlreath and James, 1984). The thicker, graded, calcarenitic limestones with sharp, erosional bases in lithofacies B record higher-energy depositional events and thus likely represent proximal turbidites. In contrast, generally thinner, finer-grained limestones prevalent in lithofacies C and D are inferred to be more distal turbidites.

Turbidity-current transport of sediments from the carbonate platform may have been triggered by storms impacting the platform margin or by other mass-movement processes impacting the slope (e.g., slumping, debris flows). The change from common, thicker proximal turbidites to progressively less frequent and thinner distal turbidites through the lithofacies B-lithofacies D transition indicates that slopes became more stable and/or that the supply of carbonate sediment from the platform decreased through time. Reduction in carbonate sediment supply to the slope and basin may be attributed to sea-level rise and progressive deepening over the carbonate platform (McIlreath and James, 1984).

Notably, carbonate turbidites have been recognized in other Taconic foreland-basin strata of Virginia and Tennessee (e.g., Read, 1980; Walker and Benedict, 1980; Shanmugan and Lash, 1980; Walker and Ruppel, 1984). These have been similarly attributed to deposition in slope, ramp, base-of-slope, and basinal settings during drowning of carbonate ramp environments.

5.3.3 Shales in Lithofacies B, C, and D

Calcareous, carbonaceous shales predominate in lithofacies B, C, and D and, thus, in the Athens Shale in general. Despite their abundance, these mudrocks are in several ways difficult to decipher. Questions remain regarding specific depositional mechanisms, sources of sediment, and basin redox conditions.

Some thin shale intervals, particularly but not exclusively those immediately above purported limestone turbidites (e.g., those in lithofacies B), may have been emplaced by turbidity currents or other relatively rapid mass-movement processes. However, most shale intervals are not so intimately associated with limestone event beds. Their homogeneous or faintly laminated fabrics provide little evidence of particular depositional mechanisms. Sedimentation may have occurred as a slow pelagic rain. However, it is likely that, hemipelagic processes (e.g., nepheloid or other plumes) also likely played a role. The shales typically contain admixed carbonate silt. As noted by McIlreath and James (1984), in pre-Mesozoic deposits, such carbonate mud likely had to be derived from adjacent carbonate platforms and thus would be considered a hemipelagic constituent. In contrast, the siliciclastic mud that dominates the

Athens shales likely was derived from noncarbonate sources in the emerging Taconic highlands to the north and east of the basin (see Section 6.4). Greater abundances of dispersed siliciclastic silt grains upward through the section may reflect increased sediment flux from these sources, possibly related to progressive uplift and/or progressive filling of the basin.

The origin of the calcite-filled spherical bodies, referred to above as calcispheres, is unclear. Calcispheres, best known from Mesozoic and Cenozoic strata, typically are manifest in thin section as spherical bodies with thin calcareous walls and are regarded as calcareous cysts produced either by benthic algae or dinoflagellates (e.g., Scholle and Ulmer-Scholle, 2003). Similar features rarely are recognized in Paleozoic strata. For example, Servais et al., (2009) described well-preserved, calcite-walled spherical bodies in Silurian carbonate platform deposits of Sweden and noted their resemblance to dinoflagellate cysts and acritarchs. Because the biological affinities of Paleozoic forms are not well established, Versteegh et al., (2009) proposed that a new term, “calchitarcha,” be applied to these enigmatic calcareous microfossils, in lieu of “calcispheres.” Notably, none of the spherical bodies observed in the Athens Shale exhibit clearly defined walls, making interpretations more tenuous. However, the presence of thin walls may have been masked by diagenesis. If these structures are microfossils (i.e., calcispheres or calchitarcha), their localized occurrences in the Athens Shale may reflect “blooms” of some unknown possibly planktonic, cyst-forming microorganism. However,

interpretations of their origins and potential relations to oceanographic conditions remain problematic.

Most evidence indicates that deposition of the shales occurred primarily under anoxic conditions. Common pyrite clearly indicates sulfidic (anoxic) conditions in the substrate, while the preservation of very thin carbonate event beds (distal turbidites), the general lack of discrete biogenic structures (i.e., burrows), moderately high organic carbon contents, and the lack of body fossils other than well-preserved planktonic forms (i.e., graptolites) suggest that bottom waters also were oxygen depleted. However, the lack of common discrete lamination in the shales and the localized occurrence of purported, compacted burrow fills indicate at least periodic episodes of slightly improved oxygenation. Notably, based on sediment fabrics and lack of body fossil content, anoxic conditions have been inferred for stratigraphically related Ordovician strata in Tennessee (Walker and Ruppel, 1984) and Virginia (Read, 1980) and are consistent with widespread anoxia reported for the Early Paleozoic (Berry and Wilde, 1978). Additional discussion of oxygen conditions during Athens Shale deposition is provided in Chapter 6.

5.4 Comparison to Pratts Ferry and Vincent sections

As noted previously, natural exposures of the Athens Shale are rare and commonly are deeply weathered. Only two outcrop sections of the Athens Shale were deemed worthy of examination in this study: the Pratts Ferry and Vincent sections. These are briefly described and compared with the Calera core section below.

5.4.1 Pratts Ferry Section

The Pratts Ferry outcrop exposes the lower part of the Athens Shale, which here is characterized by interbedded light-to medium-gray limestones and darker gray, calcareous shales (Fig. 20A, B). Limestones are well indurated, whereas the shales are fissile and more difficult to sample. Limestones range from <1 mm to several cm thick, have sharp bases and sharp to gradational tops, and are weakly graded but overall micritic; obvious skeletal or other carbonate allochems are lacking (Fig. 21A-D). These limestones resemble those observed in the Calera section, particularly those in Lithofacies B and C, and likely reflect deposition by turbidity currents (i.e., they are proximal and distal carbonate turbidites) flowing from slopes on the eastern side of the basin. Additional evidence for deposition of this interval along a basin-margin slope occurs in the form of soft sediment deformational features. Convolute laminations or soft-sediment folding locally occur within limestones (Fig. 20B) and, less commonly, in calcareous shales directly beneath limestone beds (Fig. 21C, D).

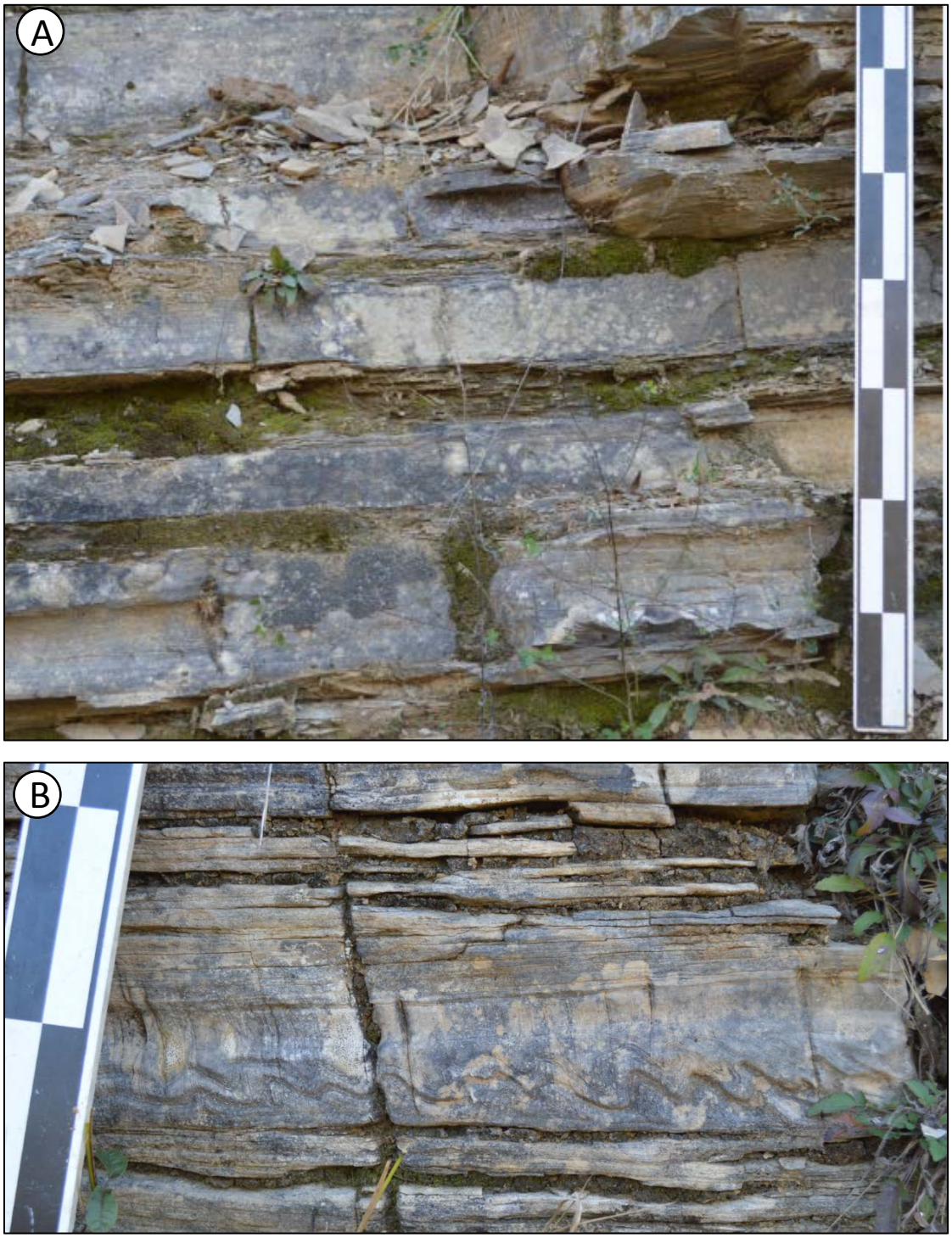

Figure 20. Outcrop photos of the Pratts Ferry section. (A) Interbedded limestones and darker gray, fissile shales. (B) Soft-sediment deformation in lower part of a limestone bed.

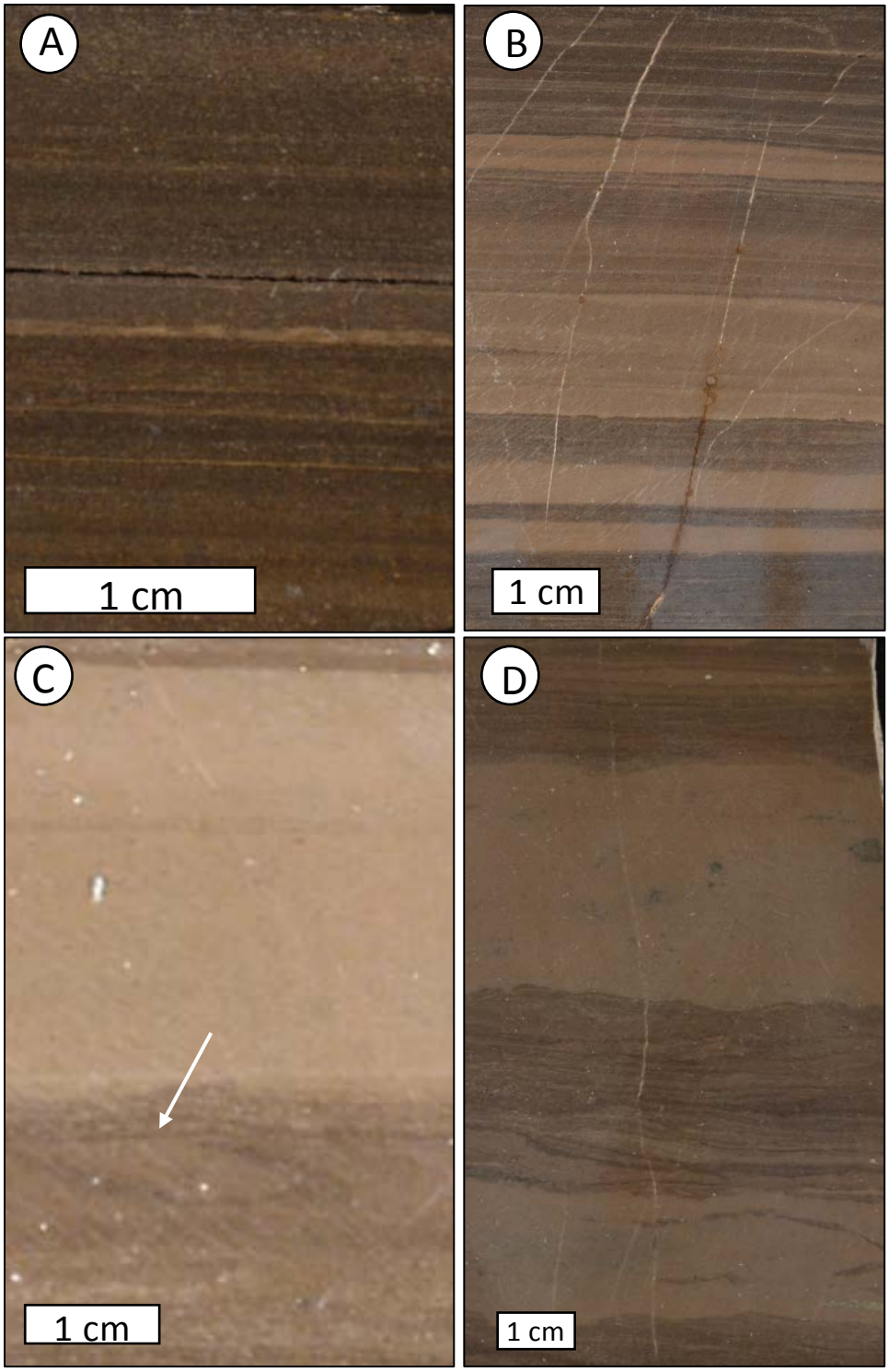

Figure 21. Photographs of slabbed block samples collected at the Pratts Ferry locale. (A) Thin carbonate laminae in calcareous shale. (B) Thin micritic limestone beds interbedded with calcareous shale. (C) Relatively thick micritic limestone bed overlying calcareous shale with soft sediment deformation features (arrow). Cross cutting linear features are saw marks. (D) Interbedded carbonate and calcareous shale with localized small-scale deformational features.

5.4.2 Vincent Sections

Compared to the Pratts Ferry section, the Athens shale at the Vincent locality is highly structurally deformed (Fig. 22A) and more deeply weathered. This section is dominated by platy weathering, calcareous shale or mudstone (Fig. 22B); distinct limestone beds are not readily evident in outcrop. Many of the collected block samples are faintly laminated to homogeneous mudrocks with locally common, large pyrite nodules (Fig. 23A, B). Other samples reveal the presence of thinly interbedded or interlaminated limestone and calcareous shale (Fig. 23C, D). Faint grading in the thin limestone beds and laminae resembles that observed in limestone layers in Lithofacies C in the Calera section. These intervals similarly may be interpreted as distal carbonate turbidites.

Figure 22. Outcrop photos of the Vincent section. (A) Weathered platy shale in tight, nearly isoclinal fold. (B) Highly fractured, platy carbonaceous shale.

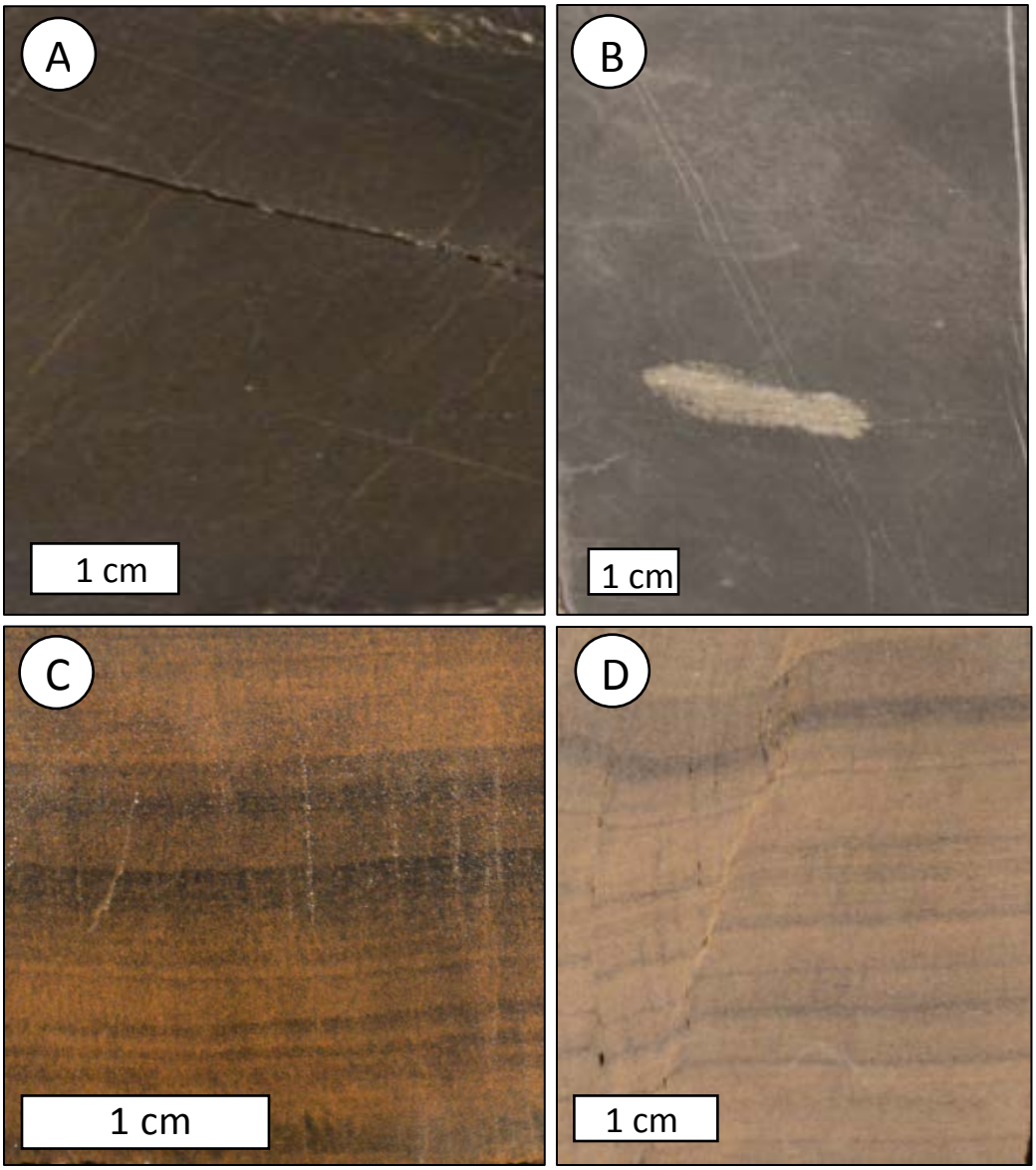

Figure 23. Photographs of polished block samples collected at Vincent section. (A) Apparently homogeneous carbonaceous, calcareous shale. (B) Calcareous shale with large pyrite concretion. (C) Thinly laminated limestone and calcareous shale cut by small-scale microfaults. (D) Thinly laminated limestone and calcareous shale.

6. Athens Shale Geochemistry

6.1 Introduction

The results of geochemical analysis of Athens Shale samples from the Calera section are presented in Tables 4 and 5. In the following sections, selected components of this dataset are used to: (1) compare Athens Shale geochemistry with other black shales and mudrocks in general; (2) assess paleo-redox conditions in the Athens basin; and (3) evaluate mudrock provenance.

6.2 Trace Element Geochemistry

Mudrocks may contain minor and trace elements in concentrations that may be more than a hundred times that of average crustal abundances, and some mudrocks, particularly black shales, may be so metal enriched that they serve as potential economic resources. Enrichment in uranium and other metals is generally linked to the elevated organic carbon contents of these rocks (Leventhal and Hosterman, 1982). As an example, parts of the Devonian Chattanooga Shale of the Appalachian Basin have uranium contents as high as 90 ppm (Conant and Swanson, 1961; Leventhal and Kepferle, 1982; Frost et al., 1985).

The trace element concentrations of the Athens Shale samples are compared with those of the average shale (from Turekian and Wedepohl, 1961)

Table 4. Trace element compositions of Athens Shale samples.

Sample		TOT/C	TOT/S	Mo	Cu	Pb	Zn	Ag	Ni	Co	Mn	Fe	As	U
	Unit	%	%	ppm	ppm	ppm	ppm	ppm	ppm	ppm	ppm	%	ppm	ppm
1-3-16-17		4.17	1.35	10.3	37.9	21.3	80	<0.5	46.3	11.5	254	2.49	13	1.7
2-5-7		3.78	1.22	10.3	39.2	21.1	92	<0.5	46.9	11.5	194	2.27	14	1.7
3-3-7		3.04	1.28	12.9	44.5	23.4	83	<0.5	52.3	12.1	166	2.28	14	1.7
4-5-20		3.00	1.30	12.3	43.1	24.8	99	<0.5	50.9	12.3	182	2.46	11	1.9
5-3-17		3.20	1.29	11.0	44.0	23.0	109	<0.5	50.4	12.3	179	2.36	12	1.8
6-2-9.5-10.5		3.44	1.48	12.0	38.7	20.3	85	<0.5	44.9	11.0	186	2.31	12	1.8
7-2-4.5-5.5		3.41	1.24	12.5	46.9	22.7	144	<0.5	52.7	12.6	188	2.34	13	2.5
8-3-15-16		2.68	2.19	15.2	53.1	29.9	132	<0.5	68.7	14.5	165	3.10	18	2.9
9-5-20-21		3.18	1.76	13.8	55.0	27.1	119	<0.5	66.4	14.3	180	2.85	16	3.2
10-4-20-21		4.20	1.29	12.6	45.8	22.3	130	<0.5	53.1	11.6	203	2.34	14	6.2
13-5-7-8		8.67	1.15											
14-2-5		8.95	0.30											

Sample		Th	Sr	Cd	Sb	Bi	V	Ca	P	La	Cr	Mg	Ba	Ti
	Unit	ppm	ppm	ppm	ppm	ppm	ppm	%	%	ppm	ppm	%	ppm	%
1-3-16-17		4.0	162	0.5	1.2	<0.5	20	9.02	0.034	9.7	14.9	1.30	80	0.006
2-5-7		4.2	152	<0.5	0.9	<0.5	29	8.30	0.035	9.4	13.2	1.09	211	0.006
3-3-7		4.9	122	<0.5	1.0	<0.5	23	5.96	0.032	9.5	13.2	0.92	86	0.006
4-5-20		5.0	110	<0.5	0.9	<0.5	24	5.78	0.031	10.2	14.7	1.15	84	0.007
5-3-17		4.5	135	0.6	1.0	<0.5	25	6.88	0.033	9.2	13.3	0.94	159	0.006
6-2-9.5-10.5		4.1	140	0.5	0.9	<0.5	20	7.10	0.035	9.1	12.7	0.90	89	0.006
7-2-4.5-5.5		4.9	141	1.1	1.3	<0.5	39	7.00	0.040	10.4	14.7	1.08	79	0.006
8-3-15-16		5.2	108	0.8	1.5	<0.5	28	4.95	0.050	9.7	15.5	0.87	75	0.006
9-5-20-21		5.1	132	0.9	1.6	<0.5	31	5.95	0.056	10.8	16.3	1.01	78	0.006
10-4-20-21		4.7	183	1.5	1.5	<0.5	36	8.82	0.049	9.8	14.0	1.50	91	0.005

Table 4 continued. Trace element compositions of Athens Shale samples.

Sample		***Hg***	***Sc***	***Tl***	***S***	***Ga***	***Se***	***Al***	***Na***	***K***	***W***
	Unit	ppm	ppm	ppm	%	ppm	ppm	%	%	%	ppm
1-3-16-17		0.09	5.2	1.0	1.34	<5	<2	0.94	0.01	0.31	<0.5
2-5-7		0.08	5.4	1.1	1.21	<5	<2	0.91	<0.01	0.28	<0.5
3-3-7		0.13	5.2	1.2	1.23	<5	<2	0.99	<0.01	0.32	<0.5
4-5-20		0.12	6.3	1.2	1.30	<5	<2	1.00	<0.01	0.33	<0.5
5-3-17		0.08	6.1	1.3	1.29	<5	<2	0.95	<0.01	0.30	<0.5
6-2-9.5-10.5		0.10	5.2	1.2	1.38	<5	<2	0.88	<0.01	0.28	<0.5
7-2-4.5-5.5		<0.05	6.0	1.3	1.24	<5	<2	1.02	0.01	0.32	<0.5
8-3-15-16		0.12	5.0	1.7	2.09	<5	<2	1.05	<0.01	0.32	<0.5
9-5-20-21		0.08	5.2	1.6	1.73	<5	2	1.09	0.01	0.32	<0.5
10-4-20-21		0.06	5.6	1.1	1.28	<5	<2	0.94	0.01	0.30	<0.5

Table 5. Whole-rock geochemistry data derived from analyses of Athens Shale samples.

Sample	*SiO_2 (%)*	*Al_2O_3 (%)*	*Fe_2O_3 (%)*	*MgO (%)*	*CaO (%)*	*Na_2O (%)*	*K_2O (%)*	*TiO_2 (%)*	*P_2O_5 (%)*	*MnO (%)*	*Cr_2O_3 (%)*
1-3-16-17	47.44	10.99	4.26	3.17	13.64	0.39	2.91	0.48	0.07	0.03	0.008
2-5-7	50.77	11.13	3.91	2.83	12.36	0.41	2.90	0.49	0.08	0.02	0.007
3-3-7	56.32	11.59	3.96	2.60	8.83	0.39	3.09	0.51	0.08	0.02	0.008
4-5-20	56.38	11.62	4.21	2.97	8.47	0.41	3.09	0.51	0.08	0.02	0.008
5-3-17	54.55	11.58	4.12	2.66	10.25	0.47	3.09	0.51	0.08	0.02	0.008
6-2-9.5-10.5	53.97	10.73	4.12	2.60	11.29	0.42	2.84	0.47	0.08	0.03	0.007
7-2-4.5-5.5	53.93	11.26	3.99	2.83	10.43	0.42	3.00	0.49	0.10	0.02	0.008
8-3-15-16	56.38	12.56	5.24	2.63	7.33	0.47	3.34	0.54	0.13	0.02	0.009
9-5-20-21	53.42	12.61	4.79	2.83	8.91	0.44	3.40	0.54	0.13	0.02	0.009
10-4-20-21	47.08	11.37	4.01	3.61	13.24	0.52	3.17	0.49	0.11	0.03	0.008
13-5-7-8	20.20	5.35	2.50	2.33	36.24	0.21	1.49	0.24	0.24	0.03	0.004
14-2-5	18.07	5.12	1.69	3.65	36.28	0.18	1.48	0.23	0.18	0.08	0.003

Table 5 continued. Whole-rock geochemistry data derived from analyses of Athens Shale samples.

Sample	*Ba (ppm)*	*Ni (ppm)*	*Sr (ppm)*	*Zr (ppm)*	*Y (ppm)*	*Nb (ppm)*	*Sc (ppm)*
1-3-16-17	449	42	173	100	21	15	10
2-5-7	600	42	167	98	22	11	11
3-3-7	495	49	137	93	20	17	11
4-5-20	489	47	124	99	22	12	11
5-3-17	582	49	150	99	21	13	11
6-2-9.5-10.5	485	44	160	88	20	12	10
7-2-4.5-5.5	474	53	151	99	23	13	11
8-3-15-16	508	69	127	101	24	12	12
9-5-20-21	513	65	145	102	25	12	12
10-4-20-21	474	53	187	117	24	10	11
13-5-7-8	281	<20	370	50	25	7	6
14-2-5	236	<20	298	55	16	<5	5

and the average black shale (from Vine and Tourtelot, 1970) in Table 6. For most elements, concentrations in the Athens Shale are equivalent to (Co, Mo, Ni, and Pb) or lower than (Ti, Ba, Cr, Cu, La, Sc, Sr, V, Y, Zn, and U) those of the average black shale. Concentrations of Mn and Zr are only slightly higher than those of the average black shale, and Mn is the only element that can be considered enriched, albeit only slightly. Overall the results indicate that mudrocks of the Athens Shale are not enriched. Indeed, uranium concentrations in the Athens Shale samples, which range from 1.7-6.2 ppm (Table 4), are more than an order of magnitude lower than those in the aforementioned Chattanooga Shale.

Table 6. Trace element concentrations (%) in Athens Shale compared to the average shale and average black shale.

Analyte	*Athens Shale (%)*	*Average Black Shale (%)* *(Vine and Tourtelot, 1970)*	*Shale Average (%)* *(Turekian and Wedepohl, 1961)*	*Minimum enrichment value*
Ti	.006	0.2	.46	0.7
Mn	.19	.15	.085	.1
Ba	.01	.03	.058	.1
Co	.001	.001	.0019	.003
Cr	.001	.01	.009	.07
Cu	.004	.007	.005	.02
La	.002	.003	.009	.007
Mo	.001	.001	.0003	.02
Ni	.005	.005	.007	.03
Pb	.002	.002	.002	.01
Sc	.0005	.001	.0013	.0002
Sr	.013	.02	.03	.15
V	.002	.015	.013	.1
Y	.002	.003	.0026	.007
Zn	.01	.03	.0095	.15
Zr	.009	.007	.016	.02
U	.0002	.002	-	.003

6.3 Potential Redox Indicators

As previously noted, basin oxygenation is a major control on the amount and type organic matter preserved in sediments. Aspects of mudrock geochemistry, particularly elemental ratios, have been employed in previous studies in attempt to evaluate the degree of oxygenation or paleo-redox conditions of depositional basins. Geochemical proxies for redox conditions explored herein include V/Cr, Ni/Co, U/Th, and C/S ratios. These ratios for the Athens Shale are provided in Table 7 and plotted versus stratigraphic height in the Calera section in Figure 24.

6.3.1 V/Cr ratios

Vanadium/Chromium (V/Cr) ratios have been used as an index of paleo-oxygenation in a number of previous studies (Rimmer, 2004; Kuscu et al., 2016). Cr is incorporated within the detrital clastic fraction where it may be substituted for Al within clays, or it occurs as chromite. Vanadium, in contrast, is bound to organic matter, and is concentrated in sediments deposited under reducing conditions. V/Cr ratios above and below 2 are thought to represent anoxic and oxic depositional conditions, respectively (Jones and Manning, 1994).

In the Athens Shale, V/Cr ratios range from 1.34 to 2.65 (average= 1.93; Table 7). Notably, two of the three samples with V/Cr ratios in excess of 2 (i.e., indicating anoxic conditions) fall in the lower part of the shale-dominated interval of the Calera core (Lithofacies C; Fig. 24).

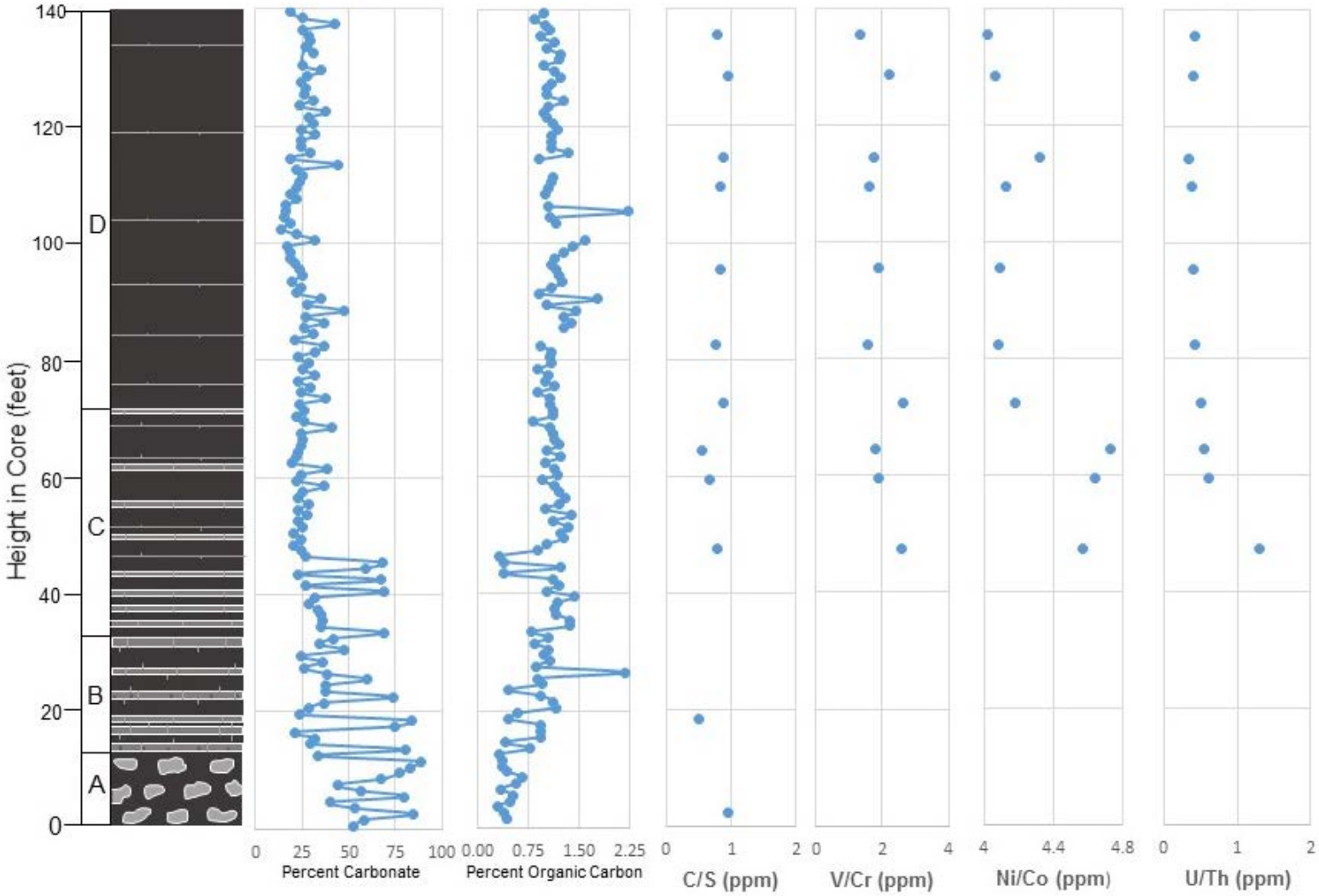

Figure 24. Geochemical indices plotted next to carbonate/organic carbon curves and stratigraphic column.

Table 7. Geochemical indices used to answer paleo-oxygenation conditions.

Sample	*C/S(%)*	*V/Cr(ppm)*	*Ni/Co(ppm)*	*U/Th(ppm)*
1-3-16	0.79	1.34	4.02	0.42
2-5-7	0.94	2.20	4.07	0.40
3-3-7	0.88	1.74	4.32	0.34
4-5-20	0.83	1.63	4.13	0.38
5-3-17	0.83	1.88	4.09	0.4
6-2-9.5-10.5	0.75	1.57	4.08	0.43
7-2-4.5-5.5	0.87	2.65	4.18	0.51
8-3-15-16	0.54	1.81	4.73	0.55
9-5-20-21	0.67	1.90	4.64	0.62
10-4-20-21	0.78	2.57	4.57	1.31

6.3.2 Ni/Co ratios

Jones and Manning (1994) indicate that Ni and Co in sediments are generally associated with pyrite and proposed that Ni/Co ratios may reflect redox conditions. In their scheme, Ni/Co ratios of <5, between 5 and 7, and >7 indicate oxic, sub-oxic, and anoxic-suboxic conditions, respectively. Ni/Co ratios for Athens Shale samples range from 4.02-4.73 (average = 4.67; Table 7), which would suggest oxic conditions in the scheme of Jones and Manning (1994). Notably, however, the highest Ni/Co ratios are recorded for samples in the lower shale-dominated part of the Calera section (Fig. 20).

6.3.3 U/Th ratios

Uranium/thorium (U/Th) ratios also may be used as redox indicators (Jones and Manning, 1994). Thorium in mudrocks is usually found in the detrital fraction of heavy minerals or clays. Some uranium also is found in this fraction but may be lost to solution during weathering. Tyson and Pearson (1991) proposed that U/Th ratios

< 0.75, between 0.75 and 1.25, and >1.25 reflect oxic, dysoxic, and anoxic conditions, respectively.

In the Athens Shale samples, U/Th ratios range from 0.34 to 1.31 (average= 0.54; Table 7). Only one sample has a U/Th ratio that is suggestive of anoxic conditions and that sample occurs in Lithofacies C in the lower part of the Calera section (Fig. 24).

6.3.4 C/S relationship

Carbon/sulfur (C/S) ratios have been employed as a tool to determine depositional environments of mudrocks (e.g., Berner, 1982; Berner and Raiswell, 1983; Leventhal, 1987; Raiswell and Canfield, 2012). When plotted on a bivariate plot (e.g., Fig. 25), C/S ratios may help distinguish shales deposited in marine vs. freshwater settings and to evaluate the degree of oxygenation of marine waters. Mudrocks deposited in freshwater settings, wherein waters are limited in sulfate, are characterized by low S contents. In contrast, for normal marine shales, there is a positive correlation between organic carbon and sulfur; typically, normal marine mudrocks have C/S ratios close to 2.8 (Berner, 1982; see Fig. 25). However, in marine mudrocks deposited in euxinic settings (i.e., below an anoxic water column), C/S ratios tend to be considerably lower (Fig. 25). In the Athens Shale samples, C/S ratios samples are in all cases <1 (average= 0.76; Table 7, Fig. 24) and thus plot in the euxinic field (Fig. 25).

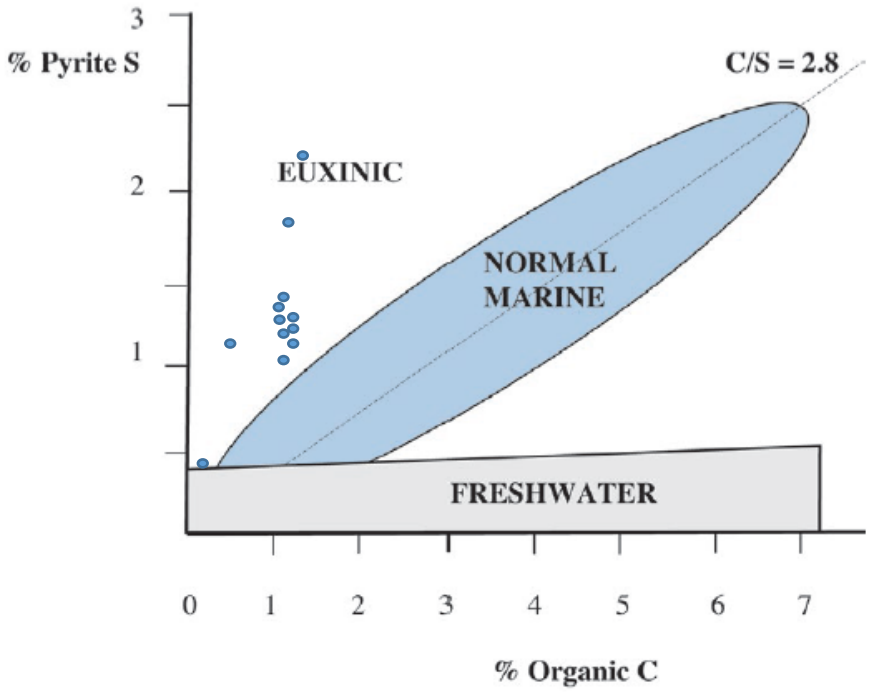

Figure 25. C/S ratios for Athens Shale samples plotted on the diagram of Raiswell and Canfield, (2012).

6.3.5 Implications for Athens Shale Basin Oxygenation

The various geochemical proxies for redox conditions yield mixed results. Ni/Co ratios suggest oxic conditions for all samples. However, V/Cr and U/Th ratios indicate locally lower levels of oxygenation (anoxia), particularly for the lower parts of the Athens Shale in the Calera core section. Increasing oxygenation through time is consistent with the observation of apparent increased weak bioturbation seen upward through Lithofacies D.

C/S ratios, in contrast, suggest that the Athens Basin was persistently euxinic; i.e., it was deposited beneath a highly stratified, anoxic water column. The reasons for this disparity are not fully understood. Berner and Raiswell (1983) noted that C/S ratios of Cambrian and Ordovician marine shales in their study were also low, ranging between 0.4 and 1. They indicated that associated depocenters could have been euxinic but also suggested that low values could be related to the absence of land plants and, thus, a lower "worldwide average C/S burial ratio" in pre-Silurian time. In the case of the Athens Shale, the C/S ratios also may have been influenced by late diagenetic influx of hydrothermal sulfur and/or thermal alteration of organic matter (see Chapter 7) during burial.

6.4 Sediment Provenance

Previous workers have suggested that the geochemistry of mudrocks can be used to evaluate sedimentary provenance, or the types of rocks weathering and eroding in the source area at the time of deposition (Roser and Korsch, 1986, 1988; Hayashi et al., 1997). Provenance, in turn, may reflect tectonic setting of the source area. Here, the more broadly applicable approaches of Roser and Korsch (1986, 1988) are tested using geochemical data derived for the Athens Shale.

Roser and Korsch (1986) proposed the use of a bivariate plot of K_2O/Na_2O vs. SiO2 to help discriminate whether muds were derived from passive margin (PM), active continental margin (ACM), or oceanic island arc (ARC) tectonic settings. When plotted on this diagram (Fig. 26), the majority of Athens Shale samples fall in the passive margin field, while two samples fall at or just inside the boundary of the active continental margin field.

Roser and Korsch (1988) subsequently developed a more rigorous approach that applied geochemical data in discriminate function analysis. Using concentrations of major elements (TiO_2, Al_2O_3, Fe_2O_3, MgO, CaO, Na_2O) and two discriminant function diagrams, they identified four provenance groups or sediment sources for mudrocks: (1) P1- mafic detritus; (2) P2- intermediate, dominantly andesite detritus; (3) P3- felsic plutonic and volcanic detritus; and (4) P4- recycled-mature polycyclic quartzose detritus derived from sandstones and mudrocks. In the first of Rosher and Korsch's (1988) diagrams, which employs

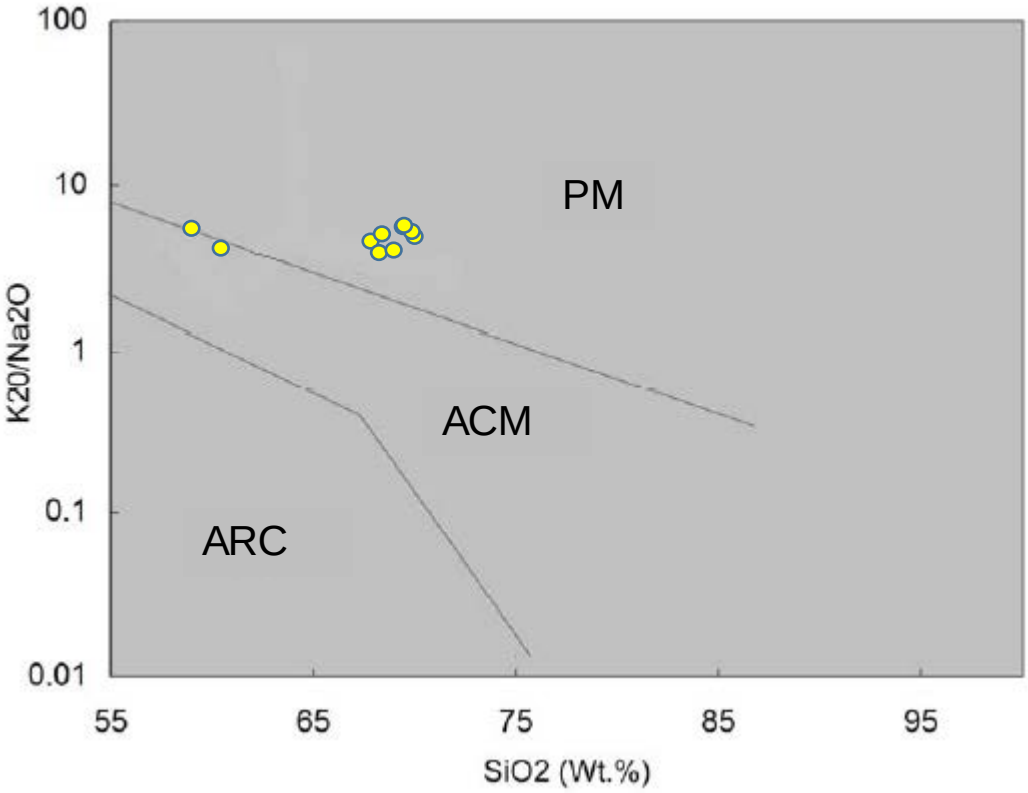

Figure 26. Athens Shale samples plotted on the mudrock provenance diagram of Roser and Korsch (1986). PM = passive margin, ACM = active continental margin, and ARC = oceanic island arc.

unstandardized discriminant coefficients derived from oxide concentrations, Athens Shale samples mainly fall in the P3- felsic plutonic and volcanic detritus field (Fig. 27). However, Rosher and Korsch (1988) noted that provenance discrimination is impacted for mudrocks with high biogenic components (carbonate and biogenic silica), which would include the carbonate-rich Athens Shale. To circumvent this problem, they derived a second diagram that employs unstandardized discriminant function coefficients that are based on oxide/Al_2O_3 ratios. When plotted on this diagram, Athens Shale samples fall well within the P4- quartzose sedimentary provenance field (Fig. 28). Notably, when Athens Shale geochemical data are normalized to exclude CaO (Table 8) and replotted on the first diagram, they also all fall within this same P4 field (Fig. 27).

Taken together, the results described above suggest that sediments making up the Athens Shale mudrocks were derived from the weathering and erosion of quartz-rich sedimentary rocks on a passive margin. This seems counterintuitive considering that Athens' muds likely were derived from the evolving Taconic orogen to the east or northeast. The Taconic orogeny is thought to involve an island arc and arc-continent collision (Niocaill et al., 1991; Hatcher 2010) and, hence, an arc/igneous provenance might be expected. The reasons for the apparent discrepancy are unclear. Athens Shale muds may have been derived mainly from older Paleozoic, Laurentian margin sedimentary rocks that were uplifted in areas between the Athens basin and the volcanic arc. Alternatively, the discrepancy may reflect inadequacies in current models that attempt to link mudrock geochemistry to provenance.

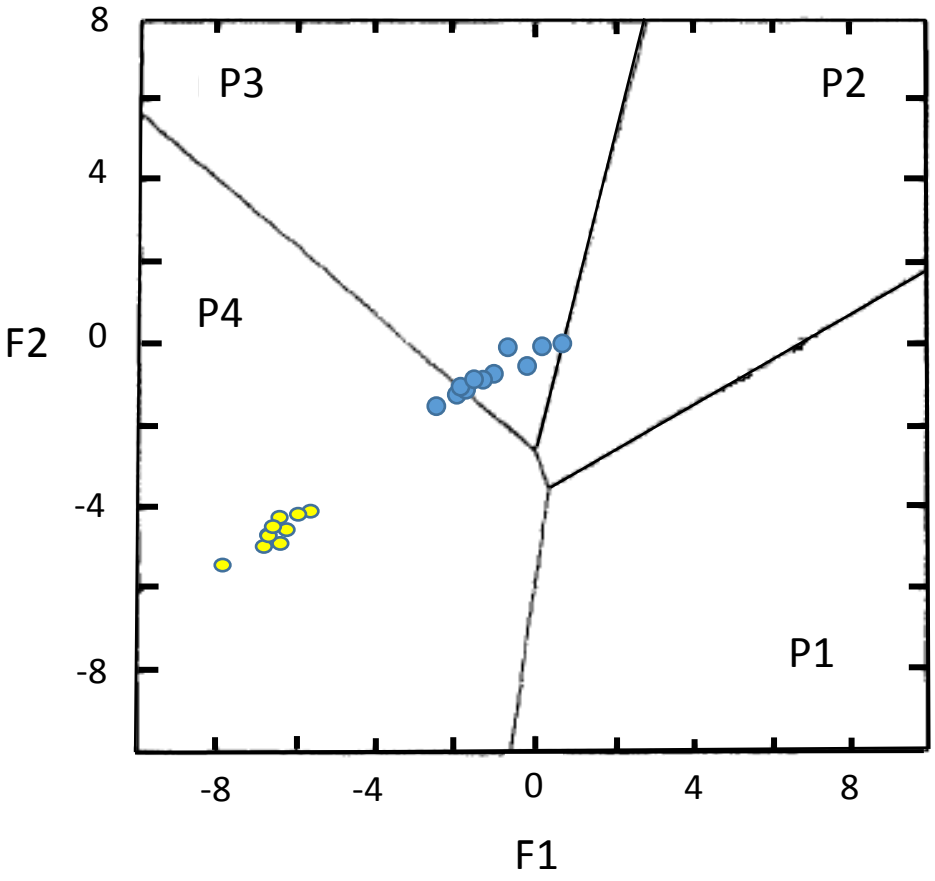

Figure 27. Athens Shale samples plotted on Rosher and Korsch's (1988) discriminant function diagram using coefficients derived from oxide concentrations. Blue dots reflect plots of raw geochemical data. Yellow dots reflect plots of data normalized after exclusion of CaO. P1= mafic detritus, P2+ intermediate dominantly andesitic detritus; P3 = felsic plutonic and volcanic detritus, and P4 = recycled mature polycyclic quartzose detritus.

Discriminant function I = -1.773 TiO_2 + 0.607 Al_2O_3 + 0.76 $Fe_2O_{3(TOTAL)}$ – 1.5 MgO + 0.616 CaO + 0.509 Na_2O – 1.224 K_2O – 9.09;

Discriminant function II = 0.445 TiO_2 + 0.07 Al_2O_3 – 0.25 $Fe_2O_{3(TOTAL)}$ – 1.142 MgO + 0.438 CaO + 1.475 Na_2O + 1.426 K_2O – 6.861

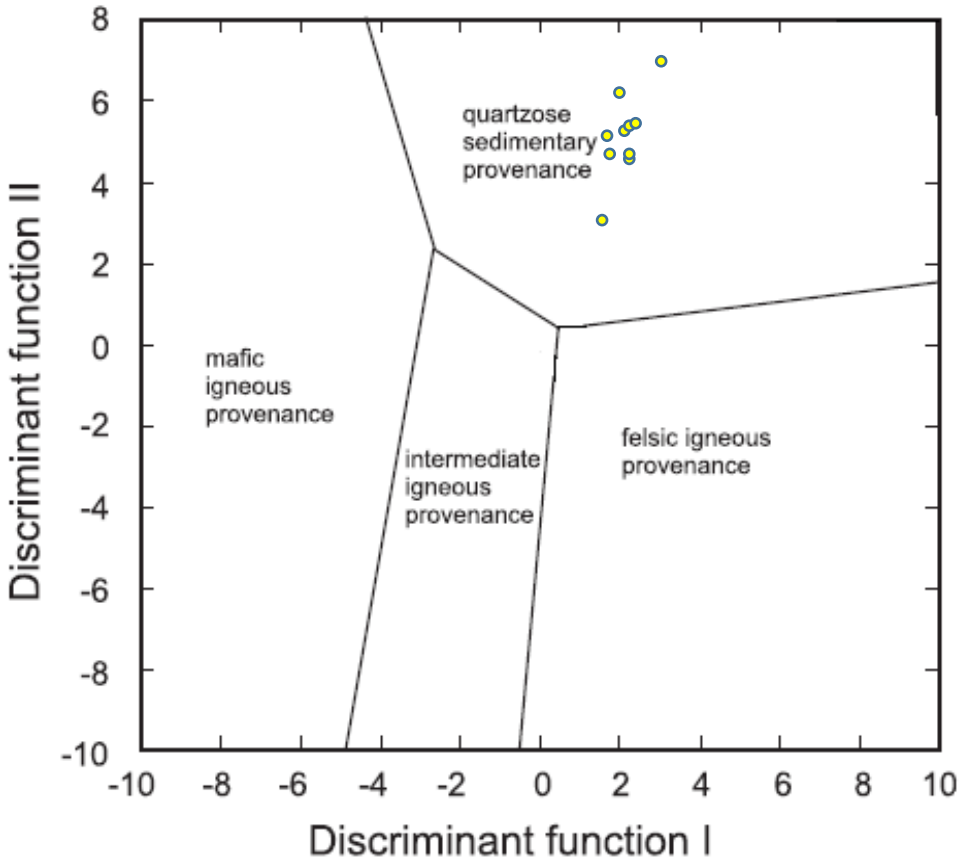

Figure 28. Athens Shale samples plotted on Rosher and Korsch's (1988) discriminant function diagram using coefficients derived from oxide ratios.

Discriminant function I = 30.638 TiO_2 / Al_2O_3 – 12.541 $Fe_2O_{3(TOTAL)}$ / Al_2O_3 + 7.329 MgO / Al_2O_3 + 12.031 Na_2O / Al_2O_3 + 35.402 K_2O / Al_2O_3 – 6.382;

Discriminant function II = 56.500 TiO_2 / Al_2O_3 – 10.879 $Fe_2O_{3(TOTAL)}$ / Al_2O_3 + 30.875 MgO / Al_2O_3 – 5.404 Na_2O / Al_2O_3+ 11.112 K_2O / Al_2O_3 – 3.890

Table 8. Normalized major oxide values used for discriminant function.

Sample	*Al_2O_3 (%)*	*Fe_2O_3 (%)*	*MgO (%)*	*Na_2O (%)*	*K_2O (%)*	*TiO_2 (%)*
1-3-16-17	15.75	6.10	4.54	0.55	4.17	0.68
2-5-7	15.34	5.38	3.90	0.56	3.99	0.67
3-3-7	14.75	5.04	3.30	0.49	3.93	0.64
4-5-20	14.65	5.30	3.74	0.51	3.89	0.64
5-3-17	15.02	5.34	3.45	0.60	4.00	0.66
6-2-9.5-10.5	14.25	5.47	3.45	0.55	3.77	0.62
7-2-4.5-5.5	14.80	5.24	3.72	0.55	3.94	0.64
8-3-15-16	15.44	6.44	3.23	0.57	4.10	0.66
9-5-20-21	16.12	6.12	3.61	0.56	4.34	0.69
10-4-20-21	16.15	5.69	5.12	0.73	4.50	0.69
13-5-7-8	16.26	7.60	7.08	0.63	4.52	1.64
14-2-5	16.86	5.50	11.89	0.58	4.82	0.74

7. Rock-Eval Pyrolysis

The hydrocarbon generative potential of source rocks is evaluated based on the quantity, thermal maturity, and type of the organic matter -- all three of which can be gauged by Rock-eval analysis (see section 4.1.5). Quantity is measured as total organic carbon content (TOC; in weight percent), thermal maturity may be reflected by Tmax values and production indices (PI), and, depending on degree of thermal maturity, organic matter type may be indicated by hydrogen and oxygen indices (HI and OI). The results of Rock-eval pyrolysis of Athens Shale samples from the Calera core are presented in (Table 9) and evaluated below.

7.1 Quantity of Organic Matter

For the eight core samples subjected to Rock-eval analysis, TOC values range from 0.83-1.12% (average = 1.02%) (Table 9).These results are consistent with the TOC values derived from the C/N analysis reported in Chapter 5 (i.e., Table 3) (average = 1.03%). While some source rocks have organic carbon values as high as 10%, the average source rock contains between 0.8 and 2% organic carbon (Barker, 1979). However, depending on organic matter type, mudrocks with TOC contents as low as 0.5% may be viable source rocks (Dow, 1977). Hence, TOC contents of the Athens Shale indicate at least moderate potential for generation of hydrocarbons.

Table 9. Results of rock-eval analysis of Calera Core samples.

Sample	TOC	S1	S2	S3	Tmax	HI	OI	PI
1-3-8	1.02	0.01	0.07	0.11	367	7	11	0.13
2-1-4	1.09	0.00	0.05	0.12	384	5	11	0.00
4-3-16	0.96	0.00	0.07	0.10	432	7	10	0.00
5-5-16	1.10	0.01	0.08	0.12	362	7	11	0.11
8-4-11	1.07	0.00	0.05	0.14	378	5	13	0.00
9-4-18	0.83	0.01	0.07	0.12	340	8	14	0.13
10-5-17	1.12	0.00	0.06	0.09	427	5	8	0.00
13-5-18	1.04	0.00	0.05	0.12	378	5	12	0.00

TOC – Total Organic Carbon, wt %

S1 - volatile hydrocarbon (HC) content, mg HC/g rock

S2 – remaining HC generative potential, mg HC/g rock

S3 – carbon dioxide content, mg CO2/g rock

HI – Hydrogen Index = S2 x 100/TOC, mg HC/g TOC

OI – Oxygen Index = S3 x 100/TOC, mg HC/g TOC

PI – Production Index = S1/(S1+S2)

7.2. Thermal Maturity

Generation of hydrocarbons depends on the thermal history of a rock during burial diagenesis. Level of thermal maturation of organic matter typically can be estimated from Tmax values derived from rock-eval pyrolysis; Tmax values increase with increased maturity (Table 10). Tmax values for Athens Shale samples range significantly from 340-432°C (average = 384°C) (Table 9). These values normally would suggest thermal immaturity (Table 10). However, when S2 values are less than 0.5 mg HC/g rock (i.e., S2 peaks are weak), as is the case with the Athens Shale samples (S2 < 0.08), Tmax values are unreliable maturity indicators (Source Rock Analyzer Guide). Indeed, given that Athens samples came from the same 140-ft core interval and likely experienced the

same thermal history, a narrower range of Tmax values would have been expected if Tmax values were valid indicators.

Production Indices (PI) for the Athens samples are also very low (0-0.13) (Table 9). Low PI could indicate low thermal immaturity. However, given the very low S1 and S2 values from which they are derived, PI likely are indicative of extreme post-mature organic matter; i.e., organic matter in the Athens Shale of the Calera core is overmature.

Table 10. Relations among Tmax values, production indices, thermal maturity, and hydrocarbon generation (modified from Hunt, 1995).

Production Index (PI)	Pyrolysis Tmax (°C)	Generalized hydrocarbon zone
<0.1	<435°C	Immature
0.1-0.2	435°- 465°C	Oil Window
0.2-0.3	465°- 480°C	Wet Gas
0.3-0.4	480°- 500°C	Methane
>0.4	>500°C	Overmature

7.3 Type of Organic Matter

The type of organic matter, or kerogen type, determines whether a source rock will be oil prone (Type I, II) or gas-prone (Type III, IV) (Table 11). Organic matter type in a source rock commonly can be determined from plots of hydrogen and oxygen indices (HI, OI) on a modified Van Krevelen diagram. Given the near lack of land plants during the Ordovician, organic matter in the Athens Shale likely would have originated as algal bodies or structureless planktonic material of marine origin and expectedly would have been oil-prone Type I kerogen. However, as shown in table 9 and figure 29, HI and OI are extremely low. This again reflects very low S1 and S2 values and supports the conclusion that the sampled intervals of Athens Shale are thermally overmature.

Table 11. Relationship among kerogen types, organic matter sources, and hydrocarbon potential.

Environment	Kerogen Type	Kerogen Form	Origin	Hydrocarbon Potential
Aquatic	Type I	Alginite	Algal bodies, phytoplankton, bacteria	Oil
Aquatic/Terrestrial	Type II	Exinite	Spores, pollen,cuticles of leaves and herbaceous plants	Oil/Some Gas
Terrestrial	Type III	Vitrinite	Fibrous and woody plant fragments	Gas/ Some Oil
	Type IV	Inertinite	Oxidized, recycled woody material	Gas

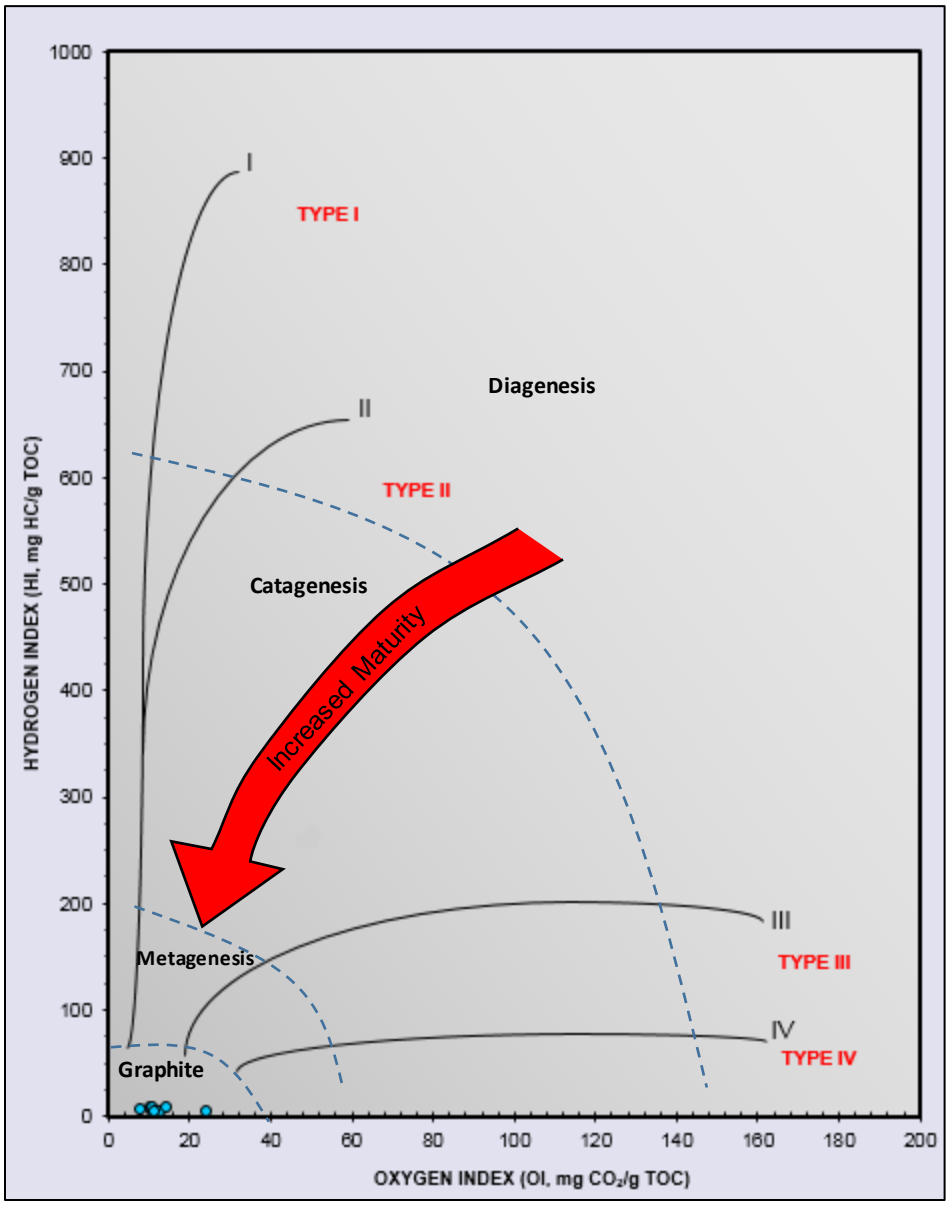

Figure 29. Athens Shale samples plotted on a modified Van Krevelen diagram.

7.4. Hydrocarbon-Source Potential

Results indicate that the Athens Shale may have contained adequate amounts of potentially oil-prone organic matter to serve as a hydrocarbon source rock. However, rock-eval pyrolysis indicates that the Athens Shale in the Calera core section is thermally overmature. Hence, the Athens Shale at this locality may be regarded as a spent source rock; i.e., a source bed that has completed the process of oil or gas generation and expulsion (Barker, 1979). If hydrocarbons were generated during burial, they may have migrated out of the shale earlier in its diagenetic history.

7.5 Comparison with Athens Shale Equivalents

Other Ordovician black shales deposited in Taconic basins in eastern North America have been recognized as potential source rocks. Wallace and Roen (1989) and Ryder et al. (1998) performed rock-eval pyrolysis on the Middle to Upper Ordovician Utica sequence in Ohio and adjacent states. They report TOC contents comparable to that of the Athens Shale, the dominance of type II kerogen, and varying levels of thermal maturity. Tmax values, production indices, and genetic potential (S1 + S2) indicate a transition from the hydrocarbon-generating catagenetic stage to the metagenetic stage eastward toward the Alleghenian tectonic front. Shales are thermally mature (in the oil or gas windows) in eastern and central Ohio. However, further east, shales experienced deeper burial and more intense deformation and, like the Athens Shale in the Calera section, they are thermally over mature.

8. Summary and Conclusions

The Ordovician Athens Shale found in the Alabama fold and thrust belt previously received limited attention compared to other black shales in the region. The current study focused on analyses of a 140-ft-thick core section of the Athens Shale near Calera, Alabama, but also included observations of limited outcrop exposures of this unit. Lithologic, petrologic, and geochemical studies were designed to (1) characterize the mudrock lithofacies of the Athens Shale; (2) interpret the environmental conditions and processes that influenced Athens Shale deposition; and (3) assess the potential of the Athens Shale as a hydrocarbon-source rock. Principal findings of this study are summarized below.

(1) Four broad lithofacies are recognized in the Calera core interval of the Athens Shale: Lithofacies A- nodular limestone in calcareous mudstone; Lithofacies B- carbonaceous shale with thin- to medium-bedded limestone; Lithofacies C- carbonaceous shale with thin, fine-grained carbonate beds and laminae; and Lithofacies D- carbonaceous shale.

(2) A variety of depositional processes were responsible for Athens Shale deposition. Lithofacies A reflects deposition primarily by debris flows. Limestone beds and laminae in Lithofacies B and C are attributed, respectively, to proximal and distal turbidity current deposition. Carbonaceous shales in Lithofacies B, C, and D were likely deposited by pelagic and hemipelagic processes. The vertical

succession from lithofacies A, through lithofacies B and C, to lithofacies D reflects increasing slope stability and/or basin deepening through time. Evidence for sparse bioturbation become more prevalent upward through the section, suggesting at least periodic improvement of basin oxygenation.

(4) Outcrop exposures of the Athens Shale at Pratts Ferry and Vincent, Alabama, include limestones with graded bedding and soft-sediment deformation features. These beds, like those in lithofacies A and B in the Calera core, reflect basin-margin slope instability.

(5) Geochemistry of mudrocks indicate that, unlike other black shales, the Athens Shale is not metalliferous.

(6) Applications of geochemical proxies for basin paleo-redox conditions yielded mixed results. However, some elemental ratios (i.e., V/Cr and U/Th) suggest a general trend towards improved oxygenation over time, consistent with evidence provided by poorly developed bioturbation in the upper parts of the section.

(7) Applications of geochemical approaches to evaluate the provenance of Athens Shale muds indicate a passive-margin source and quartzose sedimentary provenance. This differs from what would be expected in a basin formed in response to arc-related Taconic orogenesis.

(8) Organic carbon (TOC) contents of the Athens Shale are sufficient for this unit to serve as a hydrocarbon-source rock. However, Rock-eval pyrolysis indicates that the Athens Shale in the Alabama fold and thrust belt is now thermally overmature and potentially can be considered a spent source rock.

REFERENCES

Barker, C., 1979, Organic geochemistry in petroleum exploration: American Association of Petroleum Geologists Education course note series no. 10, 159 p.

Benson, D.J., 1986, Depositional setting and history of the Middle Ordovician of the Alabama Appalachians: *in* Benson, D.J., and Stock, C.W., (eds.), Depositional history of the Middle Ordovician of the Alabama Appalachians, Alabama Geological Society, 23rd Annual Fieldtrip guidebook, p.15-31.

Benson, D.J., and Mink, R.M., 1983, Depositional history and petroleum potential of the Middle to Upper Ordovician of the Alabama Appalachians: Gulf Coast Association of Geological Societies, Transactions, v. 33, p. 13-21.

Berner, R.A., 1982, Burial of organic carbon and pyrite sulfur in the modern ocean: its geochemical and environmental significances: American Journal of Science, v. 282, p. 451-473.

Berner, R.A., and Raiswell, R., 1983, Burial of organic carbon and pyrite sulphur in sediments over Phanerozoic time: a new theory: Geochimica Cosmochimica Acta, v. 47, p. 855-862.

Boggs, S., 2006, Principles of sedimentary and stratigraphy: Pearson Prentice Hall, 662 p.

Berry, B.N., and Wilde, P., 1978, Progressive ventilation of the oceans-an explanation for the distribution of the Lower Paleozoic black shales: American Journal of Science, v. 278, p. 257-275.

Bohacs, K.M., Grabowski, G.J., Carroll, A.R., Mankiewicz, P.J., Miskell-Gerhardt, K.J., Schwalbach, J.R., Wegner, M.B., Simo, J.A., 2005, Production, destruction, and dilution-the many paths to source-rock development, *in*: Harris, N.B. (eds.), The deposition of organic-carbon-rich sediments: models, mechanisms, and consequences: Society for Sedimentary Geology, Special Publication, p. 61-101.

Bohacs, K.M., Lazar, O.R., and Demko, T.M., 2014, Parasequence types in shelfal mudstone strata—Quantitative observations of lithofacies and stacking patterns, and conceptual link to modern depositional regimes: Geology, v. 42, p. 131-134.

Carroll, R.E., Pasin, J.C., and Kugler, R.L., 1995, Burial history and source-rock characteristics of Upper Devonian through Pennsylvanian strata, Black Warrior basin, Alabama: Alabama Geological Survey Circular 187, 29 p.

Carter, B.D., and Chowns, T.M., 1986, Stratigraphic and environmental relationships of Middle and Upper Ordovician rocks in northwestern Georgia and northeastern Alabama: *in* Benson, D.J., and Stock, C.W., (eds.), Depositional history of the Middle Ordovician of the Alabama Appalachians: Alabama Geological Society, 23rd Annual Field Trip Guidebook, p. 33-50.

Conant, L.C., and Swanson, V.E., 1961, Chattanooga shale and related rocks of central Tenessee and nearby areas: Geological Survey Professional Paper 357, 91 p.

Crevello, P.D., and Schlager, W., 1980, Carbonate debris sheets and turbidites, Exuma Sound, Bahamas: Journal of Sedimentary Petrology, v. 50, p. 1121-1148.

Dow, W.G., 1977, Kerogen studies and geological interpretations: Journal of Geochemical Exploration, v. 7, p.79-99.

Engelder, T., Lash, G. G., and Uzcategui, R. S., 2009, Joint sets that enhanced production from Middle and Upper Devonian gas shales of the Appalachian basin: American Association of Petroleum Geologists Bulletin, v. 95, p. 857-889.

Frost, J.K., Zierath, D.L., and Shimp, N.F., 1985, Chemical composition and geochemistry of the New Albany Shale Group (Devonian-Mississippian) in Illinois: Illinois State Geological Survey, 134 p.

Gale, J.F.W., Reed, R.M., and Holder, J., 2007, Natural fractures in the barnett shale and their importance for hydraulic fracture treatments: American Association of Petroleum Geologists Bulletin, v. 91, p. 603-622.

Gleason J.D., Finney, S.C., and Gehrels, G.E., 2002, Paleotectonic implications of a mid-to late-Ordovician provenance shift, as recorded in sedimentary strata of the Ouachita and southern Appalachian mountains: Journal of Geology, v.110, p. 291-304.

Hammes, U., and Frébourg, G., 2012, Haynesville and bossier mudrocks: A facies and sequence stratigraphic investigation, East Texas and Louisiana, USA: Marine and Petroleum Geology, v. 31, p. 8-26.

Hampton, M.A., 1972, The role of subaqueous debris flow in generating turbidity currents: Journal of Sedimentary Petrology, v. 42, p. 775-793.

Hampton, M.A., 1975, Competence of fine-grained debris flows: Journal of Sedimentary Petrology, v. 45, p. 834-844.

Hatcher, R.D., 2010, The Appalachian orogeny: A brief summary: Geological Society of America Memoirs no. 206, p. 1-19.

Haynes, C.D., Malone, P.G., and Camp, B.S., 2010, Exploration of the shallow Chattanooga Shale in north central Alabama: Tuscaloosa, Alabama, University of Alabama, College of Continuing Studies, 2010 International Coalbed & Shale Gas Symposium Proceedings, paper 1015, 16 p.

Hunt, J.M., 1995, Petroleum Geochemistry and Geology: W.H. Freeman and Company, New York, 389 p.

Johnson, A.M., 1970, Physical Processes in Geology: Freeman, Cooper and Co., San Francisco, 577 p.

Jones, B., and Manning, D.A., 1994, Comparison of geochemical indices used for the interpretation of palaeoredox conditions in ancient mudstones: Chemical Geology, v. 111, p. 111-129.

Klemme, H.D., and Ulmishek, G, F., 1991, Effective petroleum source rocks of the world: stratigraphic distribution and controlling depositional factors: American Association of Petroleum Geologists Bulletin, v. 91, p. 1809-1851.

Kuscu, M., Ozsoy, R., Ozcelik, O., and Altunsoy, M., 2016, Trace and rare earth element geochemistry of black shales in Triassic kasmlar formation, anamas-akseki platform, western Taurid, Turkey. IOP Conference Series: Earth and Environmental Science, v. 44, no. 4, p. 042012.

Lazar, R.O., Bohacs, K.M., MacQuaker, H.S., Schieber, J., and Demko, T.M., 2015, Capturing key attributes of fine-grained sedimentary rocks in outcrops, cores, and thin section: Nomenclature and descriptive guidelines: Journal of Sedimentary Research, v. 85, p. 230–246.

Leventhal, J.S., and Hosterman, J.W., 1982, Chemical and mineralogical analyses of Devonian black shales from Martin County, Kentucky; Carroll and Washington Counties, Ohio; Wise County, Virginia; and Overton County, Tennessee, USA: Chemical Geology, v. 37, p. 239-264.

Leventhal, J.S., and Kepferle, R.C., 1982, Geochemistry and geology of strategic metals and uranium in Devonian shales of the eastern interior United States. Synthetic Fuels of Oil Shales II Proceedings: Institute of Gas Technology, p. 73-97.

Leventhal, J.S., 1987, Carbon and sulfur relationships in Devonian shales from the Appalachian basin as indicators of environments and deposition: American Journal of Science, v. 287, p. 33-49.

MaQuacker, H.S., Keller, M.A., and Davies, S.J., 2010a, Algal blooms and “marine snow”: Mechanisms that enhance preservation of organic carbon in ancient fine-grained sediments: Journal of Sedimentary Research, v. 80, p. 934-942.

Macquaker, J.H.S., Bentley, S.J., and Bohacs, K.M., 2010b, Wave-enhanced sediment-gravity flows and mud dispersal across continental shelves: Reappraising sediment transport processes operating in ancient mudstone successions:Geology, v. 38, p. 947-950.

McCarthy, K., Rojas, K., Palmowski, D., Peters, K. and Stankiewicz, A., 2011, Basic Petroleum geochemistry for source rock evaluation: Oilfield Review, v. 23, p. 32-43.

McIlreath, I.A., and James, N.P., 1984, Carbonate slopes: *in* Walker, R.G., (eds.), Facies Models, 2nd ed., Geoscience Canada Reprint Series 1, p. 245-257.

Niocaill, C.M., Van der Pluijm, B.A., and Van der Voo, R., 1997, Ordovician paleogeography and the evolution of the Iapetus ocean: Geology, v. 25, p. 159-162.

O'Brien, N.R., 1996, Shale lamination and sedimentary processes: Journal of Geological Society of London Special Publication 116, p. 23-36.

Pashin, J.C., 2008, Gas shale potential of Alabama: Tuscaloosa, Alabama, University of Alabama, College of continuing Studies, 2008 International Coalbed & Shale Gas Symposium Proceedings, paper 0808, 13 p.

Pashin, J.C., 2009, Shale gas plays of the southern Appalachian thrust belt: Tuscaloosa, Alabama, University of Alabama, College of continuing Studies, 2009 International Coalbed & Shale Gas Symposium Proceedings, paper 0907, 14 p.

Passey, Q.R., Bohacs, K.M., Esch, W.L., Klimentidis, R., and Sinha, S., 2010, From oil-prone source rocks to gas- producing shale reservoir- geologic and petrophysical characteristics of unconventional shale-gas reservoirs: International Oil and Gas Conference and Exhibition, Beijing China, June 8-19, 2010, Society of Petroleum Engineers Paper 131350, 29 p.

Raiswell, R., and Canfield, D.E., 2012, The iron biogeochemical cycle past and present: Geochemical Perspectives, no.1, p. 1-2.

Raymond, D.E., Osborne, W.E., Copeland, C.W., and Neathery, T.L., 1988, Alabama Stratigraphy: Geological Survey of Alabama, Circular 140, 97 p.

Rimmer, S.M., 2004. Geochemical paleoredox indicators in Devonian-Mississippian black shales, central Appalachian basin (USA): Chemical Geology, v. 206, no. 3, p. 373-391.

Read, J.F., 1980, Carbonate ramp-to-basin transition and foreland basin evolution, Middle Ordovician, Virginia Appalachians: American Association of Petroleum Geologists Bulletin, v. 64, p. 1575-1612.

Rodgers, J., 1970, The tectonics of the Appalachians: New York, John-Wiley and Sons, 271 p.

Roser, B,P., and Korsch, R.J., 1986, Determination of tectonic setting of sandstone-mudstone suites using SiO2 content and K2O/Na2O ratio: The Journal of Geology, v. 94, p. 635-650.

Roser, B.P., and Korsch, R.J., 1988, Provenance signatures of sandstone-mudstone suites determined using discriminant function analysis of major-element data: Chemical Geology, v. 67, p. 119-139.

Ruppel, S.C., and Walker, K.R., 1984, Petrology and depositional history of a Middle Ordovician carbonate platform: Chickamauga Group, northeastern Tennessee: Geological Society of America Bulletin, v. 95, p. 568-583.

Ryder, R.T., Burruss, R.C., and Hatch, J.R., 1998, Black shale source rocks in the Cambrian and Ordovician of the central Appalachian basin, USA: American Association of Petroleum Geologists Bulletin, v. 82, p. 412-441.

Saunders, J.A., and Savrda, C.E., 1993, Geochemistry of the Athens Shale: Implications for the genesis of Mississippi valley-type deposits of the southernmost Appalachians: Southeastern Geology, v. 33, p. 161-170.

Schieber, J., 1994a, Evidence for episode high energy events and shallow water deposition in the Chattanooga Shale, Devonian, central Tennessee, U.S.A.: Sedimentary Geology, v. 93, p. 193-208.

Schieber, J., 1994b, Reflection of deep vs. shallow water deposition by small scale sedimentary features and microfabrics of the Chattanooga Shale in Tennessee: Canadian Society of Petroleum Geologists, Memoir 17, p. 773-784.

Schieber, J., 1998, Sedimentary features indicating erosion, condensation, and hiatuses in the Chattanooga Shale of central Tennessee: Relevance for sedimentary and stratigraphic evolution. *In*: Schieber, J., Zimmerle, W., and Sethier, P., (eds.), Shales and Mudstones (vol. 1): Basin Studies, Sedimentology and Paleontology, Schweizerbart'sche Verlagsbuchhandlung, Stuttgart, p. 187-215.

Schieber, J., Southard, J.B., and Thaisen, K., 2007, Accretion of mudstone beds from migrating floccule ripples: Science, v. 318, p. 1760-1763.

Schieber, J., and Southard, J.B., 2009, Bedload transport of mud by floccule ripples— Direct observation of ripple migration processes and their implications: Geology, v. 37, p. 483-486.

Schieber, J., 2011, Marcasite in black shales- a mineral proxy for oxygenated bottom waters and intermittent oxidation of carbonaceous muds: Journal of Sedimentary Research, v. 81, p. 447-458.

Scholle, P.A., and Ulmer-Scholle, D.S., 2003, A color guide to the petrography of carbonate rocks: grains, textures, porosity, diagenesis: The American Association of Petroleum Geologists Memoir 77, p. 60-62.

Servais, T., Munnecke, A., and Versteegh, G.J.M., 2009, Silurian calcispheres (calchitarcha) of Gotland (Sweden): comparisons with calcareous dinoflagellates: Comptes Rendus Palevol 8, p. 527-534.

Shanmugan, G. and Benedict, G.L., 1978, Fine-grained debris flows, Ordovician basin margin, southern Appalachians: Journal of Sedimentary Petrology, v. 48, no. 4, p. 1233-1240.

Shanmugan, G., 1980, Rhythms in deep sea, fine-grained turbidite and debris-flow sequences, Middle Ordovician, eastern Tennessee: Sedimentology, v. 27, p. 419-432.

Shanmugam, G., and Walker, K.R., 1980, Sedimentation, subsidence, and evolution of a foredeep basin in the Middle Ordovician, southern Appalachians: American Journal of Science, v. 280, p. 479-496.

Shanmugan, G., and Lash, G.G., 1980, Analogous tectonic evolution of the Ordovician foredeeps, southern and central Appalachians: American Journal of Science, v. 10, p. 562-566.

Shanmugan, G. and Walker, K.R., 1983, Anatomy of the Middle Ordovician Sevier Shale basin, eastern Tennessee: Sedimentary Geology, v. 34, p. 315-337.

Soeder, D.J., 1988, Porosity and permeability of eastern Devonian gas shales: Society of Petroleum Engineers Formation Evaluation, March 1988, p. 116-124.

Stow, D.A.V., Huc, A.Y., and Bertrand, P., 2001, Depositional processes of black shales in deep water: Marine and Petroleum Geology, v. 18, p. 491-498.

Telle, W.R., Thompson, D.A., Lottman, L.K., and Malone, P.G., 1987, Preliminary burial-thermal history investigation of the black warrior basin: Implications for coalbed methane and conventional hydrocarbon development: Tuscaloosa, Alabama, University of Alabama, 1987 Coalbed Methane Symposium Proceedings, p. 37-50.

Tissot, B.P., and Welte, D.H., 1984, Petroleum formation and occurrence, 2 ed.: New York, Springer Verlag, 699 p.

Tucker, M.E., and Wright, P.V., 2009, Carbonate Sedimentology. John Wiley and Sons, p. 48-51.

Turekian, K.K., and Wedepohl, K.H., 1961, Distribution of the elements in some major units of the Earth's crust: Geological Society of America Bulletin, v. 72, p. 175-191.

Tyson, R.V., and Pearson, T.H., 1991, Modern and ancient continental shelf anoxia: an overview: in Geological Society of London Special Publication, v. 58, no. 1, p. 1-24.

Versteegh, G.J.M., Servais, T., Munnecke, A., Streng, M., and Vachard, D., 2009, A discussion and proposal concerning the use of the term calcispheres: Paleontology, v. 52, no. 2, p. 343-348.

Vine, J.D., and Tourtelot, E.B., 1970, Geochemistry of black shale deposits – A summary report: Economic Geology, v. 65, p. 253-272.

Walker, K.R., and Benedict, G.L., III, 1980, Slope facies of the Whitesburg Formation and overlying basinal pelagic shales of the Blockhouse Formation near Silver City, Tennessee, in Walker, K.R., Broadhead, T.W., and Keller, F.B., (eds.), Middle Ordovician carbonate shelf to deep-water basin deposition in the Southern Appalachians, University of Tennessee: Studies in Geology no. 4, p. 81-85.

Walker, K.R., and Ruppel, S.C., 1984, Petrology and depositional history of a Middle Ordovician carbonate platform: Chickamauga Group, northeastern Tennessee. Geological Society of America Bulletin, v. 95, p. 568-583.

Wallace, L.G., and Roen, J.B., 1989, Petroleum source rock potential of the Upper Ordovician black shale sequence, northern Appalachian basin: USGS open file report 89-488, 46 p.

Appendix A

Photographs of Calera Core boxes showing positions of close-up photographs, thin-section samples, and samples for carbonate, organic carbon, geochemical, and rock-eval analyses.

Legend

Rock-eval pyrolysis

Geochemical Analysis

Carbonate/organic carbon analysis

Thin-section samples

Close-up photographs

Box 14 169-179

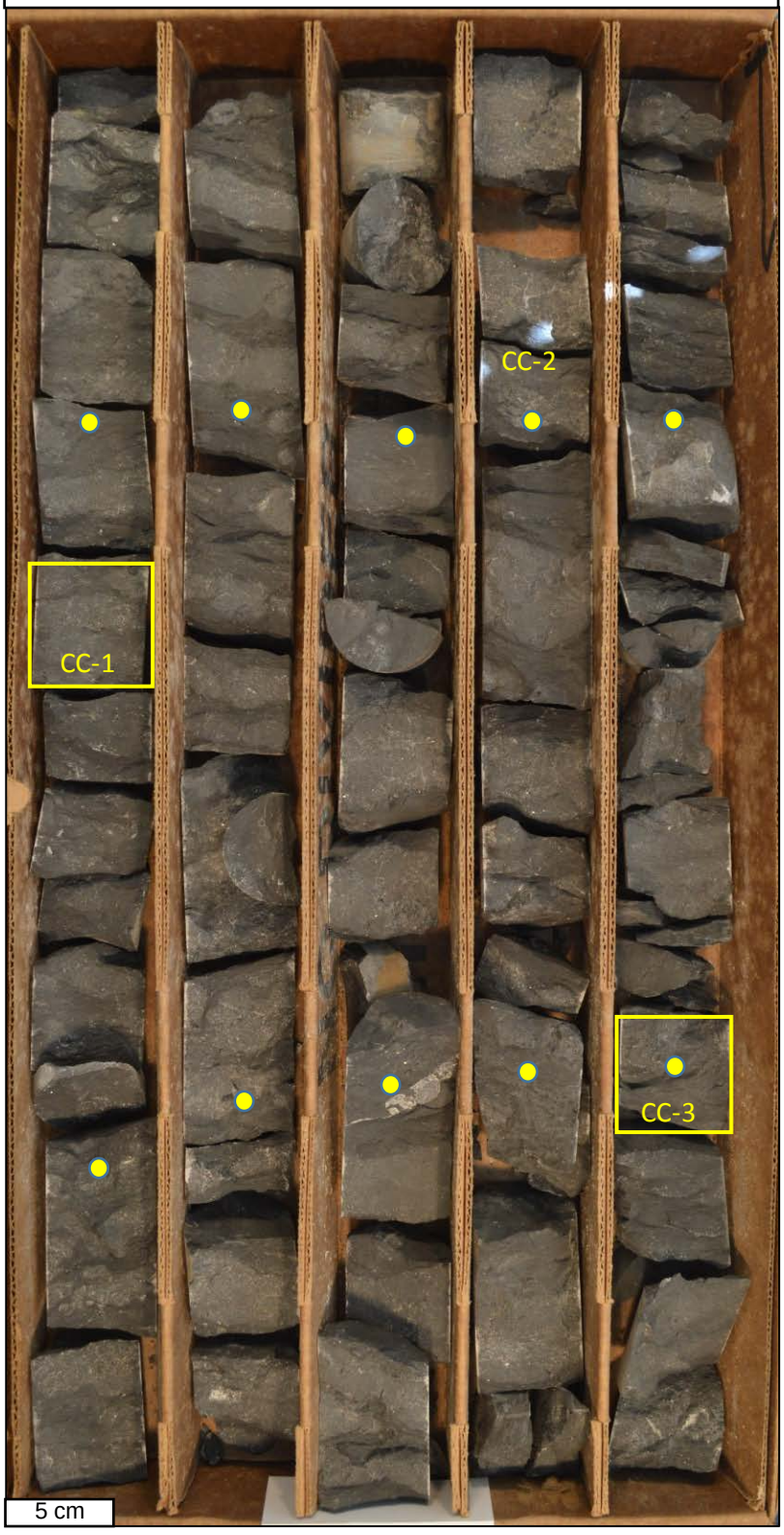

Box 13 169-179’

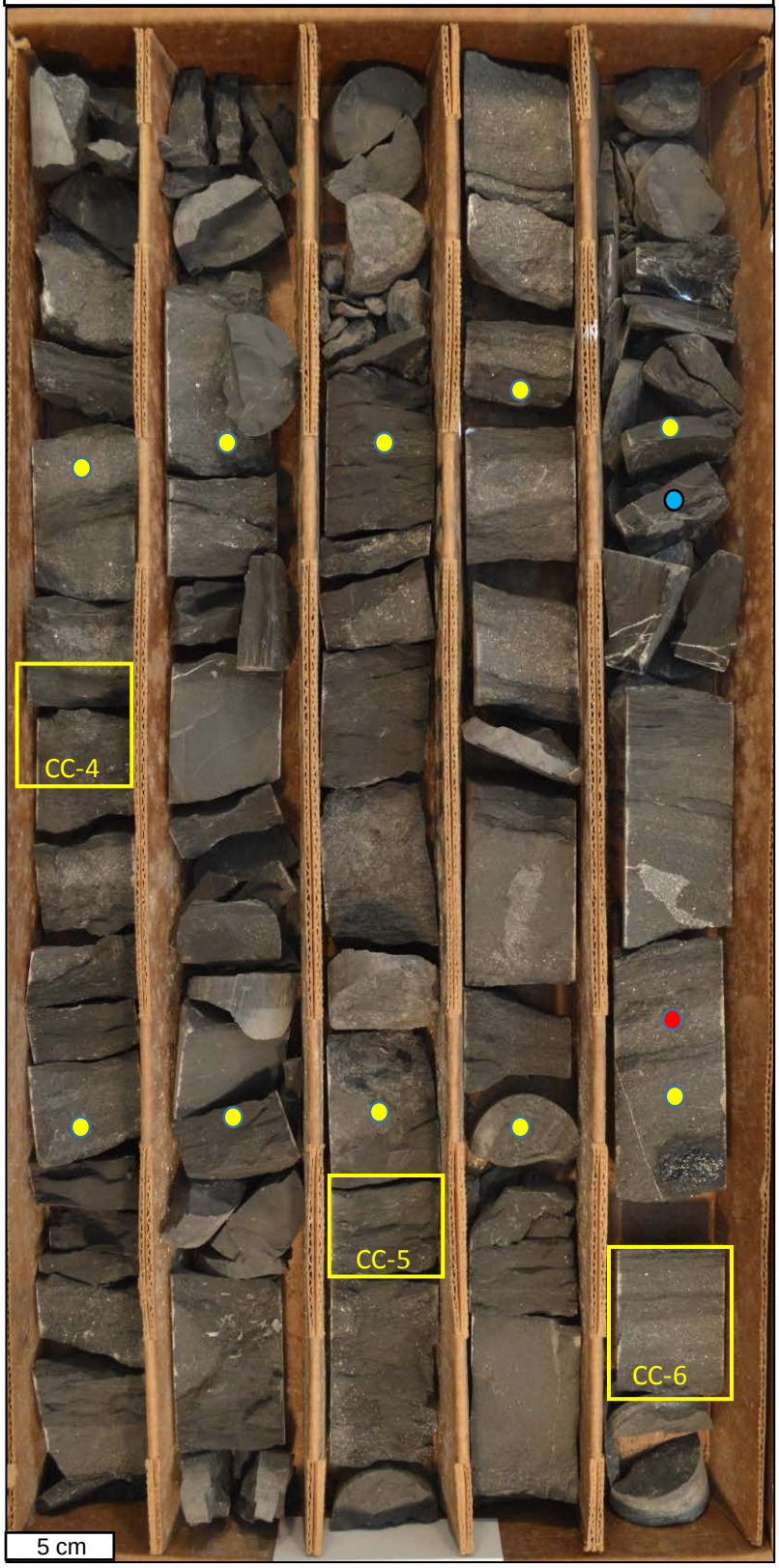

Box 12 149-159’

Box 11 139-149’

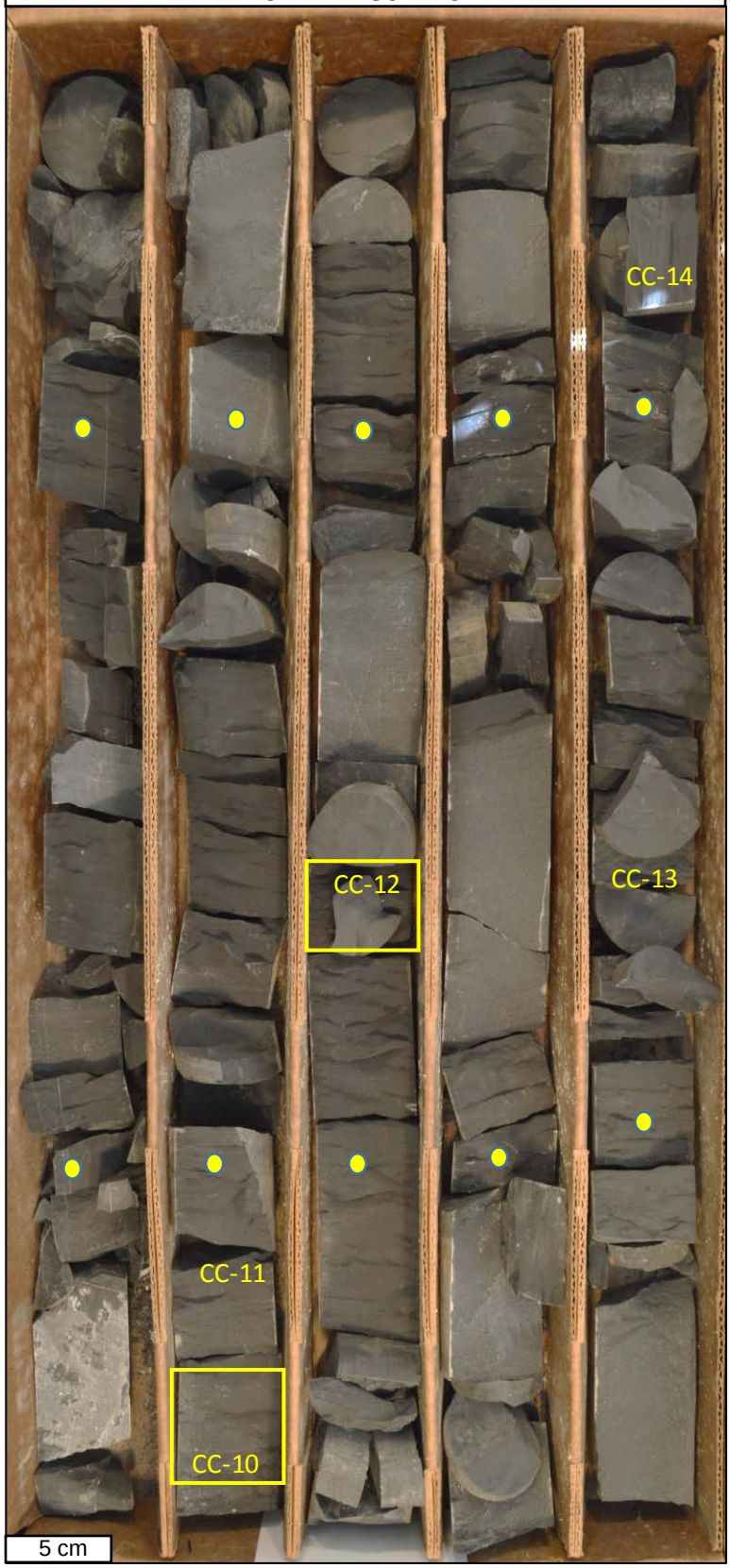

Box 10 129-139’

Box 9 119-129’

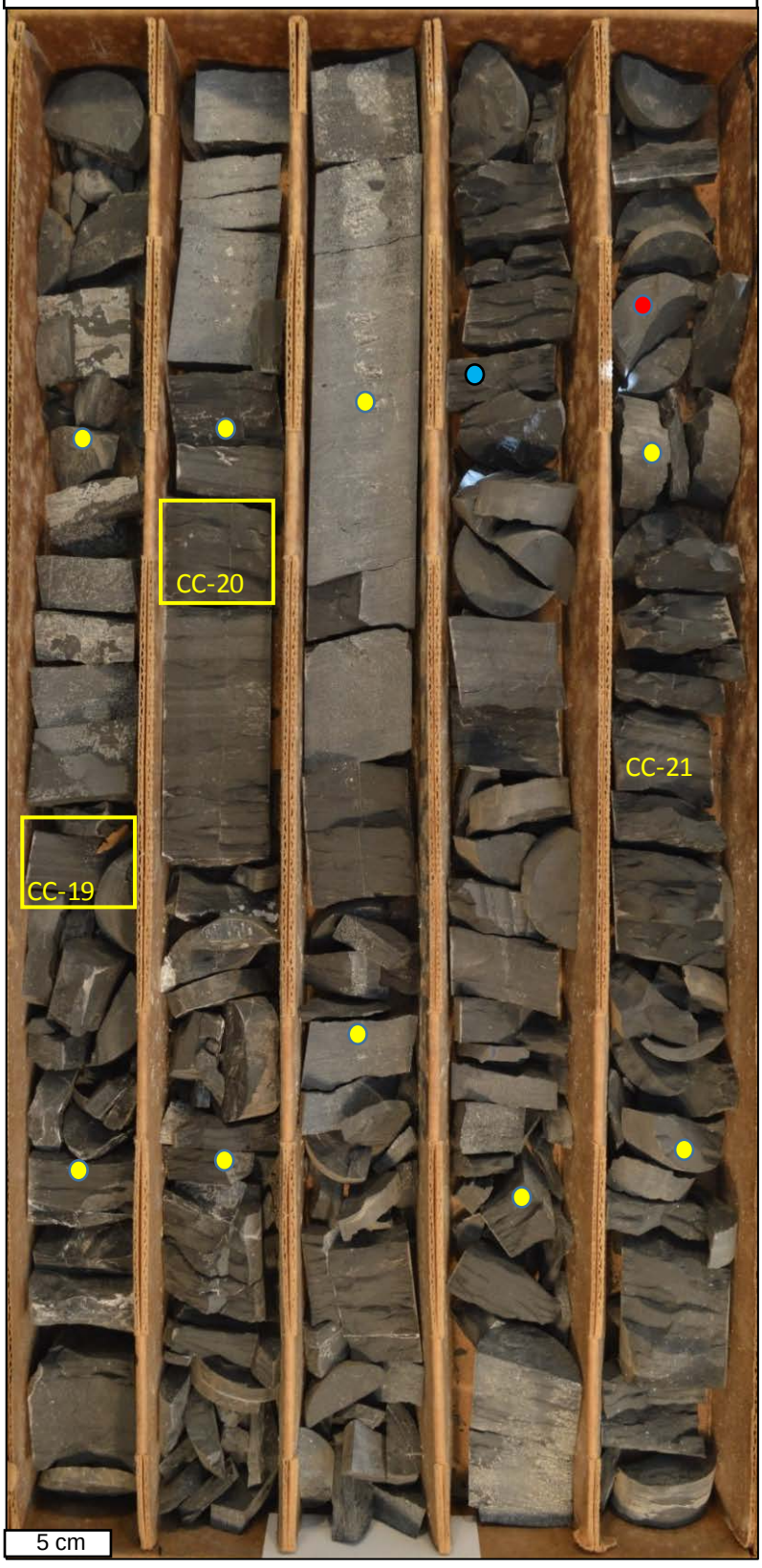

Box 8 109-119’

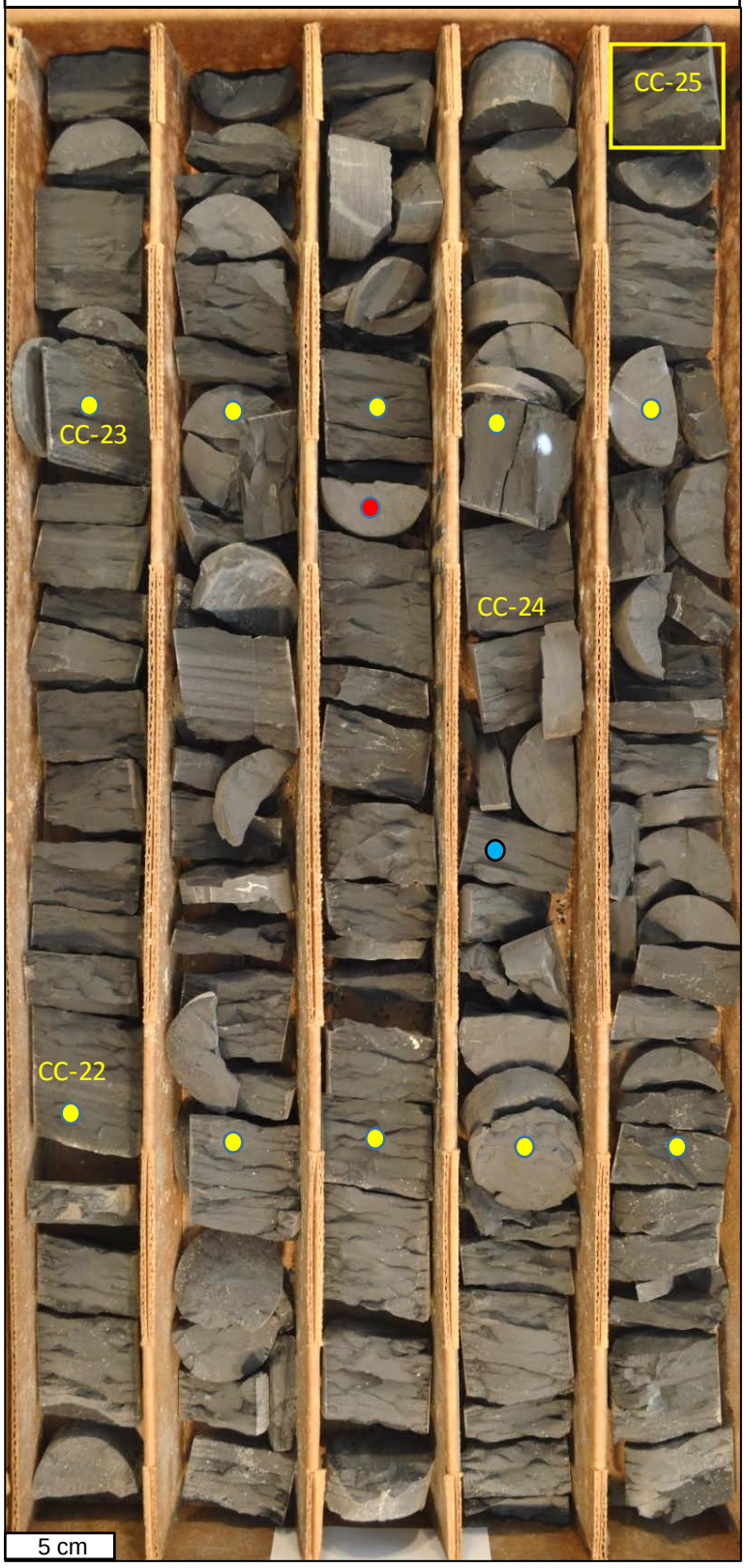

Box 7 99-109’

Box 6 89-99’

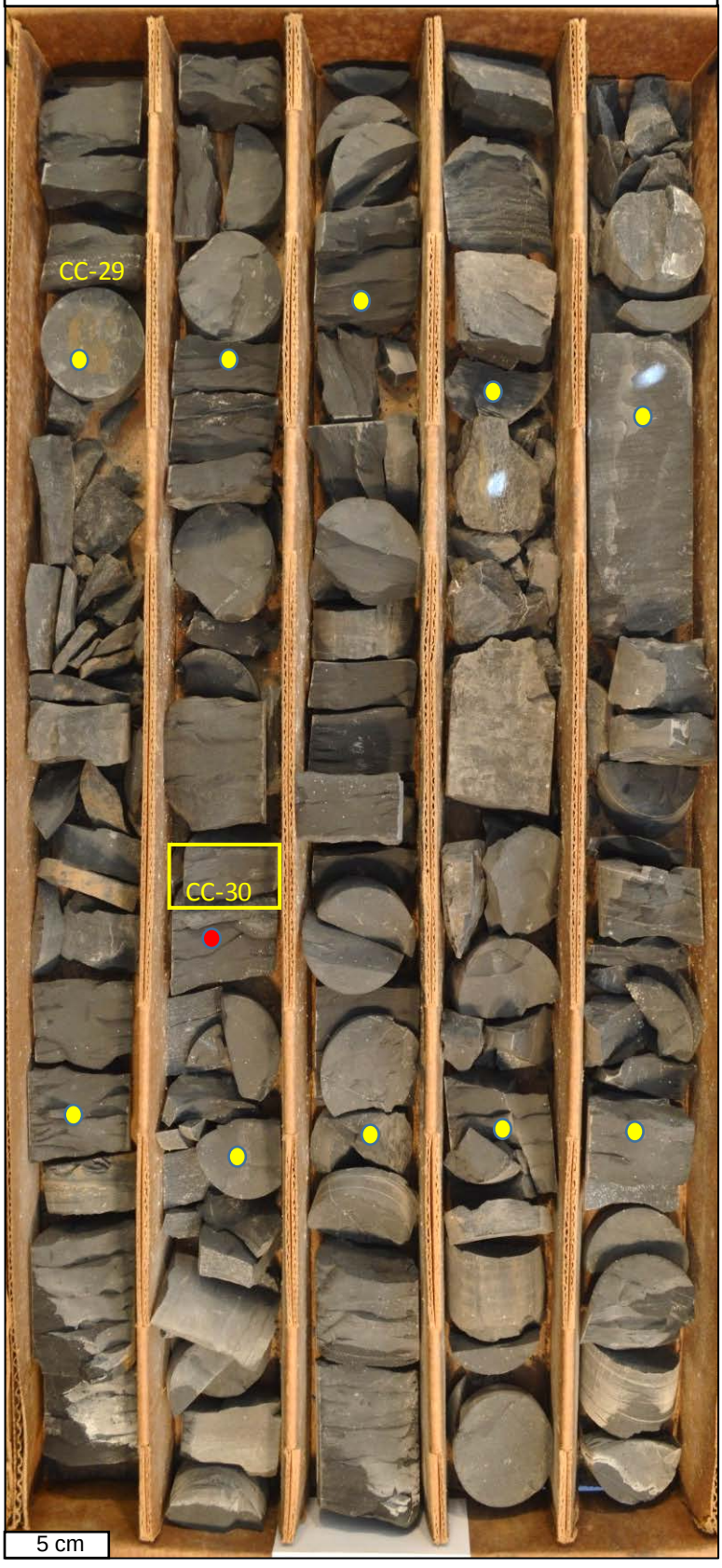

Box 5 79-89’

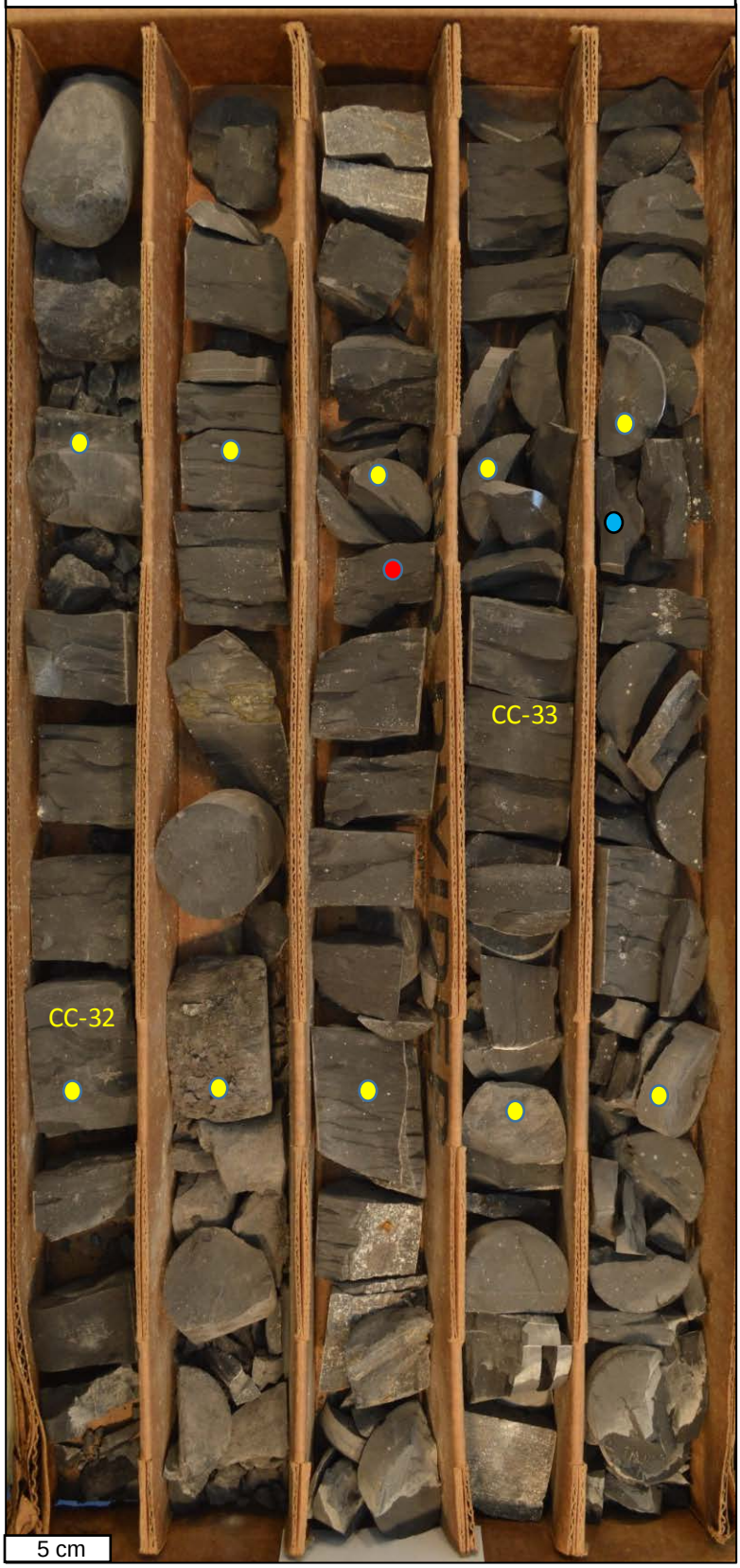

Box 4 69-79’

Box 3 59-69’

Box 2 49-59’

Box 1 39-49’